



Title	DEFECTS IN GALLIUM ARSENIDE SINGLE CRYSTALS GROWN BY GRADIENT FREEZE METHOD
Author(s)	Fujii, Katsushi
Citation	大阪大学, 1994, 博士論文
Version Type	VoR
URL	<a href="https://doi.org/10.11501/3075267">https://doi.org/10.11501/3075267</a>
rights	
Note	

*The University of Osaka Institutional Knowledge Archive : OUKA*

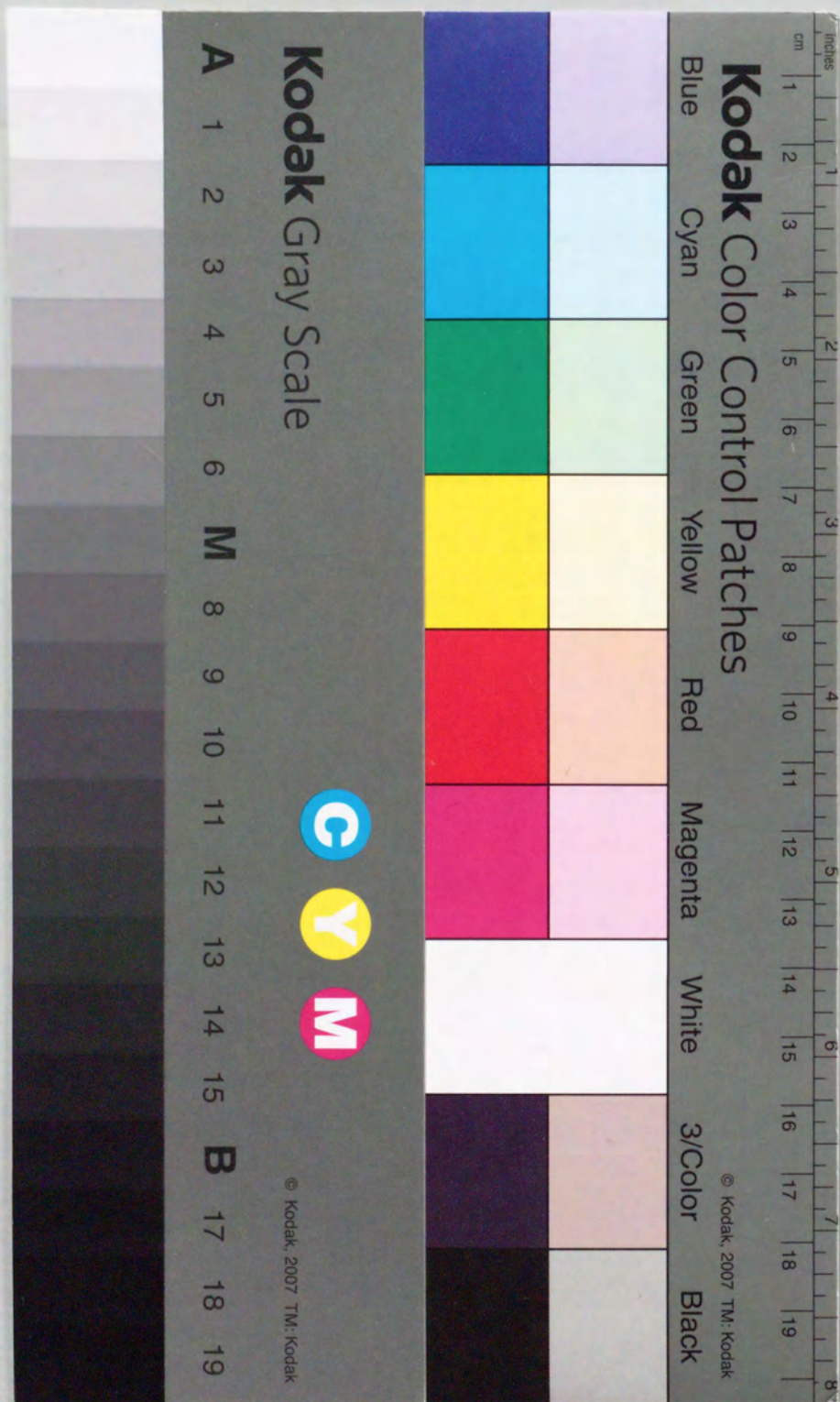
<https://ir.library.osaka-u.ac.jp/>

The University of Osaka



DEFECTS IN GALLIUM ARSENIDE  
SINGLE CRYSTALS GROWN BY  
GRADIENT FREEZE METHOD

Katsushi FUJII





①

**DEFECTS IN GALLIUM ARSENIDE SINGLE  
CRYSTALS GROWN BY GRADIENT FREEZE METHOD**

Katsushi FUJII

Opto-electronics Laboratory, Tsukuba Plant  
Mitsubishi Kasei Corporation

(November, 1993)



## SYNOPSIS

Semi-conducting bulk gallium arsenide single crystals grown by boat growth method are commonly used as substrate for light emitting diodes and also laser diodes. In this thesis, the present author has chosen some problems on the lattice defects which have been commonly found in gallium arsenide single crystals grown by the gradient freeze method, a kind of boat growth method.

Defect distribution and the shape of the solid-liquid interface were investigated by chemical etching. The nature of each defect was identified by transmission electron microscopy. There is a close relation among the distribution of defects, the shape of solid-liquid interface and the nature of defects. A numerical simulation of the initial stress caused by solidification-induced volume expansion and the stress started at the interface was carried out. The obtained defect distribution corresponds well with that of observed defects.

Gallium arsenide crystals grown by the gradient freeze method are usually contaminated with silicon and oxygen, from the reaction between gallium and quartz boat. This is explained by a thermodynamic analysis of the gallium - arsenic - silicon - oxygen system. The effect of reduced oxygen concentration on the electrical properties of the crystals is also discussed.

Beside above problems, (1) the effect of arsenic vapor pressure on the spatial distribution of silicon, (2) the effect of silicon doping on the lattice parameter, and (3) the nature of silicon related defects are also discussed in the following chapters.



# DEFECTS IN GALLIUM ARSENIDE SINGLE CRYSTALS GROWN BY GRADIENT FREEZE METHOD

## <CONTENTS>

1. INTRODUCTION .....	1
1-1. GENERAL INTRODUCTION .....	1
1-2. BULK CRYSTAL GROWTH OF GALLIUM ARSENIDE .....	2
1-2-1. Boat Growth Method and Liquid Encapsulated Czochralski Method .....	2
1-2-2. The Boat Growth Method .....	4
1-2-3. Impurities in the crystal .....	12
1-2-4. Structural Defect .....	14
2. CRYSTAL EVALUATION .....	18
2-1. INTRODUCTION .....	18
2-2. CRYSTAL GROWTH .....	18
2-3. IMPURITY ANALYSIS .....	19
2-3-1. Impurities in Semiconductors .....	19
2-3-2. Flameless Atomic Absorption Spectrometry .....	19
2-3-2. Secondary Ion Mass Spectroscopy .....	21
2-3-3. Charged Particle Activation .....	23
2-4. STRUCTURAL ANALYSIS .....	24
2-4-1. Structural Defects of Semiconductors .....	24
2-4-2. Chemical Etching .....	24
2-4-3. Lattice Parameter Measurement .....	27
2-4-4. X-ray Topography .....	31
2-5. ELECTRICAL AND OPTICAL ANALYSIS .....	35
2-5-1. Electrical and Optical Properties in Semiconductors .....	35
2-5-2. Resistivity, Carrier Concentration, and Hall Mobility .....	35
2-5-3. Deep Level Transient Spectroscopy .....	38
2-5-4. Photoluminescence .....	42
3. SOLID-LIQUID INTERFACE SHAPE AND CHARACTERISTIC STRUCTURAL DEFECTS .....	46
3-1. INTRODUCTION .....	46
3-2. EXPERIMENTS .....	46
3-3. EXPERIMENTAL RESULTS .....	48
3-4. DISCUSSIONS .....	55
3-5. CONCLUSION .....	55
4. THE ROLE OF DIFFUSION BARRIER TEMPERATURE IN CRYSTAL GROWTH .....	59
4-1. INTRODUCTION .....	59
4-2. EXPERIMENTS .....	60
4-2-1. Crystal Growth .....	60
4-3. RESULTS .....	62
4-3-1. Crystallographic Properties .....	62
4-3-2. Impurity Analysis .....	62
4-3-3. Electronic Properties .....	64
4-4. DISCUSSION .....	64
4-4-1. Reaction Between GaAs Melt and Quartz Boat .....	64
4-4-1-a. Review of Previous Studies .....	64
4-4-1-b. Oxygen Contamination .....	71
4-4-1-c. Si Concentration .....	72
4-4-2. Effect of Oxygen in GaAs Crystals .....	75
4-4-2-a. Electronic Properties .....	75
4-4-2-b. Deep Level .....	78
4-4-2-c. Concentrations of Impurities Along Dislocation Lines .....	80
4-4-2-d. Chemical Forms of Oxygen in GaAs Crystals .....	80



4-5. CONCLUSION.....	82
5. THE EFFECT OF ARSENIC VAPOR PRESSURE ON THE SPATIAL DISTRIBUTION OF SILICON .....	84
5-1. INTRODUCTION .....	84
5-2. EXPERIMENTS .....	84
5-3. RESULTS AND DISCUSSION .....	85
5-4. CONCLUSION.....	91
6. EFFECT OF SILICON DOPING ON LATTICE PARAMETER AND THE NATURE OF SILICON RELATED DEFECTS .....	96
6-1. INTRODUCTION .....	96
6-2. EXPERIMENTS .....	96
6-3. RESULTS .....	97
6-3-1. Lattice Parameter .....	97
6-3-2. Electrical Properties .....	100
6-3-4. Dependence of Melt Composition on Lattice Parameter .....	110
6-4. DISCUSSION .....	113
6-5. CONCLUSION.....	116
7. DEFECT REACTIONS BY HEAT TREATMENT OF HEAVILY SILICON DOPED GALLIUM ARSENIDE .....	118
7-1. INTRODUCTION .....	118
7-2. EXPERIMENTS .....	118
7-3. RESULTS .....	119
7-3-1. Distribution of Si-Related Segregation.....	119
7-3-2. Lattice Parameter, Carrier Concentration and Mobility in Si-Related Segregation Region .....	127
7-4. DISCUSSION .....	133
7-5. CONCLUSION.....	140
8. CONCLUSION AND SUMMARY .....	144
ACKNOWLEDGMENTS .....	146
REFERENCES .....	147

## **1. INTRODUCTION**

### **1-1. GENERAL INTRODUCTION**

Gallium arsenide (GaAs) has semiconducting properties which are different from those of silicon (Si). For example, GaAs, features direct band gap and high electron mobility. Thus, it is used for optical devices such as light emitting diodes (LEDs) and laser diodes (LDs), high frequency amplitude devices such as field effect transistors (FETs), and high electron mobility transistors (HEMTs). These devices are usually fabricated by ion implantation (I.I.) directly into the substrate and/or epitaxial growth using such as vapor phased epitaxy (VPE), liquid phased epitaxy (LPE), metal organic chemical vapor deposition (MOCVD), or molecular beam epitaxy (MBE) on the substrate. Naturally, the quality of these devices depends on the quality of the substrate.

The important substrate properties are those that indicate crystal perfection such as low dislocation density and those that indicate enough quality in electrical properties such as carrier concentration, mobility, and resistivity. These characteristics are controlled during the process of crystal growth by changing growth condition, doped impurity concentration and so on. Group IV impurities such as Si and carbon (C) in III-V compound semiconductors exhibit, especially, very interesting behavior. It should be noted that Group IV impurities are amphoteric impurities, i.e., they act as donors at group III sites, and act as acceptors at group V sites.

There is a basic problem in bulk growth of single crystals. Growth of industrial-sized single crystals is not easy, even for GaAs whose growth technique is considered to be well-known compared with other III-V crystals. Structural defects such as low-angle grain boundary, twin crystals, poly-crystals, and inclusion of impurities are often observed. Quantitative understanding how to control these crystal defects is still obscure. There have been only a few reports on the boat growth method, although it has been studied for a long time.



In this report, the nature of GaAs crystals made by one of the boat growth methods (the gradient freeze method) will be discussed because almost all semi-conducting GaAs crystals are made by the boat growth method at the present time. First, the relationship between structural defects and the solid-liquid interface shape was studied to devise a method of high quality single crystals. Next, the control of unintentionally doped impurities was investigated. By applying the results of these two studies, growth of purer single crystals will be hoped. Finally, the behavior of Si in GaAs was studied, by measuring the electrical properties and lattice parameters of the crystals.

## 1-2. BULK CRYSTAL GROWTH OF GALLIUM ARSENIDE

### 1-2-1. Boat Growth Method and Liquid Encapsulated Czochralski Method

Various GaAs bulk crystal growth methods have been investigated [1] until recently. Generally, the liquid encapsulated Czochralski (LEC) method and the boat growth (BG) method are commonly used for GaAs bulk crystal growth at the present time. The LEC method has been studied extensively because of the requirement for the substrates for GaAs integrated circuits (ICs). However, the requirement for the boat growth crystals is also increased with increasing demands for LEDs and LDs. Recently, new method for growing GaAs bulk crystals has been discussed by combining the characteristic points of both methods, but very little information is currently available concerning these new method.

As a technical problem, it is relatively easy to grow large-diameter crystals using the LEC method [2,3], because the growth direction is vertical. Generally speaking, it is easy to grow the crystals along the direction of gravity. A schematic diagram of the LEC method is illustrated in Fig. 1-1. Contamination from the crucible is small because it is generally made of pyrolytic boron nitride (pBN). The heater is made of carbon. Carbon contamination from the heater compensates n-type native defects in the LEC crystal. As a result, semi-insulating GaAs crystals can be grown without impurity doping. The  $\langle 100 \rangle$  growth direction can be used in the LEC method. Cutting process, perpendicular

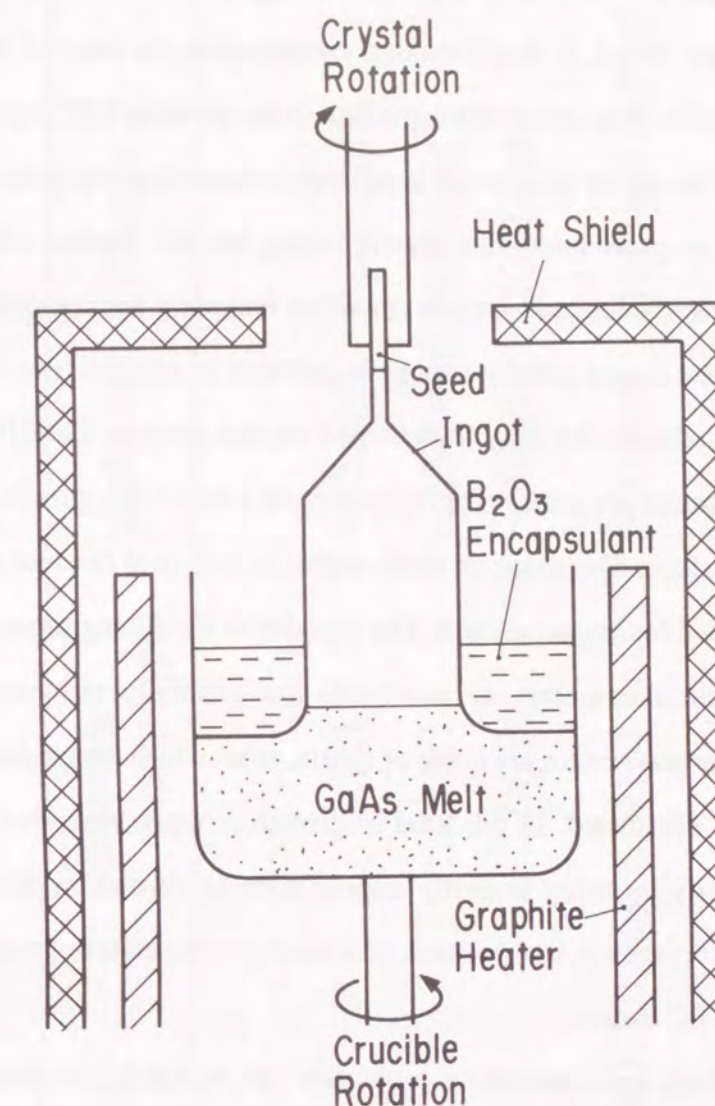


Fig. 1-1 Schematic illustration of the liquid encapsulated Czochralski (LEC) method.



to  $\langle 100 \rangle$  direction, is usually required because the (100) surface substrate is generally used to fabricate electronic devices on. As the LEC crystals have cylindrical shape and the growth is chosen to  $\langle 100 \rangle$  direction, the cutting loss, when round shaped (100) orientated wafers are sliced, is small enough compared to the case of the crystals of  $\langle 111 \rangle$  growth direction. The temperature gradient in the growing LEC crystal is so steep that the dislocation density of the crystals is difficult to control and to reduce.

It is harder to grow large size crystals using the BG method [4] because the growth direction is horizontal and growth condition including temperature gradient and the shape of the solid-liquid interface shape is difficult to control. The  $\langle 111 \rangle$  growth direction is usually chosen for easy direction of crystal growth. The (100) orientated wafers used as substrates are usually cut from a crystal with  $\langle 111 \rangle$  growth direction with an angle of  $54^\circ 44'$  slope. The shape of these wafers is half-oval because a semicircular boat is generally used for crystal growth. The loss due to the slicing process is not small enough because circular wafers as substrates are generally requested for device processing. The boat and reactor are made of quartz, from which contamination of Si and oxygen can not be eliminated. In this kind of growth process, semi-insulating crystals can be obtained only by using impurity doping such as chromium (Cr). Dislocation density of the BG crystals is low because of a smaller temperature gradient compared with those by the LEC method.

To summarize, semi-insulating properties can be easily obtained by the LEC method without using any dopants. On the other hand, the BG crystals have a feature of lower dislocation density. Based on each character, the LEC crystals are used as I.I. substrates and the BG crystals are used as epitaxial substrates. The main use of GaAs substrates is summarized in Table 1-1.

### 1-2-2. The Boat Growth Method

The horizontal Bridgman (HB) method and the gradient freeze (GF) method are the two major boat growth methods for GaAs bulk crystal growth. They are demonstrated schematically in Figs. 1-2 and 1-3, respectively. These two methods are

Table 1-1 Typical purpose of GaAs substrates.

Use	Method	Substrate dopant (type)	Diameter	Off angle	Method
LED					
Red(GaAs <sub>x</sub> P <sub>1-x</sub> ) Printer	VPE	Si(n)	~75mm $\phi$	(100)2°off	LEC, BG
IR	LPE	Si(n)	~63.5mm $\phi$	(100)just	BG
Red(Al <sub>x</sub> Ga <sub>1-x</sub> As)	LPE	Zn(P)	~50mm $\phi$	(100)just	BG
LD (Al <sub>x</sub> Ga <sub>1-x</sub> As)	LPE, MOCVD, MBE	Si(n), Zn(P)	~50mm $\phi$	(100)just or 2°off	BG
FET HEMT	VPE, MOCVD, MBE	Cr(S.I.), none(S.I.)	~75mm $\phi$	(100)just or 2°off	LEC, BG
IC	MBE, I.I.	none (S.I.)	~100mm $\phi$	(100)just	LEC



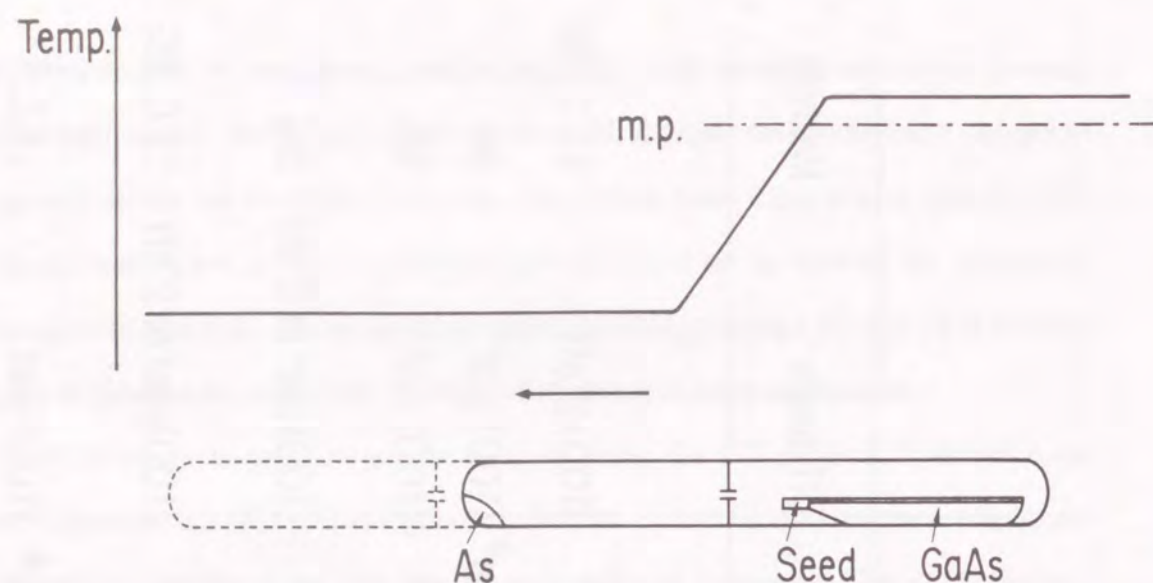


Fig. 1-2 Schematic illustration of the horizontal Bridgman (HB) method.

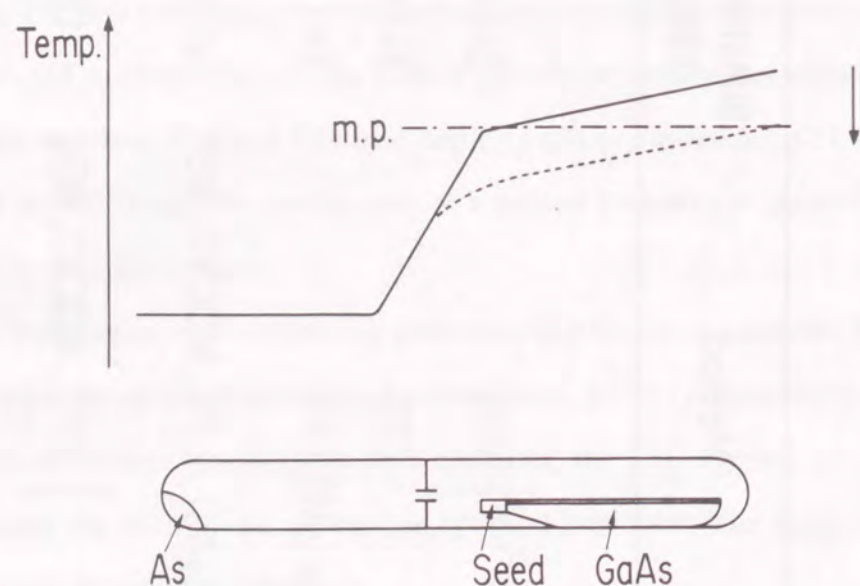


Fig. 1-3 Schematic illustration of the gradient freeze (GF) method.

similar in principle; the difference is only in the temperature changing method. In the HB method, crystal growth is started from a GaAs seed crystal, and is controlled by maintaining the temperature distribution constant by moving the furnace or the reactor. In the GF method, crystal growth is controlled by gradual lowering the temperature.

As well known, the growth temperature is nearby the softening temperature of quartz. Thus, there is a problem that the shape of the quartz reactor deforms more in the higher temperature part. As a result, the characteristics of these two methods are different. The dislocation density of the HB-grown crystals is relatively high because of the steeper temperature gradient after solidification. It is easy to grow long crystals using the HB method because the temperature gradient is not required in all parts of the reactor. In the industrial HB method, a constant temperature area is provided to keep the crystal temperature high enough after solidification. The dislocation density achieved in the GF method is lower because of the smaller temperature gradient. It is difficult to grow long crystals using the GF method, because a temperature gradient is required in all parts of the reactor. In the actual industrial GF method, the temperature distribution is modified so as to enable the growth of longer crystals.

To begin with, the phase diagrams of GaAs should be considered. Figures 1-4 and 1-5 give an x-T (composition - temperature) diagram [5] and a P-T (arsenic vapor pressure - temperature) diagram [6], respectively. The only solid compound in a gallium (Ga) - arsenic (As) system is a GaAs crystal, the melting point of which is 1238 °C, higher than those of both Ga and As. In Fig. 1-5, the curve on the left shows the As vapor pressure of an As-saturated Ga liquid, and the straight line on the right shows the As vapor pressure of pure As. In the case, As vapor pressure of about 1 atm is required for GaAs solidification from a congruent GaAs melt. Keeping the temperature of solid As at 615 °C helps to realize the As vapor pressure at about 1 atm.

The apparatus of the boat growth method is explained as follows. There are two temperature zones; one is lower temperature zone maintained at around 615 °C to control the As vapor pressure of pure As and the other is higher temperature zone maintained at around 1238 °C to grow GaAs crystals. These zones are situated the one next to another.



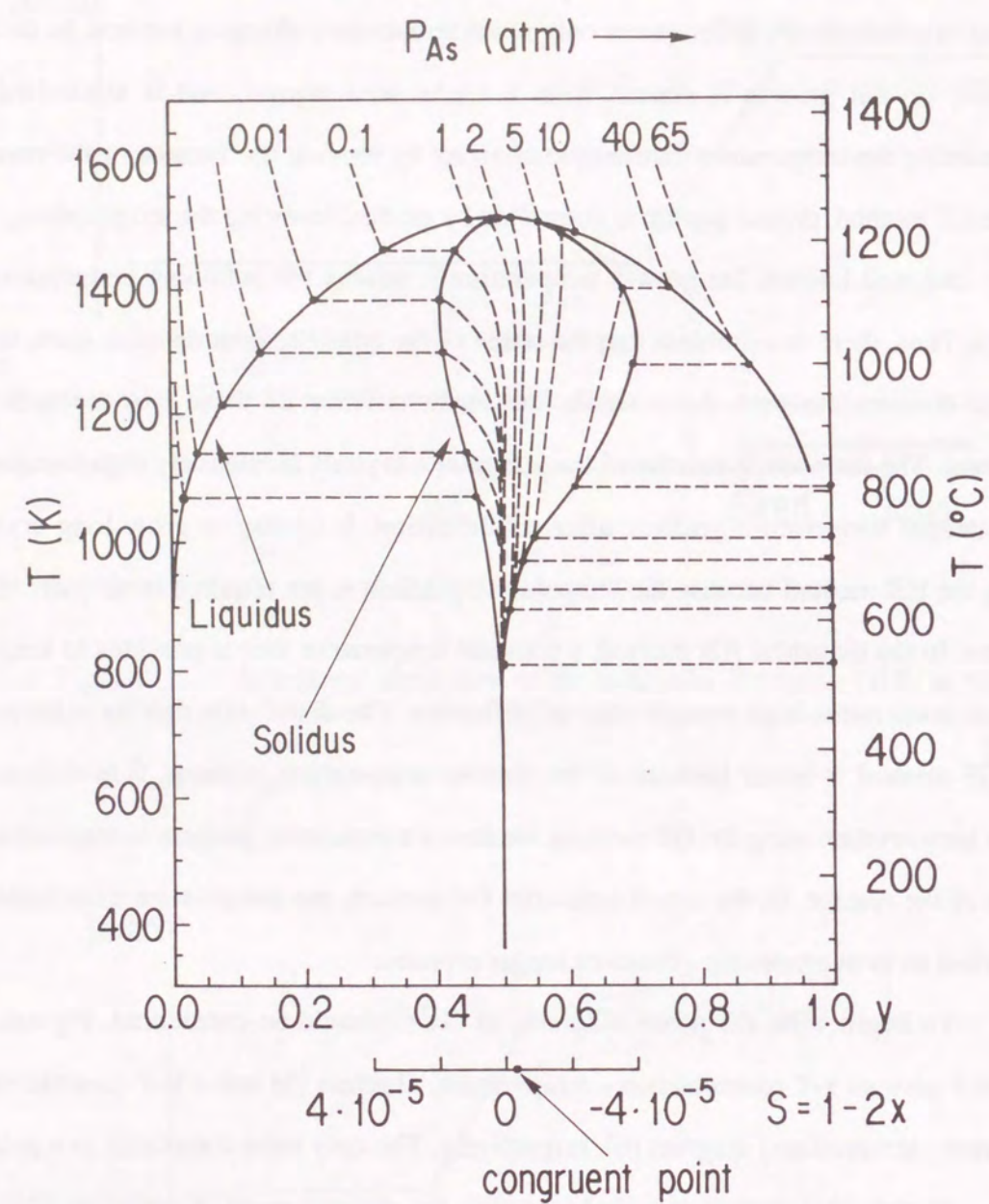


Fig. 1-4 The x-T (composition - temperature) phase diagram for GaAs.

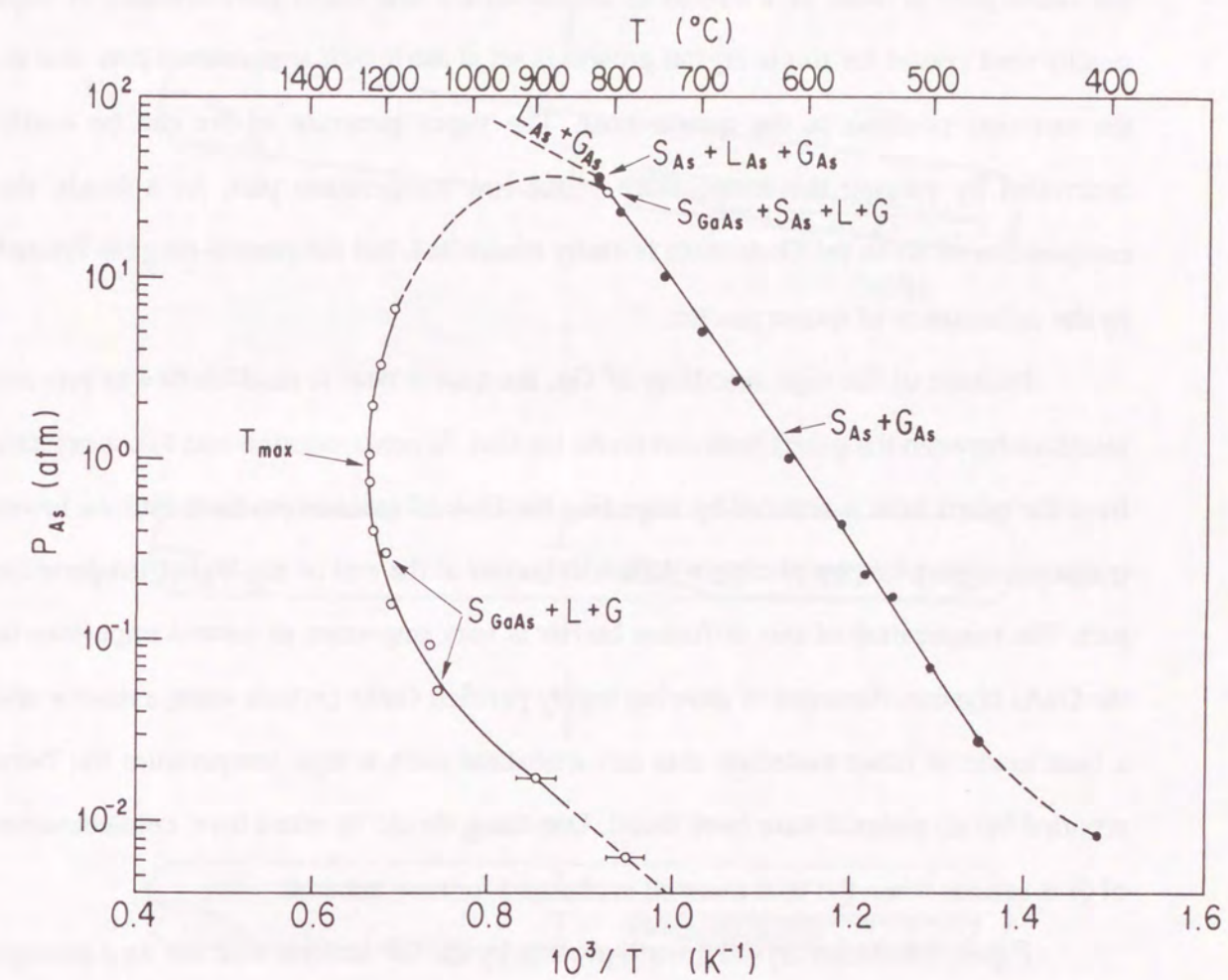


Fig. 1-5 The P-T (As pressure - temperature) phase diagram for GaAs.



Whole vacuum quartz reactor is placed in the furnace. The starting materials in the reactor are pure As in the low temperature part, and pure Ga in the quartz boat in the high temperature part. The starting materials in the quartz boat are not only elemental Ga but GaAs poly-crystals or a hybrid of elemental Ga and GaAs poly-crystals. A high quality seed crystal for single crystal growth is set at the lowest temperature part, that is, the terminal position in the quartz boat. The vapor pressure of As can be easily controlled by varying the temperature of the low temperature part. As a result, the composition of As in the GaAs melt is easily controlled, but the control range is limited by the deformation of quartz reactor.

Because of the high reactivity of Ga, the quartz boat is sand-blasted to prevent reactions between the quartz boat and GaAs (or Ga). Si contamination into GaAs crystals from the quartz boat is reduced by impeding the flow of gaseous products into the lower temperature part, i.e., by placing a diffusion barrier at the end of the higher temperature part. The temperature of this diffusion barrier is very important to control impurities in the GaAs crystals. Attempts of growing highly purified GaAs crystals using a reactor and a boat made of other materials that can withstand such a high temperature has been reported but no material have been found. One thing should be noted here; contamination of Si is serious when the boat material is changed for new material.

Figure 1-6 shows crystal growth process by the GF method with the time passage as a parameter. At the beginning, the furnace must be tilted, so as for the seed not to touch the melt. After small amount of GaAs solid phase have been synthesized on the liquid phase, the solid phase is melted into the liquid. As proceeding this process whole amount of original liquid Ga material is changed into nearly perfect GaAs liquid phase. Next, the temperature profile is adjusted, and the melt touches the seed when the furnace is leveled. Crystal growth is started at the seed by lowering the temperature steadily after melting of the end of the seed crystal. The temperature profile near the solid-liquid interface is very important for the growth of high quality single crystals. The shape of the solid-liquid interface, which is strongly related to the introduction of structural defects, can be controlled by the shape of temperature profile.

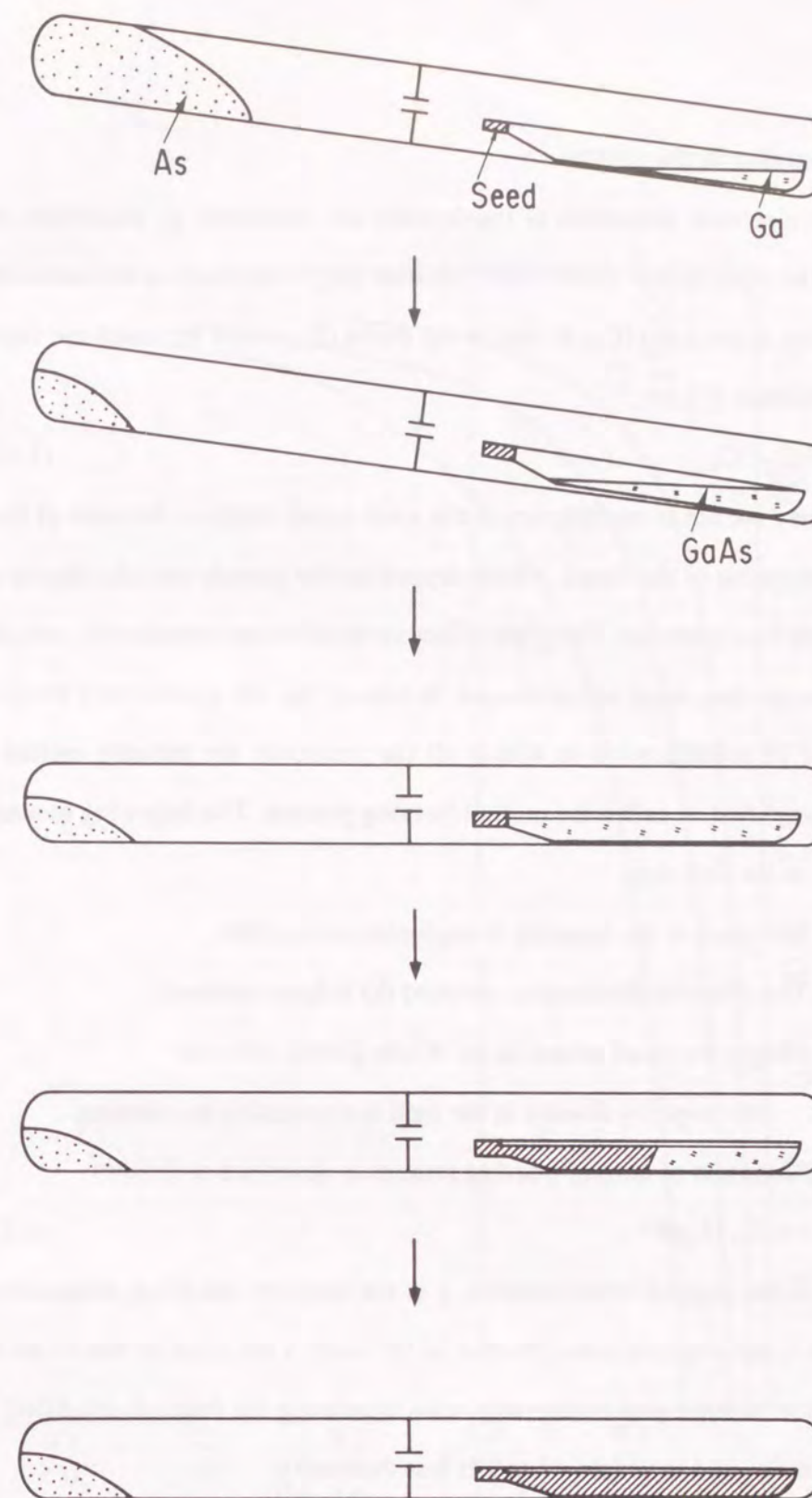


Fig. 1-6 Schematic crystal growth of the GF method along the time passage.



### 1-2-3. Impurities in the crystal

The electrical properties of the crystals are controlled by impurities added into the melt. The equilibrium distribution constant ( $k_0$ ) is defined as the ratio of impurity concentration in the solid ( $C_S$ ) to that in the liquid ( $C_L$ ) when the solid and liquid phases are in equilibrium [1], i.e.,

$$k_0 = C_S / C_L. \quad (1-1)$$

Actually, they are not in equilibrium at the solid-liquid interface because of the effect of impurity migration in the liquid, which depend on the growth rate, the degree of mixing and impurity concentration. Thus, the effective equilibrium constant ( $k$ ), which is quasi-equilibrium number, must be introduced. In both of the HB method and the GF method, the process of solidification in which all the materials are initially melted and then gradually solidified, is called the normal freezing process. The following assumptions are introduced as the first step.

- (1) Diffusion of the impurity is negligible in the solid.
- (2) The effective distribution constant ( $k$ ) is kept constant.
- (3) During the small period in the whole growth process,  
the impurity density in the melt is assumed to be constant.

Impurity distribution of normal freezing process is described as follows.

$$C_S = k C_0 (1-g)^{k-1}, \quad (1-2)$$

where  $C_0$  is the original concentration,  $g$  is the fraction solidified, respectively. In the case of  $k = 1$ , the impurity concentration in the solid is the same as that in the melt. This concentration in solid phase decreases with increasing the fraction solidified when  $k$  is more than unity, and increases when  $k$  is less than unity.

The dopants normally used in GaAs crystals are Cr for semi-insulating property, zinc (Zn) for p-type, and Si for n-type materials, respectively. The effective distribution constant of Cr ( $k_{Cr}$ ) is  $6.4 \times 10^{-4}$ , that of Zn ( $k_{Zn}$ ) is 0.3, and that of Si ( $k_{Si}$ ) is 0.14 [7]. The distribution constants for these impurities are less than unity. As a result, the impurity concentration increases with increasing the fraction solidified, as shown in Fig. 1-7.

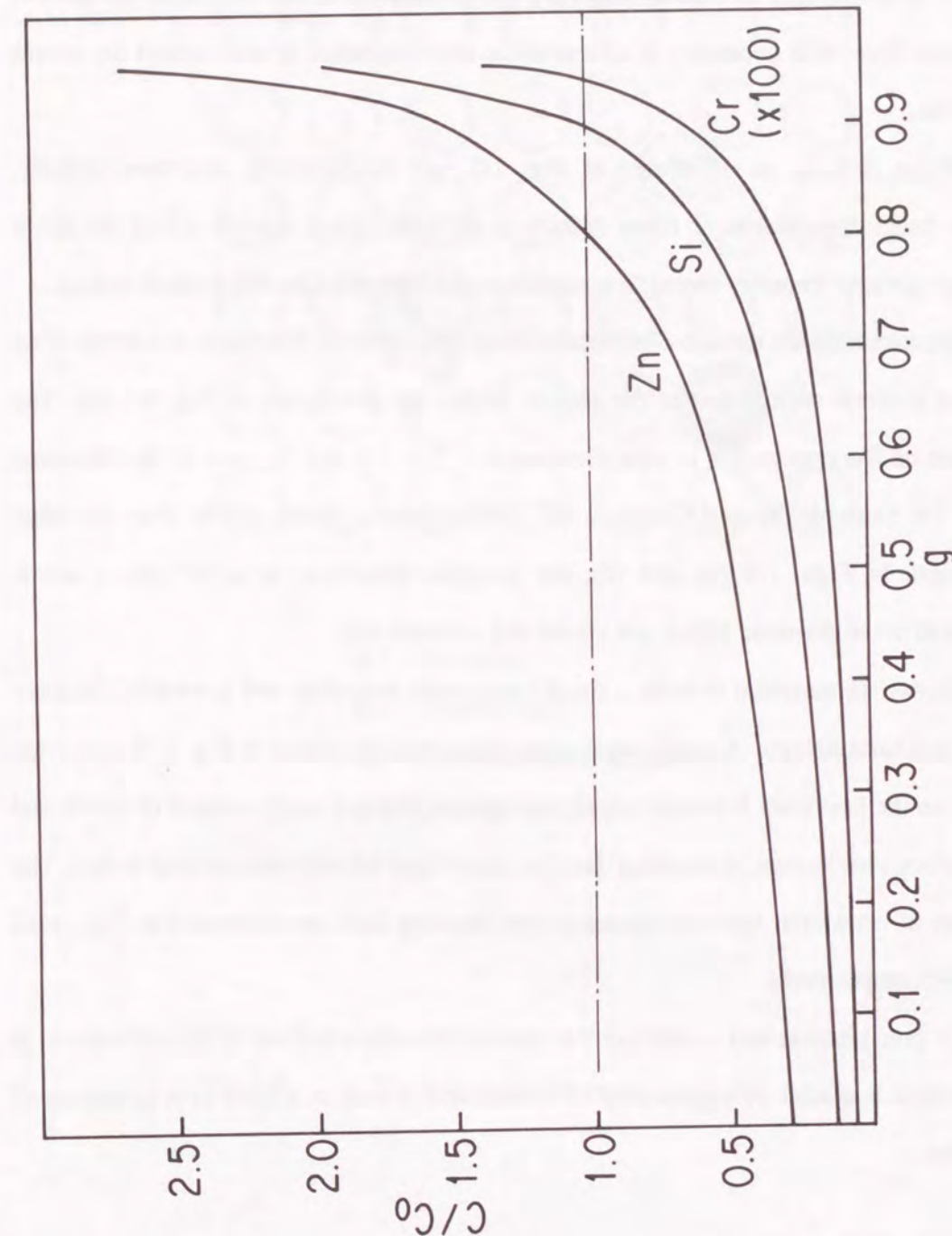


Fig. 1-7 Distribution of Si, Zn, and Cr in GaAs for normal freezing with fraction solidified.



#### 1-2-4. Structural Defect

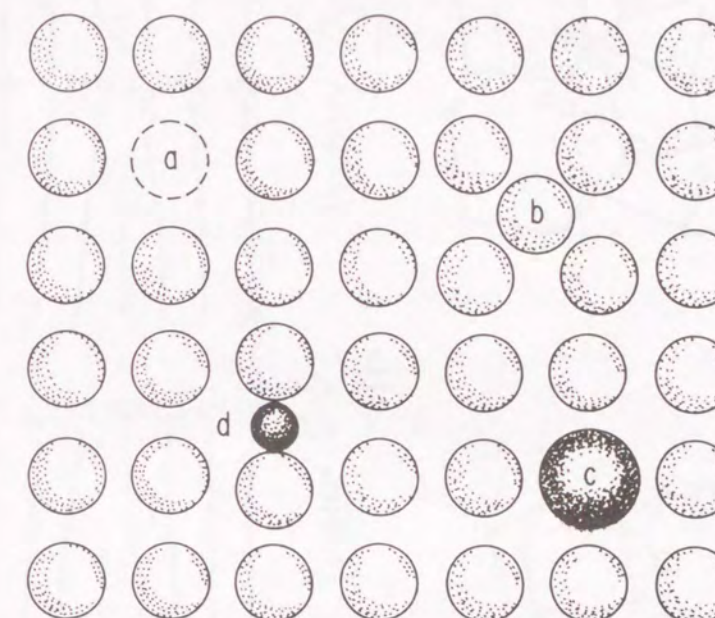
The properties of semiconductors are sensitive not only to impurities but to structural defects which are characterized by the techniques in heat treatment and growth of crystals. Thus, it is necessary to characterize microstructure to understand the nature of materials.

Point defects, as illustrated in Fig. 1-8, are fundamental structural defects. Though direct observation of these defects is difficult, these defects affect electrical properties greatly. Impurity atoms in materials mainly behave like this kind of defects.

Dislocations are the one-dimensional structural defects. The basic structures of an edge and a screw dislocation in the simple lattice are illustrated in Fig. 1-9 (a). The definition of Burgers vector is also illustrated in Fig. 1-9 (a). In case of the diamond lattice, for example Si and GaAs, a  $60^\circ$  dislocation is more stable than an edge dislocation. In Figs. 1-9 (b) and (c), the possible structures of a  $60^\circ$  and a screw dislocation in the diamond lattice are visualized, respectively.

In two dimensional defects, a small angle grain boundary and a stacking fault are typical structural defects. A small angle grain boundary, illustrated in Fig. 1-10 (a), often appears on the boundary between two crystal grains giving a small amount of misfit and edge dislocations in line. A stacking fault is also a kind of two dimensional defect. The structures of interstitial type and vacancy type stacking fault are illustrated in Figs. 1-10 (b) and (c), respectively.

A precipitation and a void are the typical three-dimensional defect structures. A precipitation is a kind of a gathering of atoms, and a void is a kind of a gathering of vacancies.



- a : Vacancy
- b : Interstitial
- c : Substitutional Impurity
- d : Interstitial Impurity

Fig. 1-8 The schematic illustration of point defects.



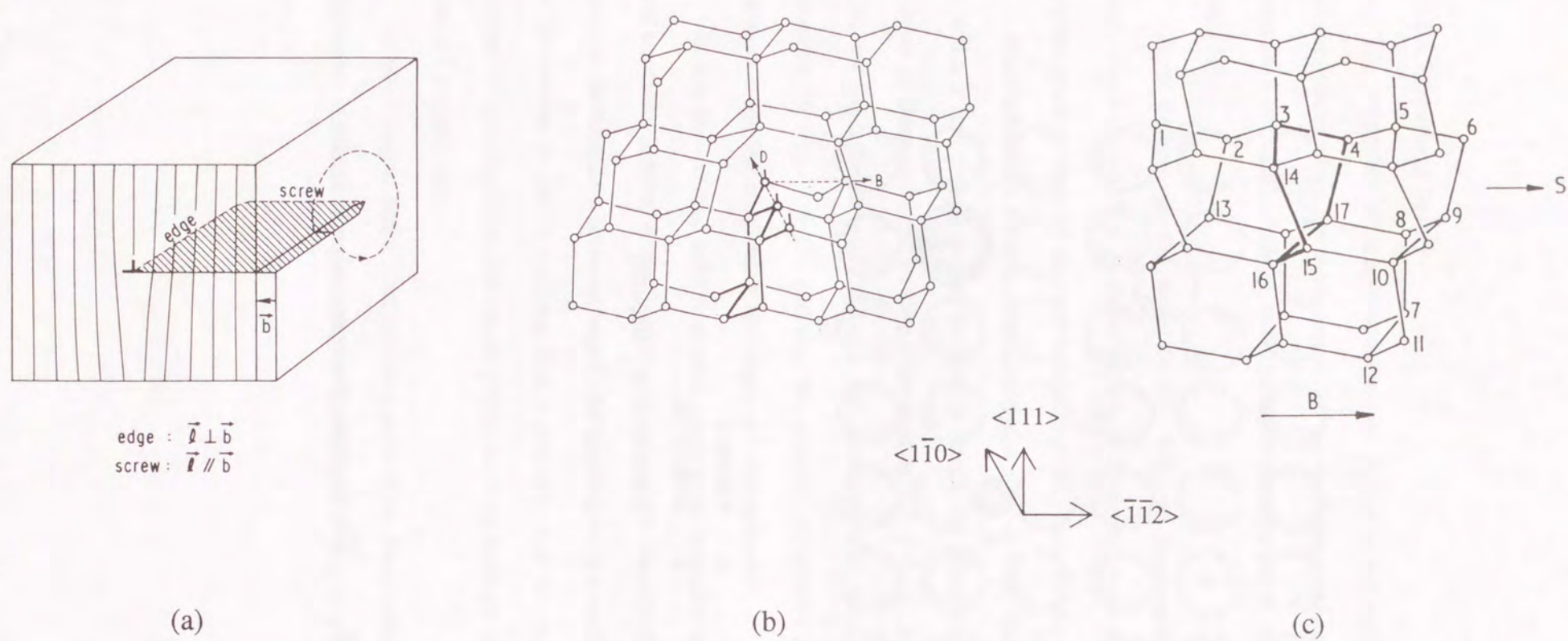


Fig. 1-9 The structures of dislocations and the definition of Burgers vector.  
(a) An edge and a screw dislocation in the simple lattice.  
(b) A  $60^\circ$  dislocation in the diamond lattice.  
(c) A screw dislocation in the diamond lattice.

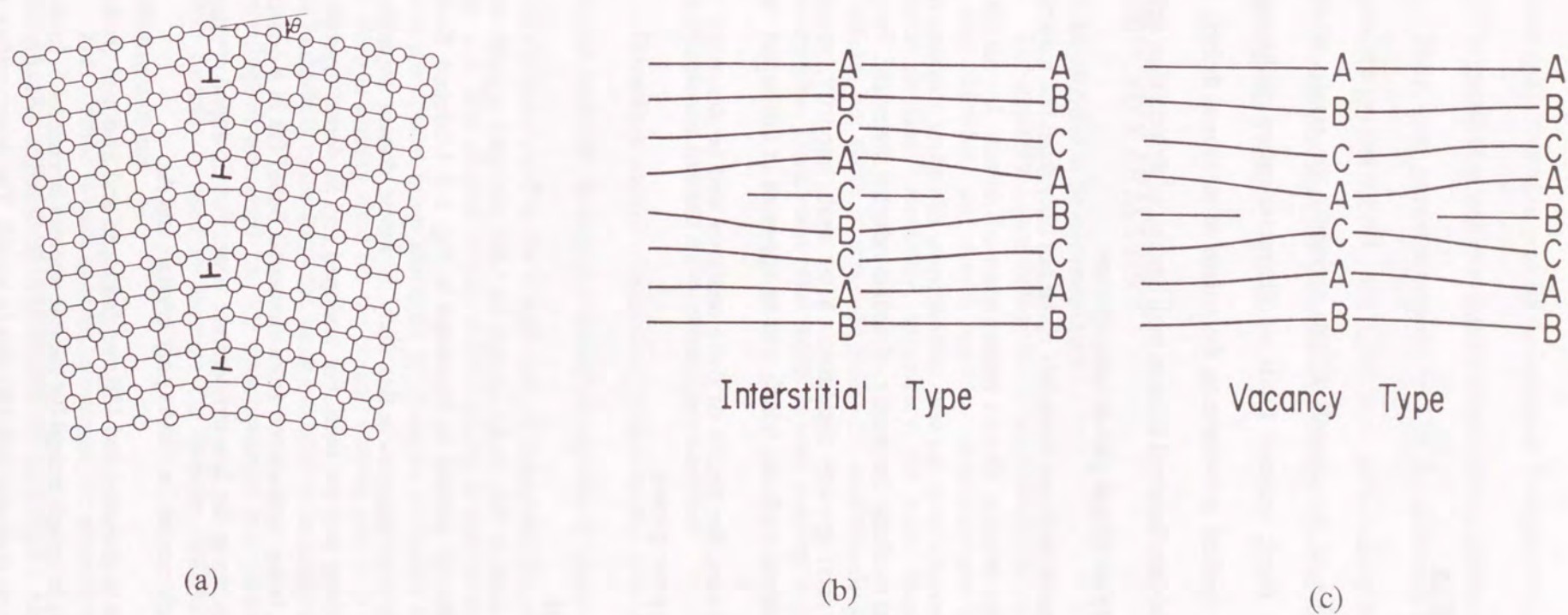


Fig. 1-10 The structures of planar type defects.  
(a) A small angle grain boundary.  
(b) An interstitial type stacking fault.  
(c) A vacancy type stacking fault.



## **2. CRYSTAL EVALUATION**

### **2-1. INTRODUCTION**

The growth condition of the crystals affects seriously the results of crystal evaluation. On the other hand, various kinds of characterization techniques in semiconductors have been applied in evaluating the nature of structural defects [8,9]. Bulk semiconductor materials are believed to have high density of defects than epitaxial materials because of their higher crystal growth temperatures.

Impurities in bulk semiconductor materials come not only from the material but also from the boat and the reactor. Direct observation of defects by an electron microscopy is one of the powerful tools for structural defects. Electrical characterization is the most common way to evaluate the nature of semiconductor materials. First, this chapter introduces the crystal growth condition. After that, impurity, structural, electrical, and optical evaluation methods, which will be appeared in this report, will be also introduced. In some cases, the details of these analyses will be described in the following chapter where they are quoted.

### **2-2. CRYSTAL GROWTH**

Almost all crystals used in this study, except for LEC undoped crystals used in chapter 6, were grown by the GF method as illustrated in Fig. 1-3. Undoped, Si-doped, and Cr-doped GaAs crystals were prepared in this study, however, dopant impurities, for example Si and Cr, were added into the melt. For undoped and Si-doped crystals, they were grown from the melt, being synthesized from elemental liquid Ga in a quartz boat and another material, that is, As in the low temperature zone. For Cr-doped crystals, the melt was synthesized from elemental Ga, GaAs poly-crystals and As.

The boat was 65 mm in diameter and 450 mm (undoped and Si-doped crystals) or 380 mm (Cr-doped crystals) in length except for the one appears in chapter 5. In the case of chapter 5, it was 50 mm in diameter and 380 mm in length. The inner surface of the

boat was sand-blasted to prevent the reactions between the quartz boat and GaAs (or Ga) melt. The quartz boat was evacuated and sealed to eliminate oxygen.

They were grown along the  $\langle 111 \rangle$  As direction by using a seed crystal. A temperature gradient of 0.5 - 1.0 °C/cm was applied along the length of the boat. Crystal growth proceeded together with lowering temperature slowly and steadily, the growth rate was about 3 mm/hr.

### **2-3. IMPURITY ANALYSIS**

#### **2-3-1. Impurities in Semiconductors**

The impurity concentration in the semiconductor materials must be estimated as first step. Residual and doped impurity concentrations can be investigated by the chemical analyses. Recently, secondary ion mass spectroscopy has found wide application, but there is some difficulty in understanding the generation process of secondary ions. Thus, some other methods were used for impurity analysis in this study.

#### **2-3-2. Flameless Atomic Absorption Spectrometry**

Flameless atomic absorption spectrometry (FL-AAS) [9] is one of these applicable methods. It uses the optical absorption of electrons excited from the ground state of the outer shell to the excited state. A schematic diagram of FL-AAS is illustrated in Fig. 2-1. The optical source should supply a narrow width in optical wavelength, because the optical beam absorbed by electron excitation in atom is very narrow. The same atom is usually used for the optical source, that is to say, a hollow cathode lamp whose cathode is made from the same material to be analyzed. A monochromator and a photomultiplier are used for the spectrometer and photo-detector, respectively. A graphite furnace is used to atomize the sample. Standard samples are needed for quantitative analysis.

This method is used in order to estimate the amount of impurities in GaAs. About 1 gram of GaAs is dissolved in hydro-chloric acid (HCl). About 10 µg of this solution is



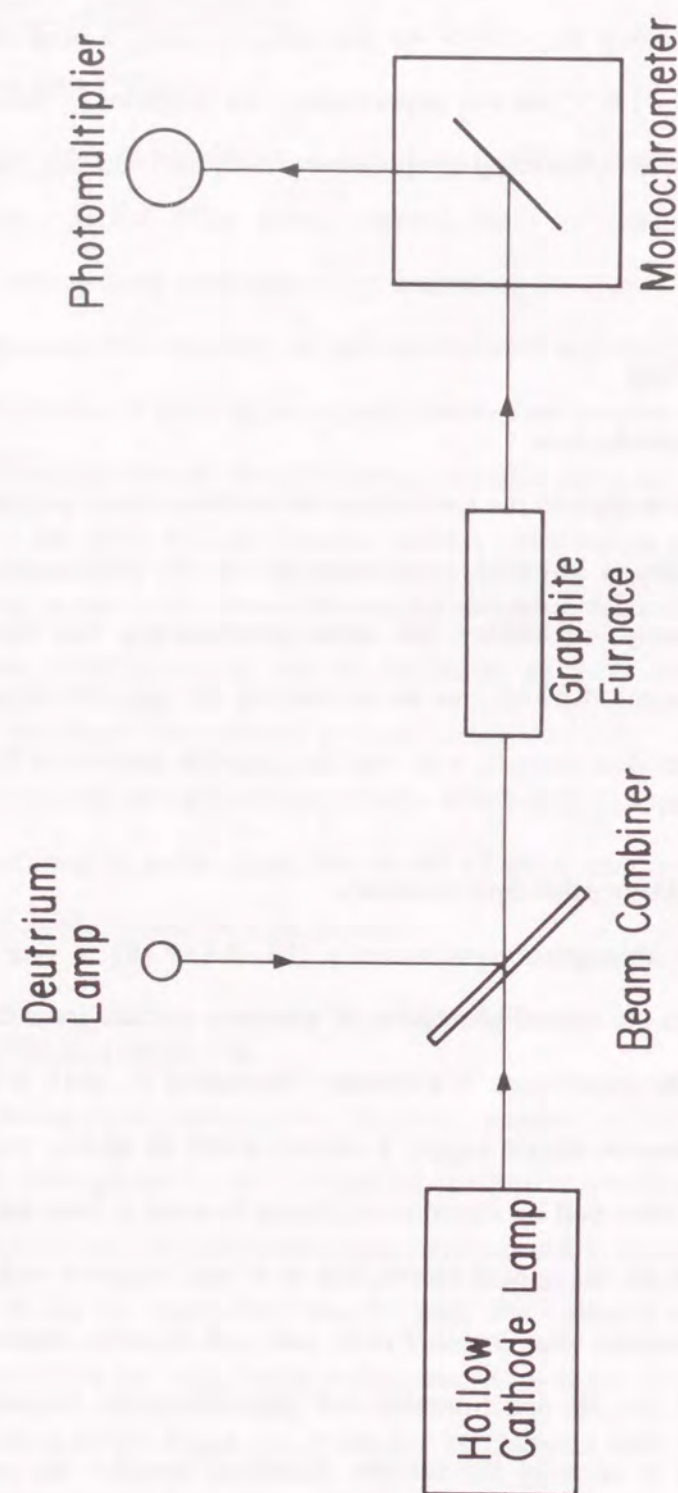


Fig. 2-1 Measurement schematic for flameless atomic absorption spectrometry (FL-AAS).

put into the graphite furnace. The solution is evaporated to ash at a high temperature around 1500 °C. Most of the GaAs matrix is removed by this operation. Residual impurities are atomized at higher temperature: about 2700°C. Analytical sensitivity depends strongly on the temperature. The impurity concentration is calibrated from standard samples made from the solution of pure analyzed material.

### 2-3-2. Secondary Ion Mass Spectroscopy

Secondary ion mass spectroscopy (SIMS) [8] has become a very powerful technique to analyze the impurities in solids. This technique relies on the removal of isolated atoms from the specimen by sputtering and on the analysis of sputtered ionized ions. Most of the sputtered material consists of neutral atoms and can not be analyzed. Only the mass/charge ratio of the ionized atoms can be analyzed by an energy filter and a mass spectrometer. The principle of SIMS is illustrated in Fig. 2-2.

Generally speaking, SIMS has high detection sensitivity for many kinds of elements, but it is not as sensitive as electrical or optical methods. Sputtering yield is the average number of atoms sputtered per an incident primary ion. It depends on the material, its crystallographic orientation, the energy and the incidence angle of the primary ions. The secondary-ion yield is significantly lower than the total yield but can be influenced by the type of primary ion. Electronegative oxygen ( $O_2^+$ ) is a secondary ion yield-enhancing species for electropositive elements (e.g., B and Al in Si) which produce predominantly positive secondary ions. The situation is reversed for electronegative elements (e.g., P, As and Sb in Si) which have greater yields when sputtered with electropositive ions like cesium ( $Cs^+$ ). The secondary ion yield for the elements varies over five to six orders of magnitude. The technique called SIMS also shows strong variations in the secondary ion yield from the same element in different samples or matrices (matrix effect).

Signal intensity can be calculated, in principle, from some factors, knowing the primary ion beam current, the sputter yield, the ionization efficiency, the atomic fraction of the ion to be analyzed, and an instrumental factor. Some of these factors are generally



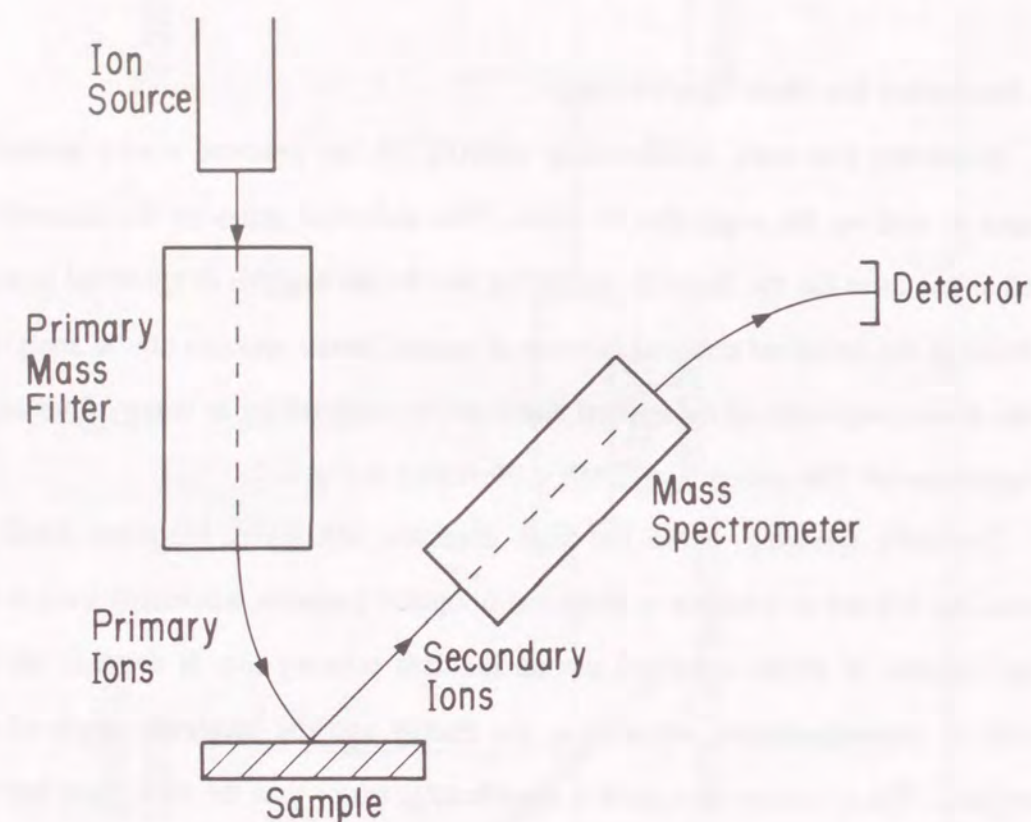


Fig. 2-2 Secondary ion mass spectroscopy (SIMS) schematic.

poorly known, and a successful technique for routine quantitative SIMS analysis has not yet emerged. The most useful approach is to use standard samples. Ion-implanted standards are very useful and also very accurate. When such a standard is measured, the SIMS system is calibrated by integrating the secondary ion yield signal over the entire profile. It should be noted that SIMS analysis determines the total impurity concentration, not the electrically active impurity concentration.

A SIMS sample size of approximately  $5 \times 5 \times 1 \text{ mm}^3$  was used in this study. The surface was previously etched in the solution containing  $\text{H}_2\text{SO}_4:\text{H}_2\text{O}_2:\text{H}_2\text{O} = 10:1:1$  for about 15 min at RT. Primary ion  $\text{O}_2^+$  was used for Mg, Al, Cr, Mn, Fe, and Zn in GaAs matrix, and  $\text{Cs}^+$  was used for C, O, Si, S, Cu, Se, and Te in GaAs analysis.

### 2-3-3. Charged Particle Activation

Charged particle activation (CPA) [8,10-12] is similar to neutron activation analysis (NAA). The difference between CPA and NAA is that of materials to be activated. These are trace analysis methods in which nuclear reactions lead to the production of radioactive isotopes from stable isotopes of the elements in the sample, followed by measurement of the radiation emitted by the desired radio isotopes.

The sample is placed in a nuclear reactor. Generally speaking, those elements that absorb  $^3\text{He}$  (for CPA) or neutrons (for NAA) are found themselves in a highly excited state that is relaxed by  $\beta$  (beta)- and  $\gamma$  (gamma)-ray emission. The sample may also become radioactive. As well known,  $\beta$ -rays have a continuous spectrum and are not useful for elemental identification. On the other hand,  $\gamma$ -rays have well defined, tabulated energies that are usually measured by a germanium (Ge) detector. The  $\gamma$ -ray energy identifies the element, and their intensity determines the amount of contamination. The detection system is well calibrated for quantitative measurements by using standard isotopes.

Oxygen concentration in GaAs was measured by using CPA technique in this study. The products of the  $^{16}\text{O}(^3\text{He},p)^{18}\text{F}$  are position emitters and are used for counting the annihilation of the radiation as a function of time. The half-life time of the products



of  $^{18}\text{F}$  is 109.8 min. The activation of the Si matrix causes no serious interference because of its shorter half-life (2.5 min.). For the GaAs matrix, the beam energy must be carefully chosen because the activation of the GaAs matrix has some influence on the analysis.

In this study, the activated  $^3\text{He}$  energy emitted for 40 min was used at 11 MeV. The measurement energy of  $\gamma$ -rays emitted from  $^{18}\text{F}$  was used at 511 KeV.

## 2-4. STRUCTURAL ANALYSIS

### 2-4-1. Structural Defects of Semiconductors

A knowledge of the structural defects is important in evaluating the character of crystals. It is, especially, unavoidable for bulk materials because they are used as substrates for I.I. and for epitaxy.

Chemical etching is convenient to evaluate structural defects. Electron beams and X-rays are sensitive to lattice spacing. The fundamental theory of these beam techniques derives from Bragg's law [13]. Bragg's law defines constructive interference as occurring when the path difference between waves scattered by successive parallel planes of atoms of interplana spacing ( $d$ ) is equal to an integral number of wavelength. If  $\theta$  is the angle of incidence, then, as shown in Fig. 2-3, the path difference between two waves is  $2d \sin \theta$ ; hence Bragg's law is:

$$2d \sin \theta = n\lambda, \quad (2-1)$$

where  $n$  is the order of reflection and  $\lambda$  is the wavelength of incidence. This relationship is used in lattice spacing measurement, X-ray topography and transmission electron microscopy.

### 2-4-2. Chemical Etching

Etch pit density (EPD) is commonly used for evaluating dislocation density. Figures 2-4 and 2-5 show a GaAs (100) surface etched in the molten KOH for about 10 min and a GaAs (111) As surface etched in the solution  $\text{HNO}_3:\text{H}_2\text{O}_2:\text{H}_2\text{O} = 3:1:4 +$

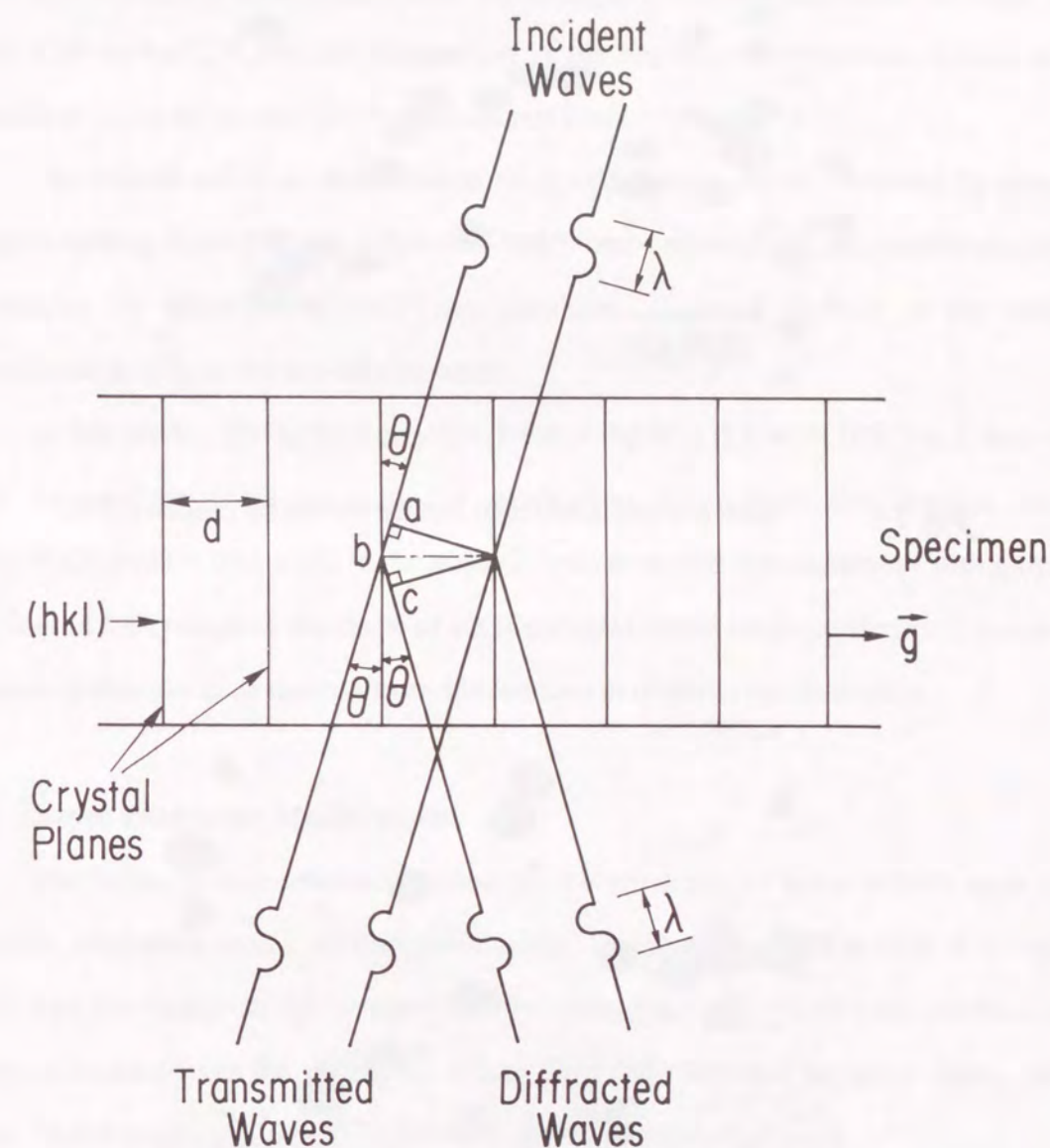


Fig. 2-3 The Bragg reflection.



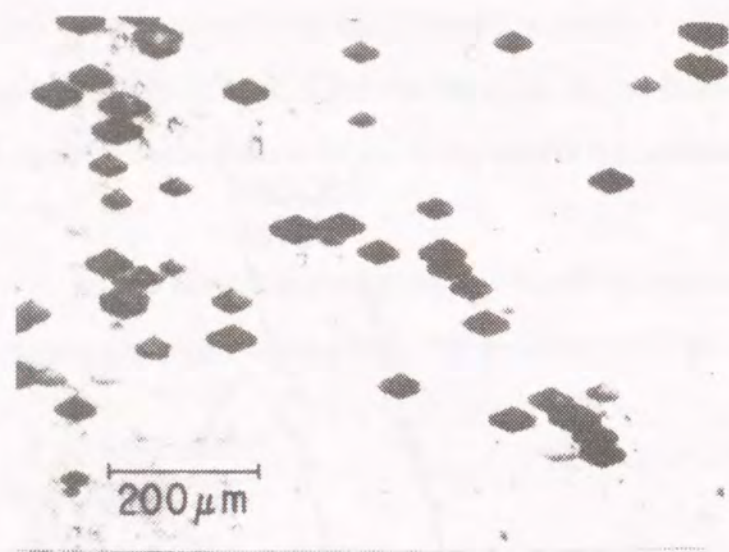


Fig. 2-4 Etch pits of GaAs (100) surface etched by molten KOH.

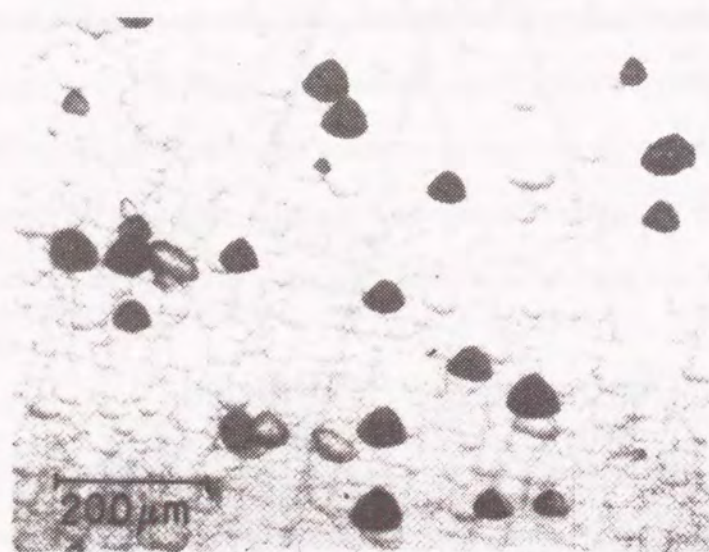


Fig. 2-5 Etch pits of GaAs (111) surface etched by  $\text{HNO}_3:\text{HF}:\text{H}_2\text{O} = 3:1:4$  + 0.3 wt%  $\text{AgNO}_3$ .

$\text{AgNO}_3$  0.3 wt% at RT for 3 min, respectively. Typical etching solution for the etch pits evaluation are listed at Table 2-1 [14-17].

The etched surfaces involve other information. For example, details of S-pits of etched GaP surface [18,19] and observation of the impurity concentration around the dislocations in GaAs crystals [20] have been reported.

The overall and local distributions of crystal defects can be observed by using chemical etching. Sometimes, a differential interference microscope and controlled light are needed for observation. Generally speaking, chemical etching is the most conventional technique for crystal evaluation.

In this study,  $\text{HNO}_3:\text{H}_2\text{O}_2:\text{H}_2\text{O} = 3:1:4$  +  $\text{AgNO}_3$  0.3 wt% (RT for 3 min on (111) As surface [14]) is used for evaluating dislocation distribution, and  $\text{H}_2\text{SO}_4:\text{H}_2\text{O}_2:\text{H}_2\text{O} = 10:1:1$  (10 °C for about 25 min under the illumination of strong light [21]) is used for evaluating the shape of striation (solid-liquid interface shape). This kind of pattern is thought to be derived from fluctuations in impurity concentration.

#### 2-4-3. Lattice Parameter Measurement

The lattice parameters are affected by the existence of point defects such as vacancies, interstitial atoms, and impurity atoms on the normal lattice sites. It is well known that the change of lattice parameter by changing the impurity concentration is usually estimated from the difference of covalent radii between impurity atoms and matrix. Well known numerical relationship is called Vegard's law.

So-called Bond method [22,23] is used to estimate lattice parameters as illustrated in Fig. 2-6. Lattice parameters can be measured to a few parts in a million by this method. The apparatus measures the angle between two reflecting positions of the crystals. The reading of the crystal position on a divided circle for one position is noted  $R_1$ , and the position for the second is noted  $R_2$ . The following is readily shown, on the conditions for  $R_2 > R_1$  and  $R = 0$  not between  $R_1$  and  $R_2$ :

$$\theta = 90^\circ - (R_2 - R_1) / 2, \quad (2-2)$$



Table 2-1 Typical etch pit etching solution for GaAs.

Name	Etchant	Surface	Ref
Schell	1 HNO <sub>3</sub> : 3 H <sub>2</sub> O	(111) Ga	R & C
	1 HF : 1~2 H <sub>2</sub> O : 4~6 H <sub>2</sub> O	(111) Ga	
R - C	1~2 HF : 3 HNO <sub>3</sub> : 0~4 H <sub>2</sub> O (approx. 1% AgNO <sub>3</sub> added)	(111) As	
A - B	4 HF : 5 H <sub>2</sub> O (approx 0.002% Ag, 20% CrO <sub>3</sub> added)	(100), (110), (111)	A & B
	Molten KOH	(100), (110), (111)	

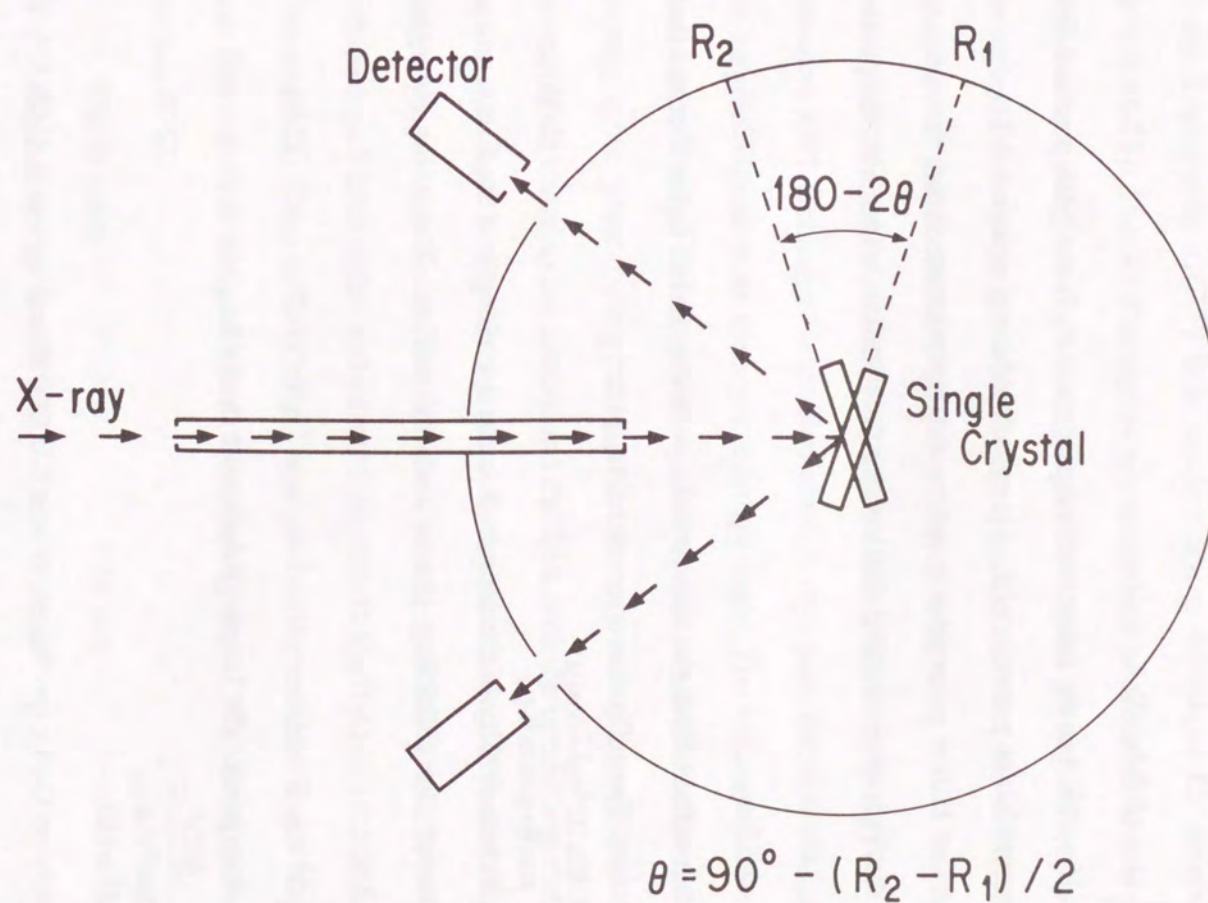


Fig. 2-6 Schematic illustration of the Bond method for lattice parameter measurement.



where  $\theta$  is the Bragg angle. This method of determining  $\theta$  eliminates the eccentricity error, the absorption error and the zero error [22].

The peak position is determined by the least square fitting of the Cauchy distribution function from measured X-ray intensity and measurement position. The function is:

$$I(\theta) = \frac{2I}{\pi\delta} (1 + (2(\theta - \theta_0)/\delta)^2)^{-1}, \quad (2-3)$$

where  $\delta$  is the half width,  $I$  is the integrated intensity, and  $\theta_0$  is the peak position. From this  $\theta$ , a measurement lattice parameter ( $a_{\text{obs}}$ ) is calculated using equation 2-1.

The observed lattice parameter involves the temperature error, the reflection error, the axial divergence error, and the Lorenz-polarization error. The temperature correction ( $\Delta a_{\text{temp}}$ ) is:

$$\Delta a_{\text{temp}} = \alpha \Delta T a_{\text{obs}}, \quad (2-4)$$

where  $\Delta T$  is the deviation from the standard temperature, and  $\alpha$  is the thermal linear expansion coefficient. The reflection correction ( $\Delta a_{\text{refr}}$ ) is:

$$\Delta a_{\text{refr}} = \frac{4.48 \times 10^{-6} n_0 \lambda^2 \cos(\mu)}{\sin(\theta + \mu) \sin(\theta - \mu)}, \quad (2-5)$$

where  $n_0$  is the electron density of the sample,  $\lambda$  is the wavelength of the X-ray, and  $\mu$  is the rotation between the reflecting planes and the surface. The axial divergence correction ( $\Delta a_{\text{div}}$ ) is:

$$\Delta a_{\text{div}} = \frac{1}{6} \Delta^2 a_{\text{obs}}, \quad (2-6)$$

where  $\Delta$  is axial divergence. The Lorenz-polarization error ( $\Delta a_{\text{Lp}}$ ) is:

$$\Delta a_{\text{Lp}} = \frac{(\delta/2)^2}{(2 \sin^2 \theta) a_{\text{obs}}}, \quad (2-7)$$

where  $\delta$  is the half width.

In this study on GaAs specimens,  $\alpha$  was 0.0000058 and  $n_0$  was  $1.4167 \text{ \AA}^{-1}$ . The value of  $\Delta$  was used as 0.00278 rad for the present apparatus. In this study, {111} wafers with 1 mm thickness were sliced from GaAs ingots, and the side to be measured was polished. Square shaped samples, of approximately 10 mm x 10 mm, were cut from each wafer. These pieces were etched on both sides in a solution of  $\text{H}_2\text{SO}_4:\text{H}_2\text{O}_2:\text{H}_2\text{O} = 10:1:1$  for about 20 min at RT to remove surface damage completely. The sample was fixed at the crystal fixture with a little amount of water to prevent mechanical stress. The

(444) reflection of GaAs was used with Cu K $\alpha$ 1 radiation (0.15405981 nm wavelength [24]) at  $25 \pm 1^\circ \text{C}$  to measure the lattice parameter.

#### 2-4-4. X-ray Topography

X-ray Topography (XRT) is a nondestructive technique for determining structural defects [8,25]. The XRT image is not magnified because no lenses can be used. It is therefore not a high-resolution technique. But it does give microscopic information only through the enlargement of the photograph. The microscopic information has the same resolution as that obtained using the etching technique.

The transmission XRT (Lang method), illustrated in Fig. 2-7, is the most common XRT technique. Monochromatic X-rays pass through a narrow slit and strike the sample aligned at an appropriate Bragg angle. The tall and narrow primary beam is transmitted through the sample and strikes a lead screen. The diffracted beam falls on the photographic plate through a slit in the screen. A topography is generated by synchronous scanning the sample and the film, with the screen held stationary.

A sample with a GaAs (111) surface plane and a (220) reflecting plane were used for imaging in this study. The thickness was around 250  $\mu\text{m}$ . The sample had one side polished and both sides etched with  $\text{H}_2\text{SO}_4:\text{H}_2\text{O}_2:\text{H}_2\text{O} = 10:1:1$  for 30 min at RT. Characteristic X-ray called CuK $\alpha$ 1 was used as the incident X-ray beam. The film used was Ilford nuclear research plate (Emulsion Type L4). The development process was as follows:

Dip in water	10 min
Copinal (at 10 °C with ice)	20 min
(the ice is melted)	20 min
Stop (water + acetic acid)	10 min
Fix (Fuji fix)	2 - 3 hr
Flowing water	over 3 hr

The defect image was observed after image enlargement process.



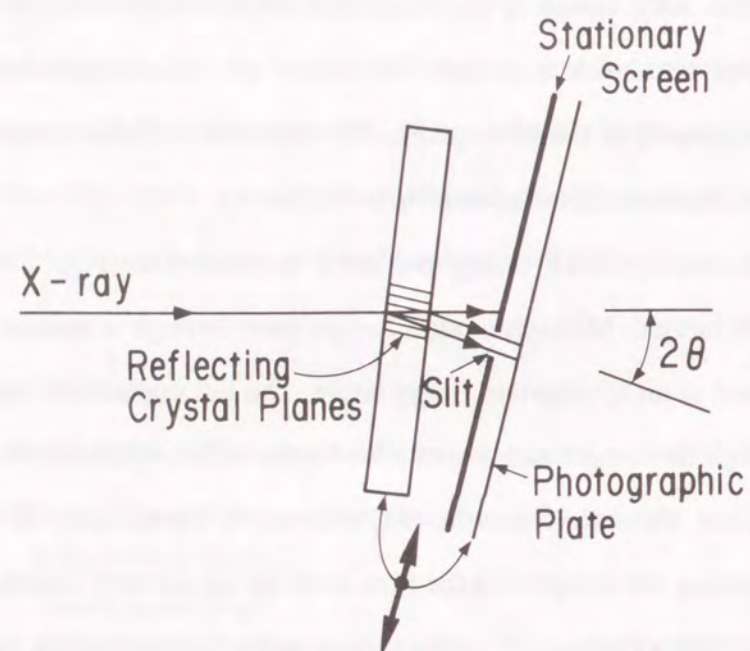


Fig. 2-7 Schematic illustration of Lang transmission X-ray topography.

#### 2-4-5. Transmission Electron Microscopy

Transmission electron microscopy (TEM) was originally used for highly magnified sample images [8,13]. The observation using TEM is, in principle, similar to that of optical microscopes; both contain a series of lenses to magnify the image of specimens.

A schematic TEM is shown in Fig. 2-8. Electrons from an electron gun are accelerated at high voltages - typically 100 to 400 kV - and focused on the sample by condenser lenses. The static beam has a diameter of a few  $\mu\text{m}$ . The sample must be thin enough (a few tens to a few hundreds of nm) for electrons to be transmitted through it. As a result, the resolution of TEM is higher than scanning electron microscopy (SEM) because the electron beam does not have a chance to spread like a "balloon" in the thin sample. The transmitted and forward scattered electrons from a diffraction pattern are focused on the back focal plane (Ewald sphere) and a magnified image is focused on the image plane. With additional lenses, either the image or the diffraction pattern is projected onto a screen for viewing or for photographic recording.

Images formed using only transmitted electrons are known as bright-field images and images formed using a specific diffracted beam are called dark-field images, as illustrated in Fig. 2-8. Few electrons are absorbed in the sample. Sometimes, absorbed electrons lead to sample heating, which can change the structure of the sample during the observation.

High-resolution TEM (HREM) gives structural information on the scale of the atomic size level, in the case of planer defects such as interface and stacking faults. In lattice imaging technique using HREM, a number of different diffracted beams are combined to give an interference image. Several photographs of lattice images must be taken to determine the appropriate focus condition. The focus condition must be changed from over-focus to under-focus condition. The result on these image condition must be compared with the numerical simulation of the image contrast given by dynamical theory.



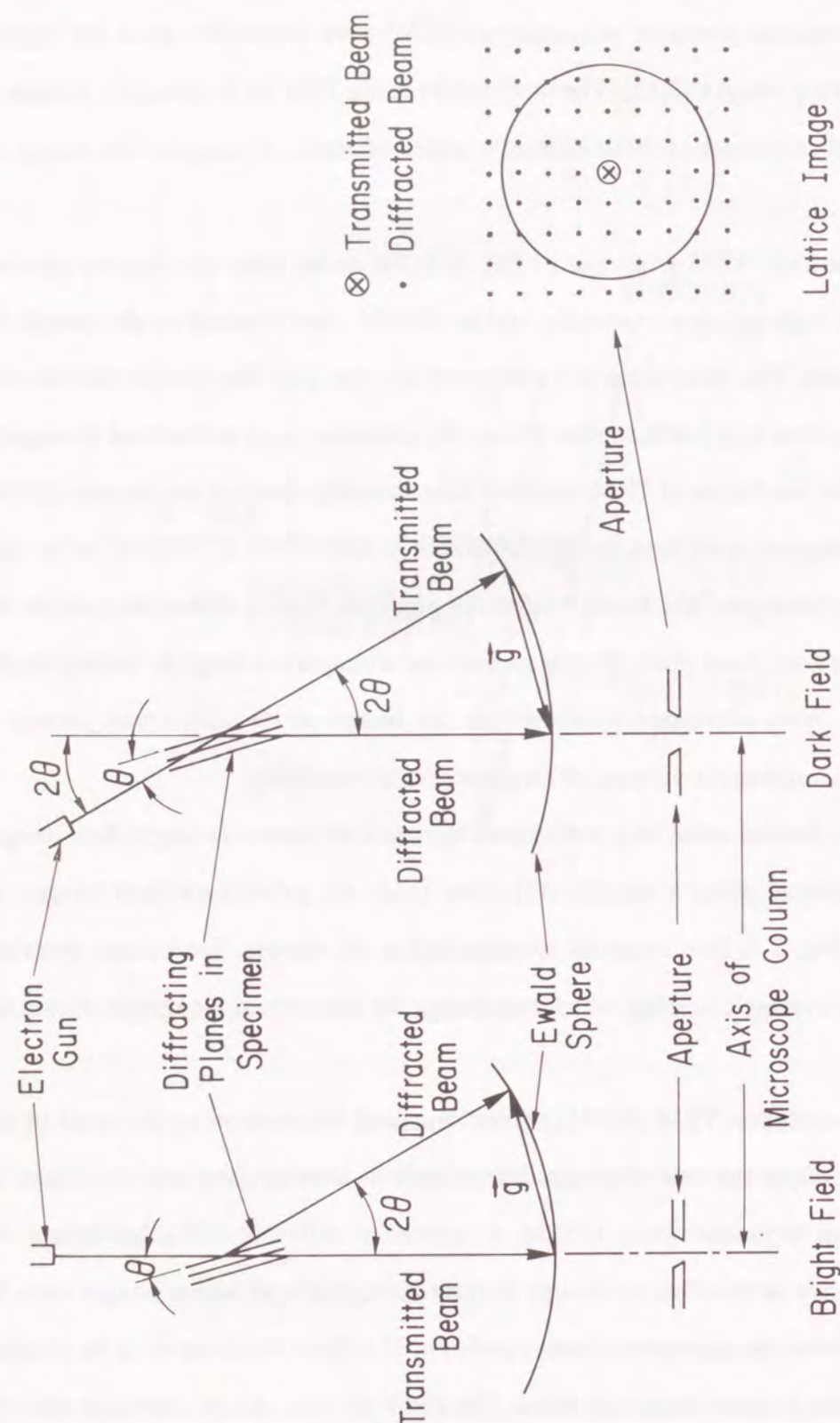


Fig. 2-8 Transmission electron microscopy (TEM) schematic.

In this study, specimens for TEM observation were fabricated as follows: Wafers with a thickness of 0.35 mm on (111) orientation were cut from the ingots. Some disks of 3 mm in diameter were also cut from the sample. A "pot-hole" of 1 mm in diameter and 0.28 mm in depth was dug by an ultrasonic drill at the center of the surface of each disk. Next, these disks were dipped in a solution ( $\text{H}_2\text{SO}_4:\text{H}_2\text{O}_2:\text{H}_2\text{O} = 3:1:1$ ) for about 10 sec at 50 °C in order to get metallic gloss on the specimen surface. After this treatment the disks were transferred to another solution ( $\text{HNO}_3:\text{HF}:\text{H}_2\text{O} = 3:3:4$ ) and kept at 25 °C until small holes formed around which were wedge shaped and suitable for TEM observations.

Bright-field images, dark-field images, and HREM were used in this analysis. The acceleration voltage was fixed at 200 kV.

## 2-5. ELECTRICAL AND OPTICAL ANALYSIS

### 2-5-1. Electrical and Optical Properties in Semiconductors

Electrical properties are the basic semiconductor material parameters. Carrier concentration and Hall mobility are particularly important for the characterization of bulk crystal. These characteristics depend greatly on the kind of semiconductor, the amount of dopant, and unintentionally doped impurities. Deep levels are very difficult to find out, but greatly influence their electrical properties. Photoluminescence is a useful tool in analyzing shallow and deep levels. In this study, resistivity, carrier concentration, and Hall mobility were measured using the Van der Pauw method. Deep level transient spectroscopy and photoluminescence were applied for deep level analysis.

### 2-5-2. Resistivity, Carrier Concentration, and Hall Mobility

Resistivity, carrier concentration, and Hall mobility are commonly measured by using the Van der Pauw method [8,26], where the resistivity is measured by a kind of the four-point probe technique. This is one of the most common techniques to estimate semiconductor resistivity, because two-point probe method requires a pair of reliable



ohmic contacts. In the present four-point probe method, contact resistance and spreading resistance are negligible in principle.

Van der Pauw [26] showed how to estimate specific resistivity of a flat sample of arbitrary shape without defining a pair of current probes. In case, the following conditions are satisfied:

- (1) the contacts are on the periphery of the sample,
- (2) the contacts are sufficiently small compared to sample size,
- (3) the sample thickness is approximately uniform,
- (4) the sample does not contain any isolated holes among the four contacts.

Let us consider a flat sample of a conducting material with arbitrary shape, with contacts 1, 2, 3, and 4 along the periphery as illustrated in Fig. 2-9 (a), which satisfies the above conditions. The resistance  $R_{12,34}$  is defined as:

$$R_{12,34} = V_{34} / I_{12}, \quad (2-8)$$

where the current  $I_{12}$  enters the sample through contact 1 and goes out through contact 2, and  $V_{34} = V_3 - V_4$  is the voltage difference between the contact 3 and 4.  $R_{23,41}$  is defined similarly. The resistivity ( $\rho$ ) is given by:

$$\rho = (\pi t / \ln(2)) \frac{(R_{12,34} + R_{23,41}) F}{2}, \quad (2-9)$$

where  $t$  is the sample thickness and  $F$  is a function only of the ratio  $R_r = R_{12,34} / R_{23,41}$ , satisfying the relation:

$$(R_r - 1) / (R_r + 1) = \frac{F}{\ln(2)} \arccos\left(\frac{\exp(\ln(2) / F)}{2}\right). \quad (2-10)$$

The function  $F$  on the right side of equation 2-10 depends only on  $R_r$ .

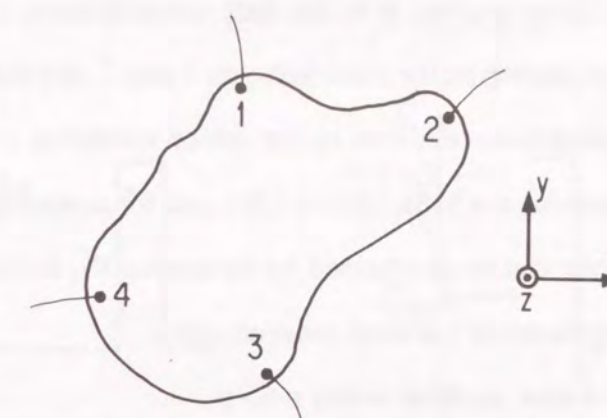
The Van der Pauw Hall mobility is given by the similar expression to the Hall mobility:

$$\mu_H = \text{abs}(R_H) / \rho = \text{abs}(R_H) \sigma, \quad (2-11)$$

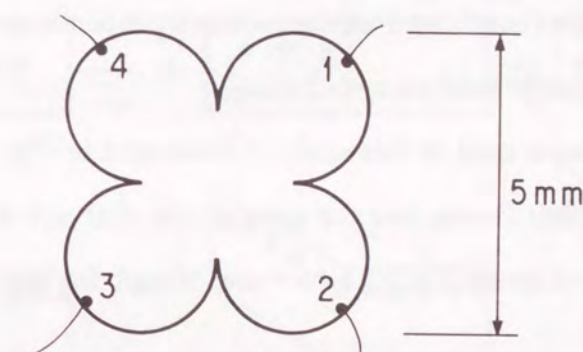
with the Hall coefficient ( $R_H$ ) given by:

$$R_H = t \Delta V_{34} / (2BI_{12}), \quad (2-12)$$

where  $\sigma$  is the conductivity ( $\sigma = 1/\rho$ ) and  $\Delta V_{34} = V_{34} \text{ (for } +B) - V_{34} \text{ (for } -B)$  with  $I_{12}$  flowing in the specimen through the terminal 1 and terminal 2, and  $B$  is the magnetic field applied in the  $z$ -direction.



(a)



(b)

Fig. 2-9 (a) A lamella-type Van der Pauw Hall sample and (b) A Van der Pauw Hall sample used in this study.



For extrinsic p-type material, where  $p \gg n$ :

$$R_H = r / (qp), \quad (2-13)$$

where  $q$  is the electronic charge,  $p$  is the hole concentration, and  $n$  is the electron concentration. The scattering factor  $r$  lies between 1 and 2, depending on the scattering mechanism in the semiconductor, that is, for lattice scattering  $r = 3\pi / 8 = 1.18$ , for ionized impurity scattering  $r = 315\pi / 512 = 1.93$ , and for neutral impurity scattering  $r = 1$ . The scattering factor can be determined by measuring  $R_H$  in the high magnetic field limit, and a scattering factor of 1 is used conventionally.

For extrinsic n-type material, where  $n \gg p$ :

$$R_H = r / (qn), \quad (2-14)$$

When comparable number of holes and electrons are present, the expression of the Hall coefficient becomes:

$$R_H = \frac{r [(p - b^2n) + (\mu_n B)^2 (p - n)]}{q [(p + bn)^2 + (\mu_n B)^2 (p - n)^2]}, \quad (2-15)$$

This expression is rather complicated and its sensitivity depends on the mobility ratio  $b = \mu_n / \mu_p$  and on the magnetic field strength  $B$ .

The sample shape used in this study is illustrated in Fig. 2-9 (b). The applied magnetic field was 3000 Gauss, and the current was 500 mA for a sample with the carrier concentration of above  $1 \times 10^{17} \text{ cm}^{-3}$  and 50 mA for that with a concentration below  $1 \times 10^{17} \text{ cm}^{-3}$ .

### 2-5-3. Deep Level Transient Spectroscopy

Deep level transient spectroscopy (DLTS) is based on the technique called capacitance measurements. The emission power and capture transient analysis was only fully realized when automated data acquisition techniques were adopted [8,27].

Lang introduced the rate window concept to determine deep level characterization. If the  $C$ - $t$  (capacitance - time) curve from a transient capacitance experiment as illustrated in Fig. 2-10, is processed so that a selected decay rate produces a maximum output, a signal whose decay time changes monotonically with time reaches a peak when the rate passes through the rate window of a box-car averager or the

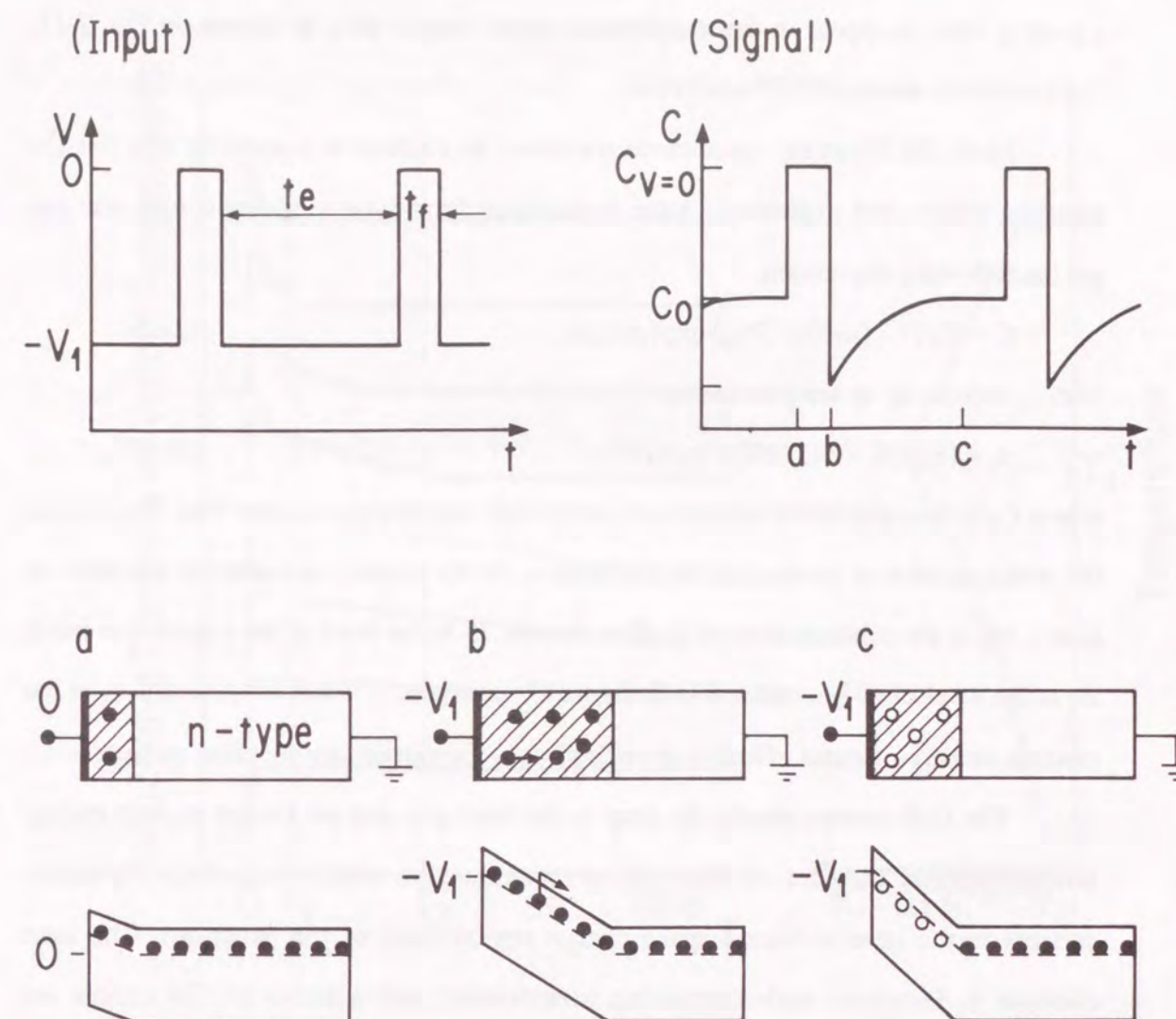


Fig. 2-10 Relationship between capacitance and time. A Schottky diode for a: zero bias, b: reverse bias at  $t = 0$ , c: reverse bias as  $t \rightarrow \infty$ . The applied voltage waveform is shown (Input); (Output) is the capacitance transient.



frequency of a lock-in amplifier. When observing a repetitive C-t transient through such a rate window while varying the decay time constant by varying the sample temperature, a peak is seen to appear in the temperature versus output plot, as shown on Fig. 2-11. Such a plot is named a DLTS spectrum.

Next, DLTS using capacitance transients is explained. Assuming that the C-t transient follows the exponential time dependence for n-type semiconductors, one can get the following expression,

$$C = C_0 [1 - (n_T(0) / 2N_D) \exp(-t / \tau_e)] , \quad (2-16)$$

with  $\tau_e$  depending on temperature as:

$$\tau_e = [\exp(E_c - E_T) / kT] / (\gamma_n \sigma_n T^2) , \quad (2-17)$$

where  $C_0$  is the capacitance without any deep-level impurities at reverse bias  $-V_1$ ,  $n_T(t)$  is the concentration of generation-recombination (G-R) centers occupied by electrons at time  $t$ ,  $N_D$  is the concentration of shallow donors,  $E_c$  is the level of the conduction band,  $E_T$  is the level of G-R centers,  $k$  is Boltzmann's constant,  $T$  is the temperature,  $\gamma_n$  is the electron density-of-states effective mass, and  $\sigma_n$  is the carrier capture cross section.

The G-R centers usually lie deep in the band gap and are known as deep energy level impurities. They act, for example, as recombination centers when there are excess carriers in the reverse-biased space-charge region (scr) of p-n junctions. The time constant  $\tau_e$  increases with decreasing temperature, and a series of C-t curves are illustrated in Fig. 2-11 as a function of temperature. The capacitance decay waveform is corrupted by noise, and the essence of DLTS is the extraction of the desired signal from that covered with the noise in some automated manner. A coincidence technique is also used, which is a signal processing method where the input signal is multiplied by a reference signal and a weighting function  $w(t)$ , and the product is filtered (averaged) by a weighting function. The filter can be an integrator or a low-pass filter. The correlator output is:

$$\delta C = (1/T) \int_0^T f(t)w(t) dt , \quad (2-18)$$

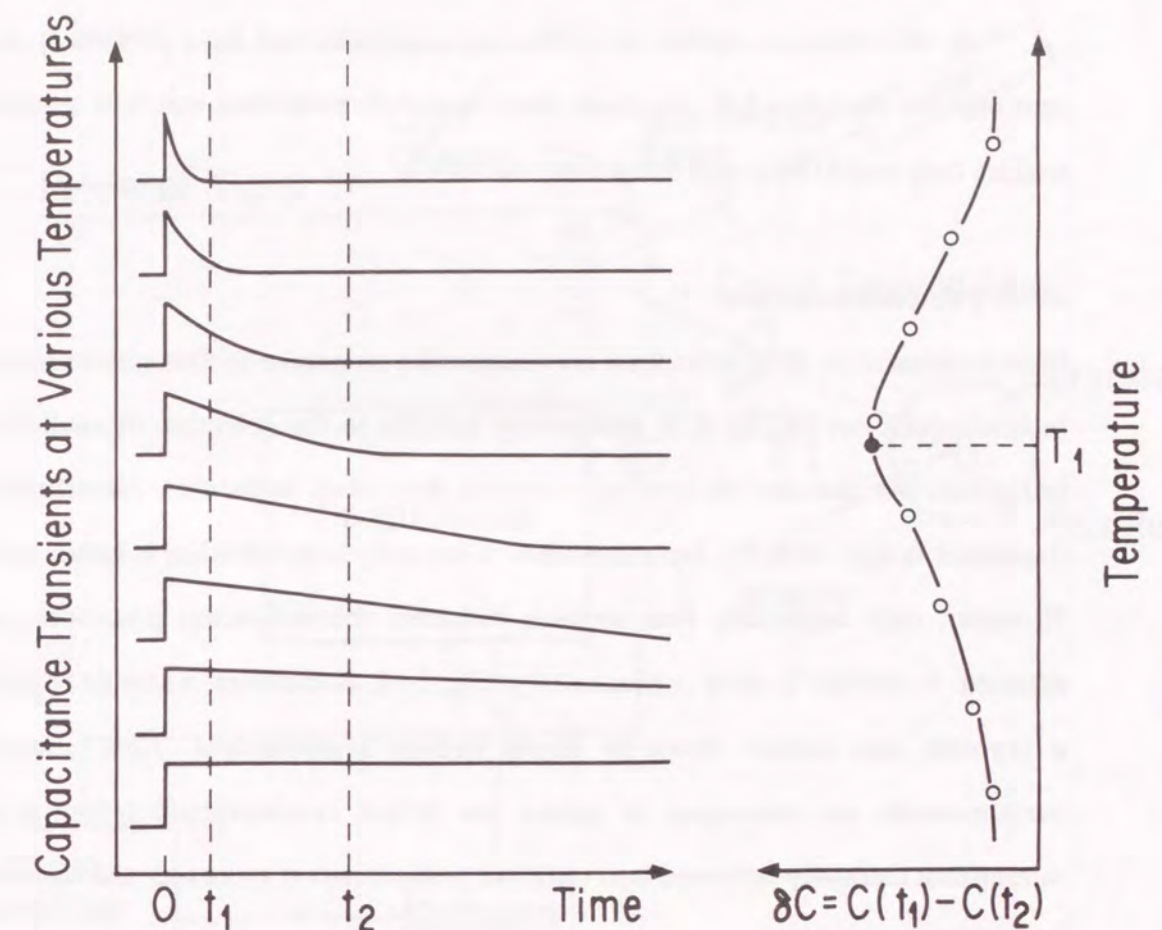


Fig. 2-11 Implementation of a rate window by a double boxcar integrator. The output is the average difference between the capacitance amplitudes at sampling times  $t_1$  and  $t_2$ .



where we use equation 2-16 for  $f(t)$ . By measuring  $\delta C$  and  $T$  for the different rate windows (weighting function), one can obtain the G-R level together with the capture cross section.

In this series of studies, the following conditions had been previously settled: zero bias (set bias) was 1 V,  $-V_1$  (peak bias) was -1 V, pulse time was 0.01 s, minimum waiting time was 0.004 s, and delay time was 0.01 s.

#### 2-5-4. Photoluminescence

Photoluminescence (PL) provides a non-destructive technique to find certain impurities in semiconductors [8,28]. It is particularly suitable to the detection of shallow-level impurities, but can also be applied to certain deep-level impurities. Identification of impurities is easy with PL, but estimation of impurity concentration is rather difficult. However, only impurities that produce radiative recombination processes can be detected. A typical PL setup is illustrated in Fig. 2-12. Sometimes, a sample is placed in a cryostat and cooled down to liquid helium temperatures. Low-temperature measurements are necessary to obtain the fullest spectroscopic information by minimizing thermally-activated non-radiative recombination processes and thermal line broadening.

The sample is excited by an optical source, typically a laser with  $h\nu > E_g$ , to generate electron-hole pairs that are recombined by one of several mechanisms. Photons are emitted in a radiative recombination processes. In non-radiative recombination mechanism, no photons are emitted any more. The photon energy depends on the recombination processes illustrated in Fig. 2-13, where five of the most commonly observed PL transitions are shown. Band-to-band recombination (Fig. 2-13 a) dominates at room temperature, but is rarely observed at low temperatures in materials with small effective masses due to the large electron orbital radii. Excitonic recombination is commonly observed at low temperatures. A free exciton (FE) decay energy, shown in Fig. 2-13 b, is slightly less than the band-gap energy required to create separated electron-hole pairs. This is because coulombic attraction can lead to the formation of an

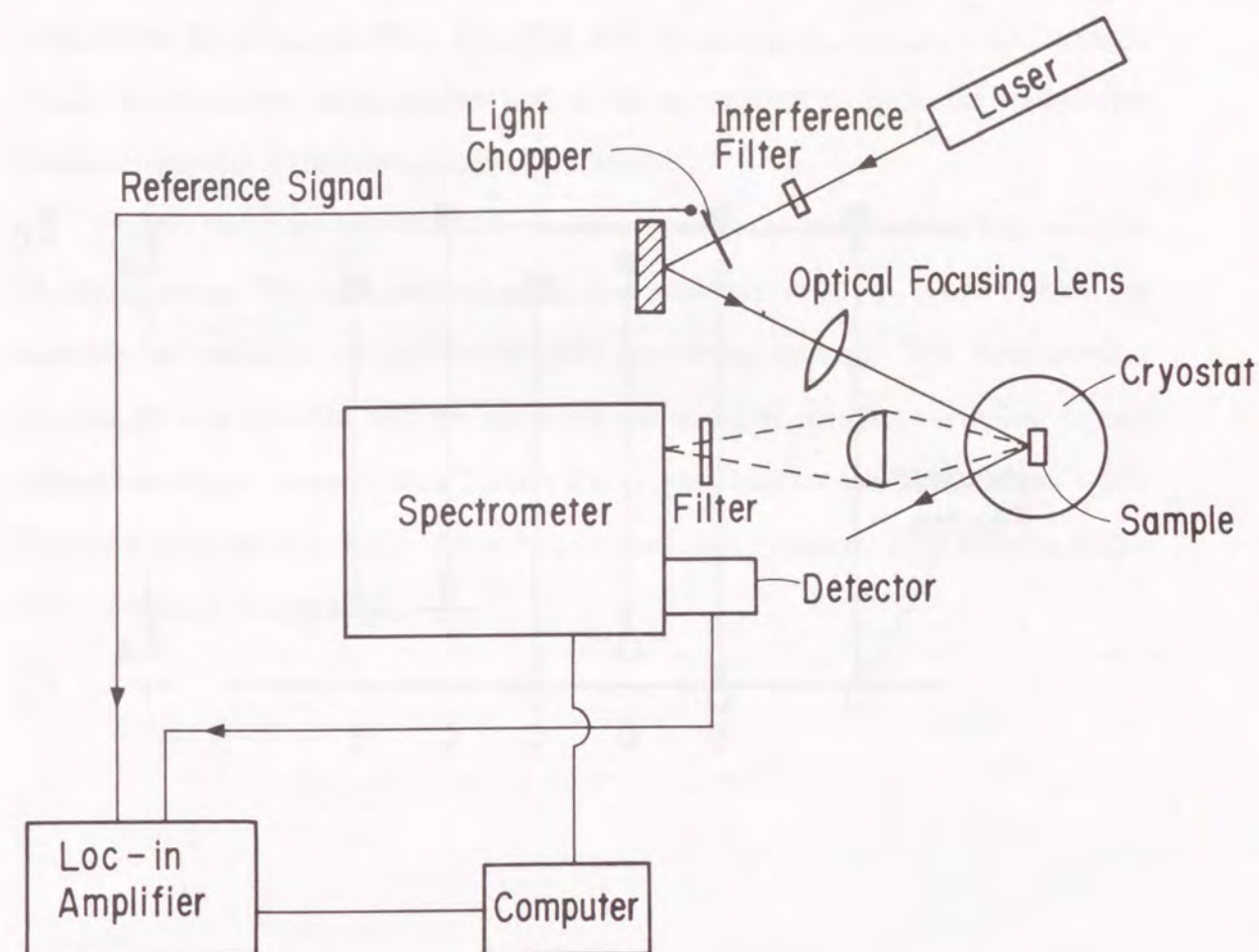


Fig. 2-12 Apparatus for photoluminescence (PL) measurements.



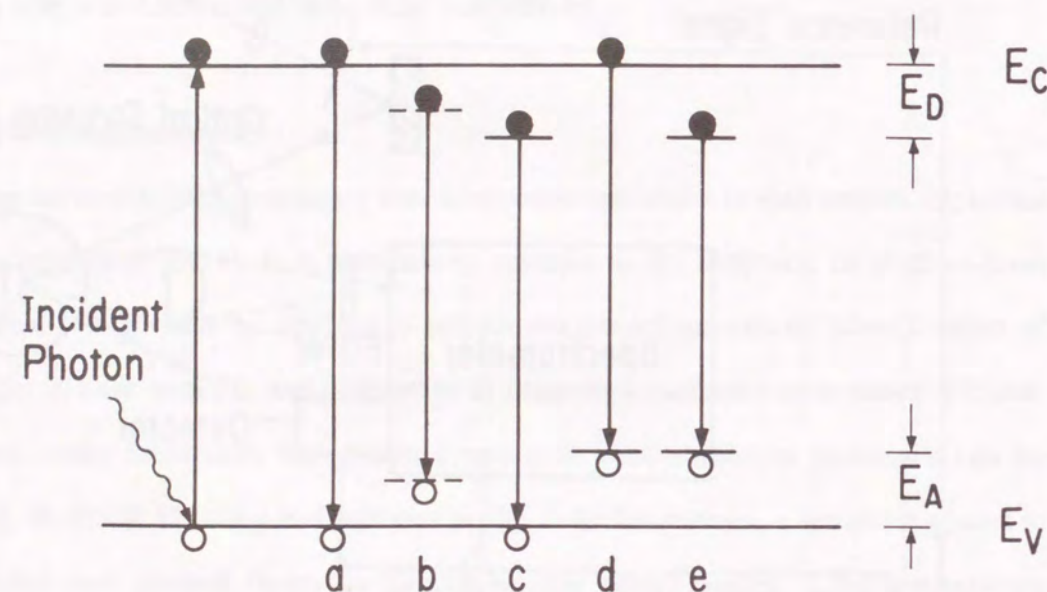


Fig. 2-13 Radiative transitions observed with PL.

excited state in which an electron and a hole remain bound one another in a hydrogen-like state. A free hole can combine with a neutral donor (Fig. 2-13 c) and forms a positively charged excitonic ion or a bound exciton (BE). Similarly, electrons combining with neutral acceptors also form BEs (Fig. 2-13 d). Lastly, an electron which escaped from a neutral donor can recombine with a hole in a neutral acceptor: the well-known donor-acceptor (D-A) recombination (Fig. 2-13 e).

In this study, a 400 mW 514.5 nm Ar laser and a Ge detector have been used for PL measurement. The input and output slit was relatively wide, i.e., 3 mm because the intensity of radiative recombination was not strong enough. The measurement wavelength was between 800 nm and 1200 nm at 4.2 K for GaAs samples. Square shaped samples, of approximately 5 mm x 5 mm, were used for this measurement which had been cut from each wafer and etched in a solution contained  $\text{H}_2\text{SO}_4:\text{H}_2\text{O}_2:\text{H}_2\text{O} = 10:1:1$  for about 20 min at RT.



### 3. SOLID-LIQUID INTERFACE SHAPE AND CHARACTERISTIC STRUCTURAL DEFECTS

#### 3-1. INTRODUCTION

One of the most important problems is to control the crystal structure and the nature of defects during the crystal growth from a melt. Dislocations in a substrate material seriously affect the nature of the epitaxial layer grown on it. A number of papers [3,29-31] have already discussed the relations among thermal stress induced while the crystal is being cooled, the shape of solid-liquid interface during the crystal growth and the defect density.

The crystals grown by the boat growth method have been used as substrates for LEDs because of their low dislocation density and their uniform distribution. However, the defect rich regions are sometime introduced in crystals and affect the uniformity of the material. These regions are not appropriate for practical use. It has also been reported that controlling the shape of solid-liquid interface is important to avoid the introduction of such defects [32]. The causal relationship between the shape and the nature of defects is still obscure.

In this chapter, defects were observed by using the etching technique as the simplest and most reliable way to find out them. The shape of solid-liquid interface was also observed from the striations revealed after etching the specimens in particular kind of chemical solution. Defect characterization was carried out by TEM. The nature of defects and their distribution will be discussed together with the simulation of the distribution of internal stress in solid phase.

#### 3-2. EXPERIMENTS

GaAs single crystals used in this chapter were grown by the GF method [33] as described in section 1-2-2. Figure 3-1 schematically shows the configuration in the growth system. For the purpose of later discussion, the Z axis is assigned along the

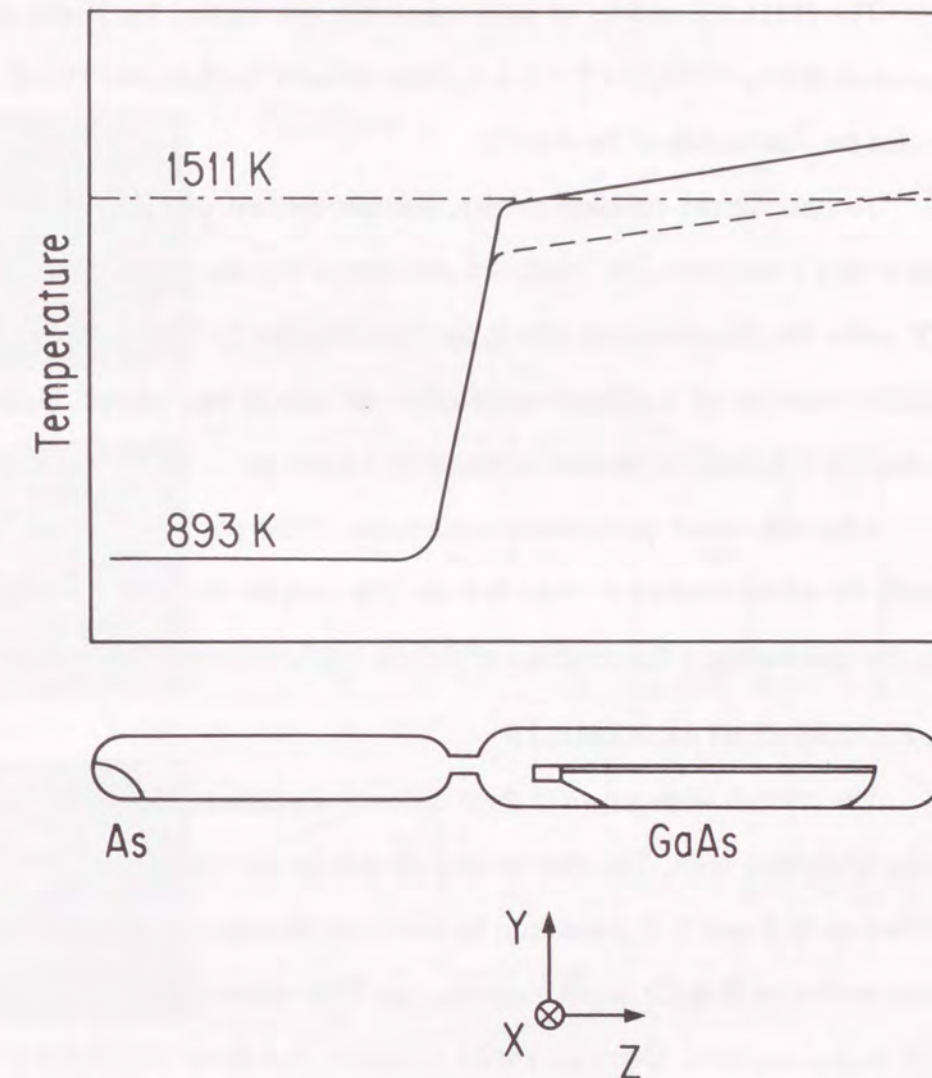


Fig. 3-1 The schematic diagram of the gradient freeze method. We fixed the X, Y and Z directions as illustrated.



growth direction, the X axis along the width of the boat and the Y axis perpendicular to them as shown in Fig. 3-1.

The (111) As surface of each specimen was etched for 3 min at 25 °C in a solution of  $\text{HNO}_3:\text{HF}:\text{H}_2\text{O} = 3:1:4 + \text{AgNO}_3$  0.3 wt% (etching test 1) [14]. This etchant revealed the distribution of the defects.

To observe the striation pattern, another etchant which contains  $\text{H}_2\text{SO}_4:\text{H}_2\text{O}_2:\text{H}_2\text{O} = 10:1:1$  was used. The specimen was dipped into the solution for about 25 min at 10 °C under the illumination of strong light (etching test 2) [21]. Etched specimens were carefully observed by a differential interference optical microscope. Figure 3-2 shows the shape of solid-liquid interface as traced by a digitizer.

After the above preliminary experiment, TEM observation was carried out to identify the microstructure of these defects. The samples for TEM observation were cut from the regions where the existence of defects had been checked by etching test 1.

### 3-3. EXPERIMENTAL RESULTS

The crystals were grown in three different conditions. Figure 3-3 summarizes the results of etching tests. The distribution of defects and the shape of the solid-liquid interface on X-Y and Y-Z planes can be classified into three groups. Etching tests 1 and 2 were applied to Si or Cr doped materials, but TEM observation was carried out mainly in Cr doped crystals. One can easily visualize the three dimensional temperature distribution in solid phase in individual cases A, B or C [34,35]. The detailed defect structures of following discussions is described in section 1-2-4.

#### Case A

Judging from the results obtained by TEM observation, the principal defects that cause the etching patterns are groups of rows of edge type 60° dislocations; One can simply identify the defects of this type to be typical small angle grain boundaries on the (110) plane (see Fig. 3-4 (a)). Figure 3-3 shows that this type of defect usually appears in every part other than the central part along X axis. In this case, the solid-liquid interface has a small radius of curvature. In this region, it also has been found another type of two

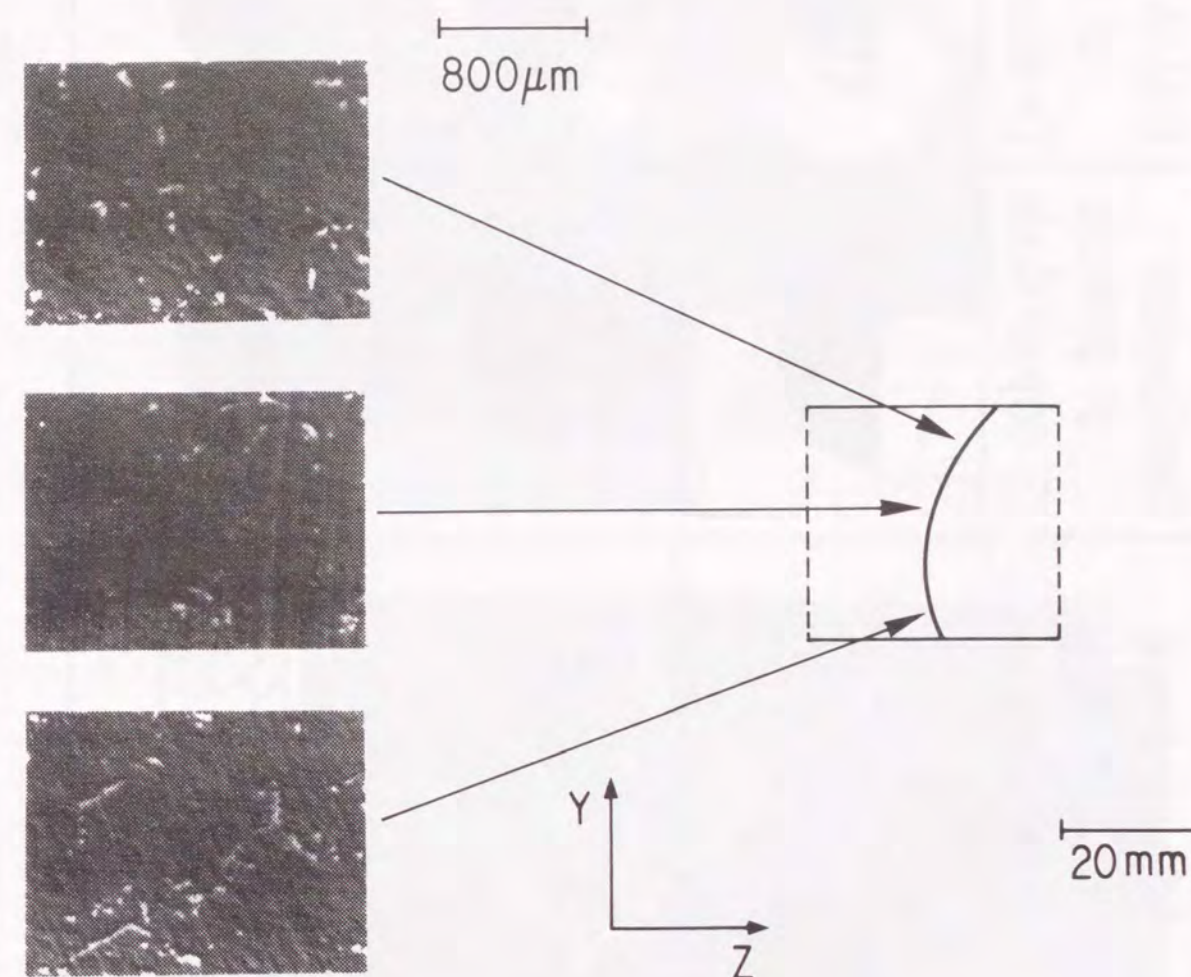

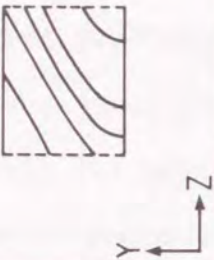


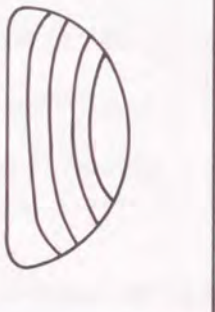
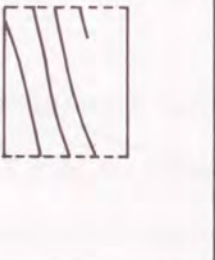



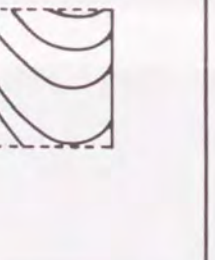




Fig. 3-2 The trace of the shape of solid-liquid interface by using a differential interference optical microscope. Each specimen was etched by etching solution 2.



Case	Solid-liquid interface X-Y plane	Solid-liquid interface Y-Z plane	Distribution of defects Si doped GaAs	Distribution of defects Cr doped GaAs
A				
B				
C				

20mm

Fig. 3-3 The striation of X-Y and Y-Z planes together with the distribution of defects. These patterns were observed defect structure of Si doped GaAs.

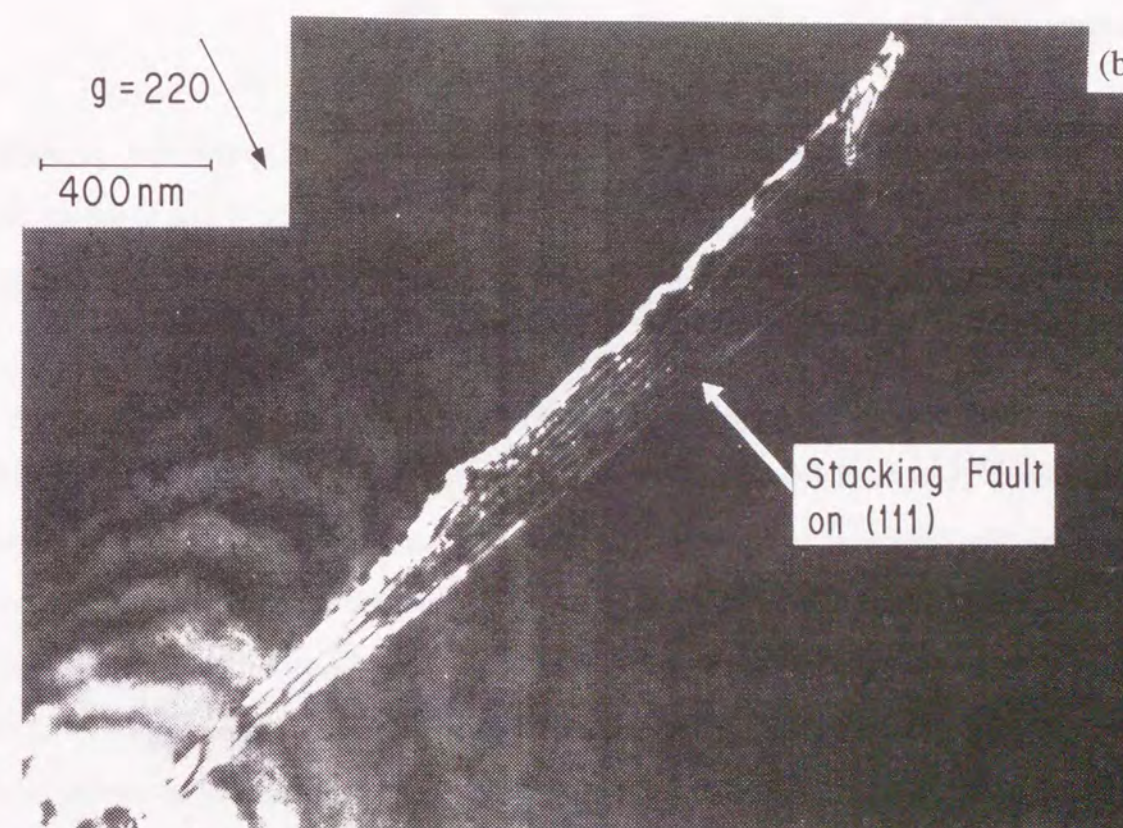
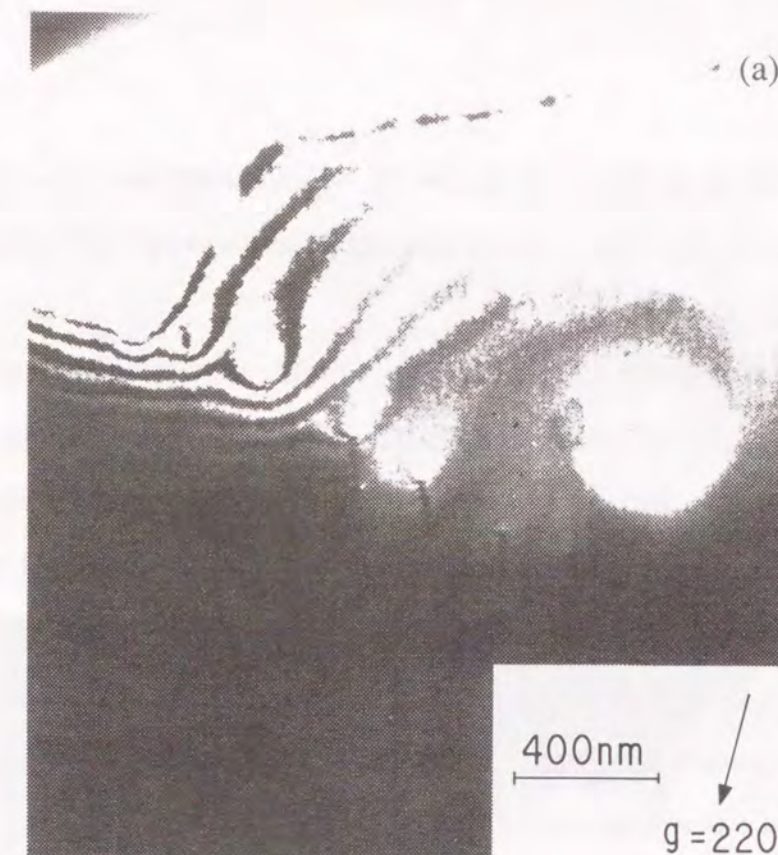


Fig. 3-4

Defects observed in case A.

(a) A row of edge dislocations on the (110) plane.

(b) Stacking fault on the (111) plane with some precipitates on.





dimensional defects as shown in Fig. 3-4 (b), which has the form of a stacking fault on the (111) plane. On this plane, one can also recognize the images of small precipitates.

#### Case B

The etching pattern in case B in Fig. 3-3 reflects the presence of complex defects as shown in Fig. 3-5. The shape of solid-liquid interface is relatively smooth compared with that of case A. Etching treatment 1 caused only one simple straight line. After detailed observation, a stacking fault on the (111) plane was found surrounded by complex structures including entangled dislocations and dislocation loops. The origin of the etching pattern B is tentatively imagined as follows: A crack started at the solidification front is introduced during the growth process of the crystal. Next, both fresh surfaces contact each other giving a small amount of misfit. So much strain accumulates around the stacking fault or boundary around which groups of complicated defects were also formed.

#### Case C

Here, solidification must have started at the bottom end of the melt, in other words, there was a region of negative temperature gradient along the Y axis in the region close to the bottom. With this negative temperature gradient, a convection current, which usually helps the melt mixing, must never have occurred.

Two types of string shaped precipitates have been found as shown in Fig. 3-6 (a). One labeled A, is not a dislocation and does not present any dislocation like strain field contrast. No particular impurity atoms have been detected by using an analytical microscope. The type B defect must also be a kind of precipitate, but this part must have been etched off while the specimen was being etched. The following understanding has been supposed: Constituent atoms of both types, Ga and As atoms, precipitated independently around dislocations with different character, minimizing the strain field around the dislocations. Another example of the defects is shown in Fig. 3-6 (b); these were taken under conditions of a dark field image. Small triangles of precipitates in lines can be recognized; they are supposed to have been nucleated around the strain field of dislocations.

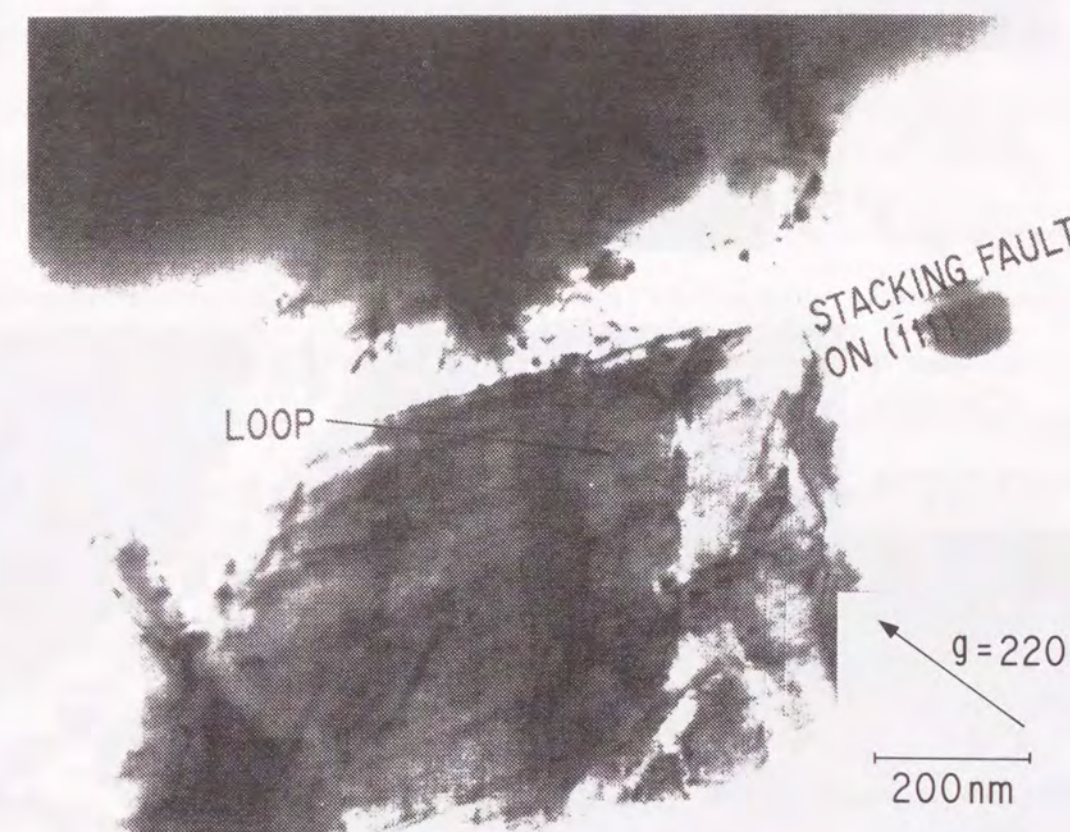


Fig. 3-5 Defects observed in case B.  
Stacking fault on the (111) plane and complex defects.



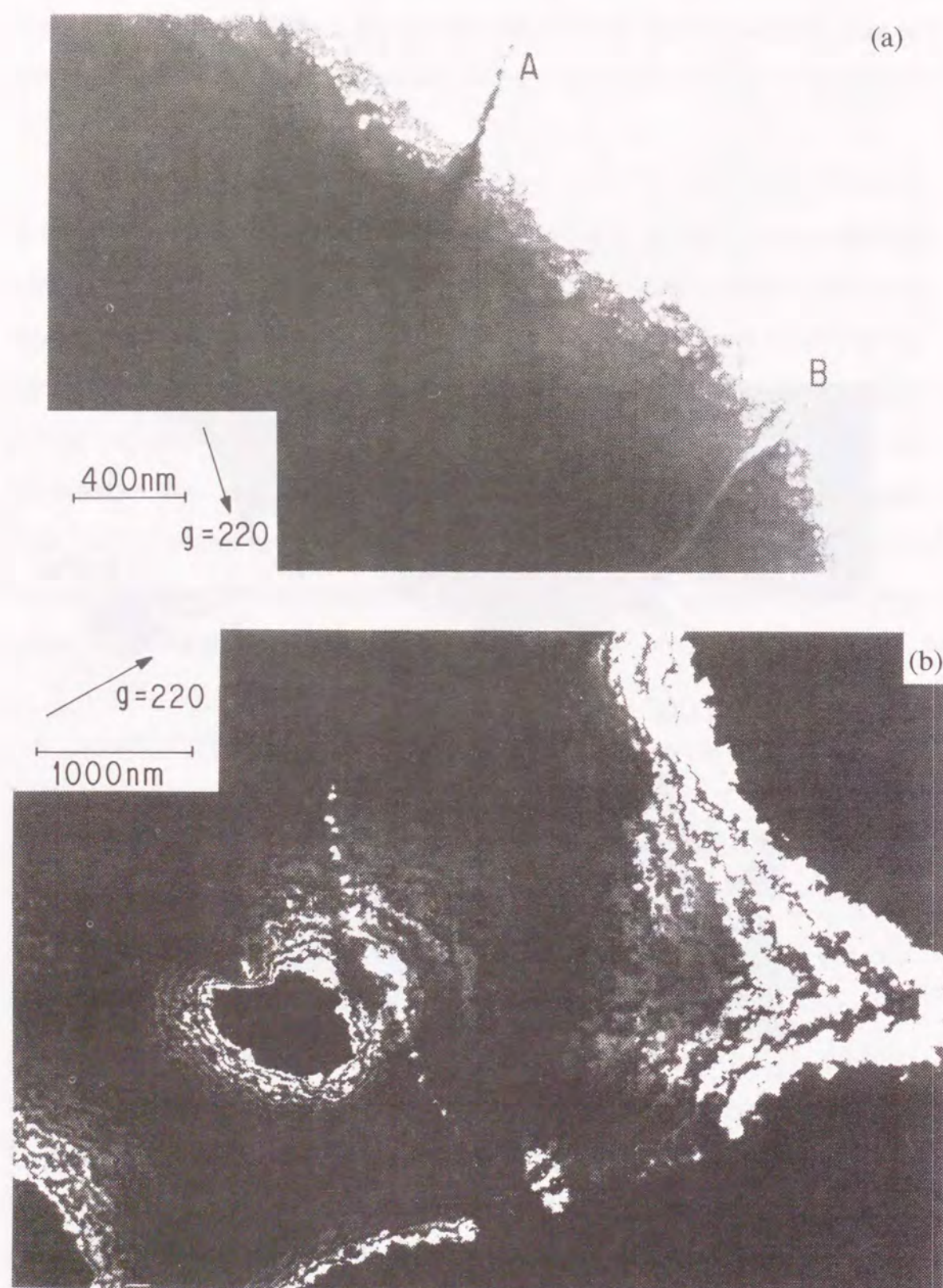


Fig. 3-6 Defects observed in case C.  
 (a) Two types of one dimensional precipitates.  
 (b) Dark field image around dislocations and precipitates.

### 3-4. DISCUSSIONS

As mentioned already, there is a close causal relationship among the distribution of defects, the shape of solid-liquid interface, and the nature of defects. Defects have been observed mainly in regions near the concave interface; the propagation direction of these defects is normal to the interface [36]. The former reporters have proposed that the generation of dislocations derives from the internal thermal stress [3,30,31]. However, for this GF method, the thermal stress is not large enough to introduce these defects by applying a very small amount of temperature gradient ( about  $1^{\circ}\text{C}/\text{cm}$  ) and cooling rate ( less than  $1^{\circ}\text{C}/\text{h}$  ).

Then, the amount of stress was estimated starting at the solid-liquid interface, taking the volume expansion by solidification into consideration. A numerical simulation was carried out by the finite element analysis [37]. The model was simplified as an isotropic two dimensional plane stress model. The force was applied on the solid-liquid interface, the shape of which was traced from that of striations as shown in Figs. 3-2 and 3-3. Free boundary condition was applied on the surface of crystal while the points crossing at the wall of the boat and the solid-liquid interface were fixed in this simulation. The simulation models are illustrated in Fig. 3-7. Figure 3-8 shows the distribution of principal stress estimated by this simulation. The value of the stress at each point in a solid is given in arbitrary units where positive and negative values mean compression and dilation, respectively.

According to the stress map in Fig. 3-8, the origin of the defects is able to be concluded the local concentration of stress, although detailed calculation including component of shear stress will be required.

### 3-5. CONCLUSION

Defect distribution and the shape of the solid-liquid interface in GaAs single crystals grown by the GF method were observed by etching. The nature of defects was



Case \	Simulation Model X-Y Plane	Simulation Model Y-Z Plane
A		
B		
C		

— Free  
 — Wall of the Boat (Free)  
 - - - A Certain Fource (f)  
 Per Unit Length / Free

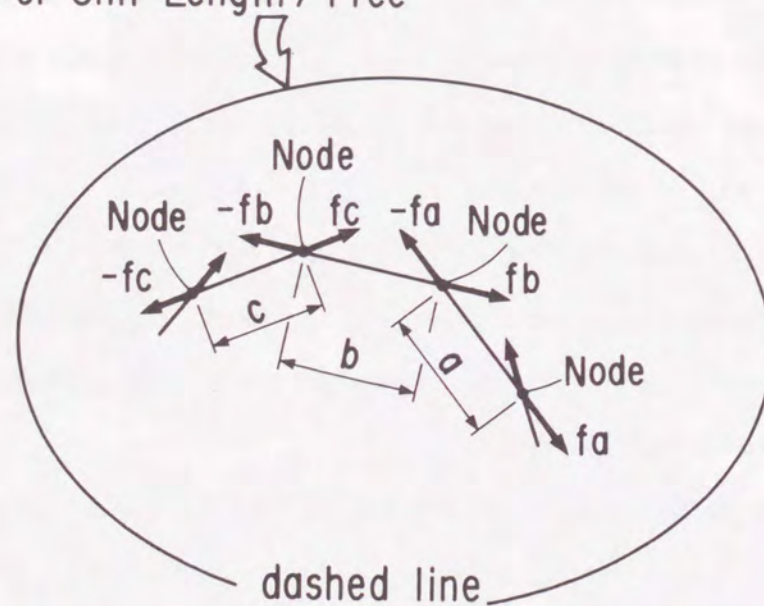


Fig. 3-7 Simulation stress model in solid phase. Solid line is free surface, bold line is the wall of the boat, and dashed line is solid-liquid interface, respectively. The cross points of the solid-liquid interface and the wall of the boat are fixed. The shape of solid-liquid interface was traced from that of striation in Fig. 3-3.

Case \	Stress distribution X - Y plane	Stress distribution Y - Z plane
A		
B		
C		

20 mm

Fig. 3-8 Simulated stress distribution in solid phase. The shape of solid-liquid interface was traced from that of striation in Fig. 3-3.



identified by TEM. There is a close relation among the distribution of defects, the shape of solid-liquid interface and the nature of defects. A numerical simulation of the initial stress caused by solidification-induced volume expansion and the stress started at the interface was carried out. The obtained defect distribution corresponds well with that of observed defects.

## **4. THE ROLE OF DIFFUSION BARRIER TEMPERATURE IN CRYSTAL GROWTH**

### **4-1. INTRODUCTION**

GaAs crystals grown by the boat growth method [4] (HB Method/GF Method) are commonly used as materials for LEDs and LDs, as mentioned before. However, such GaAs crystals are contaminated with Si from the quartz used in the boat growth method [38-41]. The Si atoms come not only from the quartz boat but from the quartz ampoule [39-41]. GaAs crystals are probably also contaminated with oxygen from quartz, but the effect of oxygen contamination in GaAs crystals has not yet been clarified.

The reaction of gallium with the quartz boat was described by Cochran and Foster [38], using equilibrium calculations. Kobayashi et al. [41] reported that Si contamination was enhanced by the presence of boron. They also reported that GaAs crystals grown in a pyrolytic boron nitride (pBN) boat were contaminated with Si and concluded that Ga vapor reacted with the quartz ampoule. Suzuki and Akai [42] and Akai et al. [43] clarified that Si contamination in GaAs crystals was mainly controlled by the temperature of the medium temperature zone in the three-temperature zone horizontal Bridgman (3T-HB) method. The medium temperature zone of the 3T-HB method is situated between the high temperature zone and low temperature zone. They reported that Si contamination could be prevented by setting a medium temperature zone so as to control the gallium suboxide ( $\text{Ga}_2\text{O}$ ) vapor pressure. The solubility of oxygen in GaAs crystals was discussed by Leitner and Moravec [44] using the above mentioned results.

Woods and Ainsle [45] reported the relationship between the partial pressure of additional oxygen in the ampoule and electronic properties in order to reduce Si contamination of GaAs crystals. They reported that oxygen added in the quartz ampoule in amounts varying from zero to 150 Torr at room temperature, suppresses the  $\text{SiO}_2$  dissociation at the wall of the quartz boat. The room temperature resistivity increased by about ten orders of magnitude. Martin et al. [46] reported that gettering of Si was



observed even in Si and Ga<sub>2</sub>O<sub>3</sub> co-doped GaAs crystals. They proposed a compensation scheme that takes account of the value of resistivity measured in undoped or slightly Cr doped boat-grown GaAs crystals. Gatos et al. [47] reported that oxygen in GaAs introduces a midgap level, ELO, which has almost same activation energy as EL2 and with four times larger electron capture cross section. However, they have not investigated oxygen concentration in GaAs crystals yet and its correlation with crystal growth conditions.

This chapter describes the origin and behavior of oxygen contamination in GaAs crystals in the GF growth process. Experimental results on the relationship between diffusion barrier temperature ( $T_d$ ) and oxygen concentration are compared with calculations of chemical equilibrium. The effect of oxygen concentration on the properties of GaAs crystals is also reported.

## 4-2. EXPERIMENTS

### 4-2-1. Crystal Growth

Undoped and intentionally Si-doped GaAs crystals were grown by the GF method [4,33], as schematically illustrated in Fig. 4-1. A diffusion barrier is a small hole sitting between a high temperature zone and a low temperature zone. It is well known that gaseous products are produced by the reaction of Ga with quartz [38]. Si contamination in GaAs crystals has been reduced by impeding the diffusion of the gaseous products to the low temperature zone [38] by placing a diffusion barrier at the end of the high temperature zone [48], which is the coldest point of the high temperature zone. The temperature of the diffusion barrier ( $T_d$ ) was measured by a thermocouple in contact with the quartz ampoule.

Crystals were grown under various  $T_d$  conditions in the range of 1280 - 1500 K. Here, 42.1 ppm Si by weight was added into GaAs melt for Si-doped GaAs crystal growth.

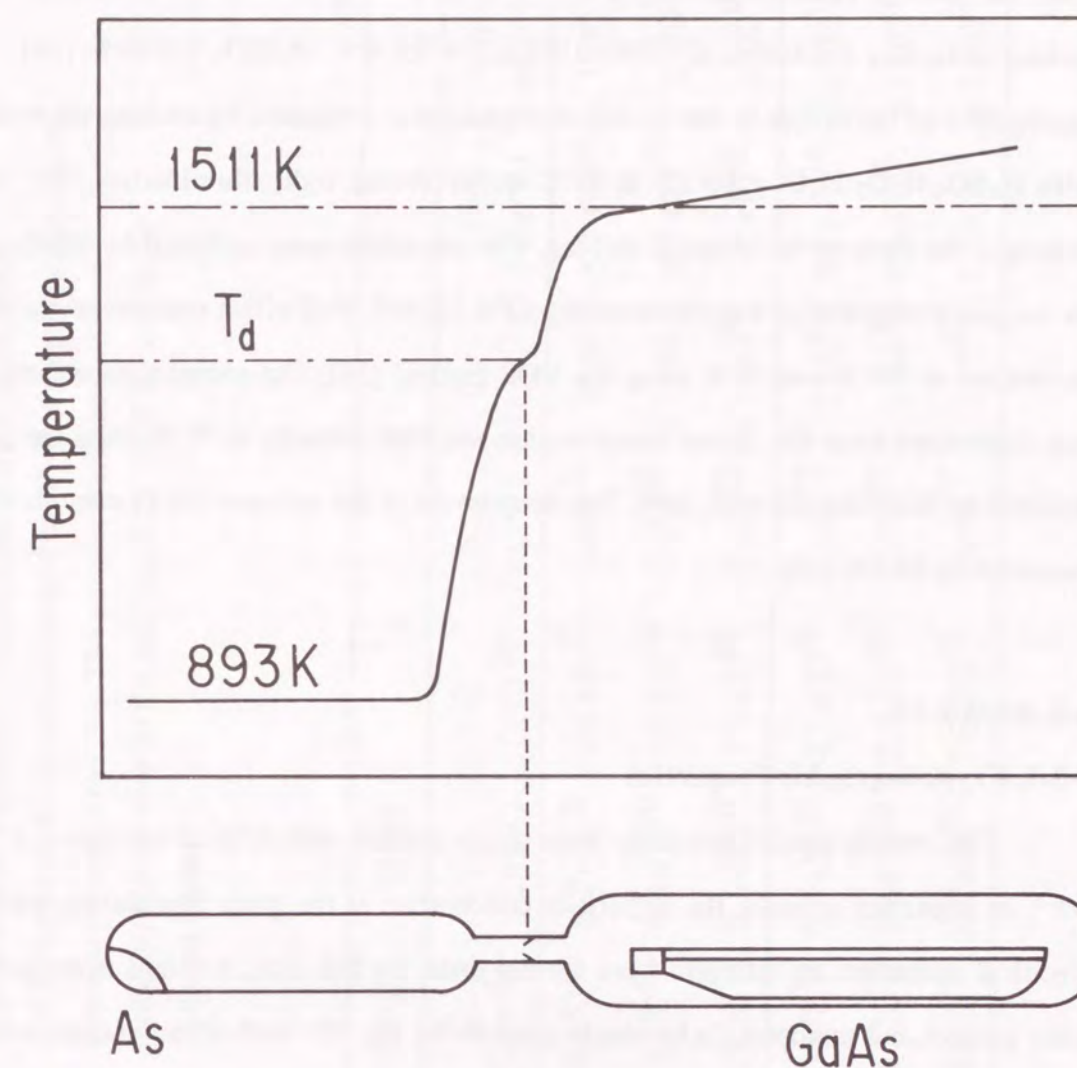


Fig. 4-1 Schematic diagram of the gradient freeze method.  $T_d$  is the temperature of the diffusion barrier.



#### 4-2-2. Crystal Evaluation

Similar to the former chapter, crystallographic evaluation was carried out by chemical etching. The etch pit density (EPD) of these samples was counted on (111) As surface etched by a solution of  $\text{HNO}_3:\text{HF}:\text{H}_2\text{O} = 3:1:4 + \text{AgNO}_3$  0.3 wt% [14]. The aggregation of impurities in the Si-doped crystals was evaluated by etching the wafers with  $\text{H}_2\text{SO}_4:\text{H}_2\text{O}_2:\text{H}_2\text{O} = 10:1:1$  at  $10^\circ\text{C}$  under strong light illumination [21]. This etching is the same as the striation etching. The impurities were analyzed by SIMS, and the oxygen concentration was measured by CPA [10,46]. Hall effect measurements were carried out at 300 K and 77 K using the VDP method [26]. The compensation ratio ( $\theta$ ) was determined from the carrier concentration and Hall mobility at 77 K using the table reported by Walukiewicz et al. [49]. The deep levels in the undoped GaAs crystals were measured by DLTS [27].

### 4-3. RESULTS

#### 4-3-1. Crystallographic Properties

The crystals used in this study were single crystals with EPD of less than  $1 \times 10^{-4} \text{ cm}^{-3}$ . In imperfect crystals, the impurities concentrate at the grain boundaries, and the electrical properties are different from normal ones. By this time, it seems to be hard to grow perfect and undoped GaAs single crystals by the GF method, so sample wafers were sliced from the part near the seed, where the fraction solidified ( $g$ ) is equal to 0.15.

#### 4-3-2. Impurity Analysis

Typical results of the impurity analysis for various  $T_d$  are shown in Table 4-1. The CPA measurements show that oxygen concentration depends on  $T_d$ . The SIMS measurements indicate that Si and Al are the dominant impurities. Si and Al come from the reaction of Ga with quartz or, in the case of Si in Si-doped GaAs, come from the Si dopant. Other impurities were detected at very low levels or some others were the same as the background level.

Table 4-1 Typical results of impurity concentration analysis in undoped and Si-doped GaAs crystals, measured by SIMS. Oxygen concentration was also measured by CPA. The samples were obtained from  $g = 0.15$ . Initial Si concentration in the melt was  $4.21 \times 10^{-5}$  by weight for Si-doped GaAs.

	$T_d$ (K)	CPA		SIMS						
		O ( $\text{cm}^{-3}$ )	O ( $\text{cm}^{-3}$ )	C ( $\text{cm}^{-3}$ )	Si ( $\text{cm}^{-3}$ )	Cu ( $\text{cm}^{-3}$ )	Fe ( $\text{cm}^{-3}$ )	Mn ( $\text{cm}^{-3}$ )	Al ( $\text{cm}^{-3}$ )	
undoped GaAs	1467.5	$4.9 \times 10^{18}$	$\leq 2 \times 10^{16}$	$\leq 4 \times 10^{15}$	$4 \times 10^{16}$	$3 \times 10^{16}$	$\leq 3 \times 10^{14}$	$\leq 1 \times 10^{14}$	$\leq 1 \times 10^{16}$	
	1361.5	$5 \times 10^{15}$	$\leq 4 \times 10^{16}$	$\leq 1 \times 10^{16}$	$3 \times 10^{16}$	$\leq 7 \times 10^{15}$	$\leq 2 \times 10^{14}$	$2 \times 10^{15}$	$\leq 1 \times 10^{15}$	
	1354.3	$1.7 \times 10^{16}$	$\leq 4 \times 10^{16}$	$\leq 1 \times 10^{16}$	$3 \times 10^{16}$	$\leq 1 \times 10^{16}$	$1 \times 10^{16}$	$3 \times 10^{15}$	$\leq 7 \times 10^{14}$	
Si-doped GaAs	1477.0	$2.3 \times 10^{19}$	$\leq 4 \times 10^{16}$	$\leq 1 \times 10^{16}$	$7 \times 10^{17}$	$3 \times 10^{16}$	$\leq 3 \times 10^{14}$	$\leq 2 \times 10^{14}$	$\leq 8 \times 10^{15}$	
	1362.9	$8 \times 10^{15}$	$\leq 4 \times 10^{16}$	$\leq 3 \times 10^{16}$	$7 \times 10^{17}$	$3 \times 10^{16}$	$\leq 4 \times 10^{15}$	$\leq 1 \times 10^{14}$	$\leq 5 \times 10^{15}$	
	1309.7	$1.6 \times 10^{16}$	$\leq 2 \times 10^{16}$	$\leq 6 \times 10^{15}$	$7 \times 10^{17}$	$2 \times 10^{15}$	$\leq 1 \times 10^{14}$	$\leq 1 \times 10^{14}$	$\leq 2 \times 10^{14}$	



The differences in oxygen concentrations estimated by SIMS and CPA must have resulted from the inherent differences in the two techniques. SIMS uses secondary ions for analysis. The emission efficiency of secondary ions from oxygen compounds in GaAs crystals would not be large enough. Therefore, it has been concluded that SIMS is not a suitable for quantitative oxygen concentration analysis. On the other hand, CPA uses nuclear reactions for technique, so it detects all of the oxygen atoms present in the materials, regardless of each charge state.

Figure 4-2 shows oxygen concentration measured by CPA versus  $T_d$ . One must noted that oxygen concentration abruptly increases around  $T_d$  of 1400 K.

#### 4-3-3. Electronic Properties

All samples were n-type because of the presence of Si. The relationship between oxygen concentration and carrier concentration at 300 K in GaAs crystals is shown in Figs. 4-3 and 4-4 for undoped and Si-doped GaAs crystals, respectively. The carrier concentration of undoped crystals increased slightly with increasing the oxygen concentration. In Si-doped GaAs crystals, there was no correlation with oxygen concentration.

#### 4-4. DISCUSSION

##### 4-4-1. Reaction Between GaAs Melt and Quartz Boat

##### 4-4-1-a. Review of Previous Studies

Cochran and Foster [38,50] were the first to propose equilibrium calculations for a GaAs melt in a quartz ampoule and a boat. They assumed that  $Ga_2O$  exists only in the vapor phase, because there was no analytical data for oxygen concentration in GaAs crystals at that time. Their calculations were studied in detail by Woods and Ainsle [45] and Akai et al. [43]. Kobayashi et al. [41] proposed the reaction between Ga vapor and the quartz ampoule. They [41,43,45] also assumed that oxygen exists only in the vapor phase. A thermodynamic analysis [44] of oxygen concentration in GaAs crystals

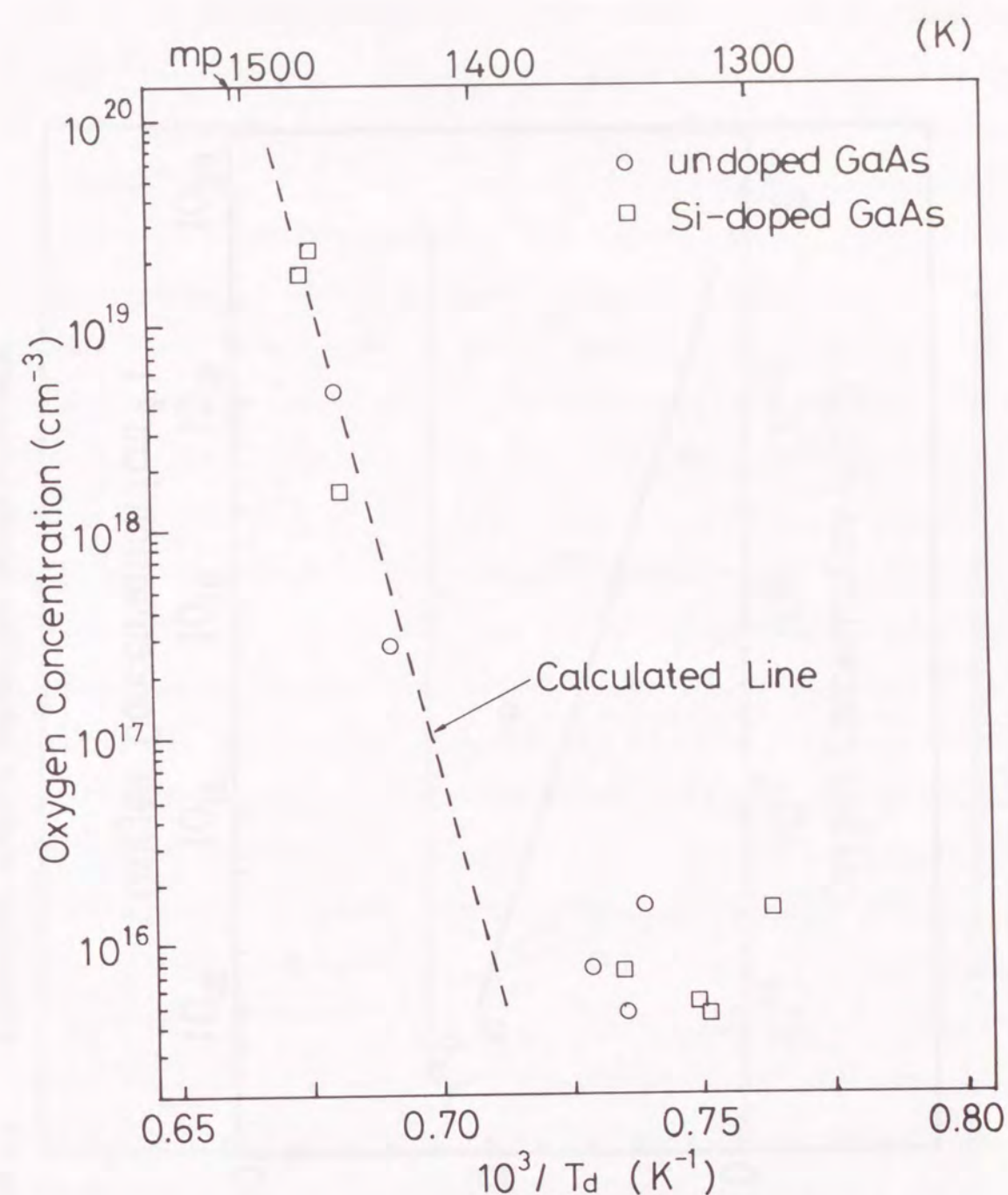


Fig. 4-2 Oxygen concentration in GaAs crystals by CPA versus the reciprocal of the diffusion barrier temperature  $T_d$ .



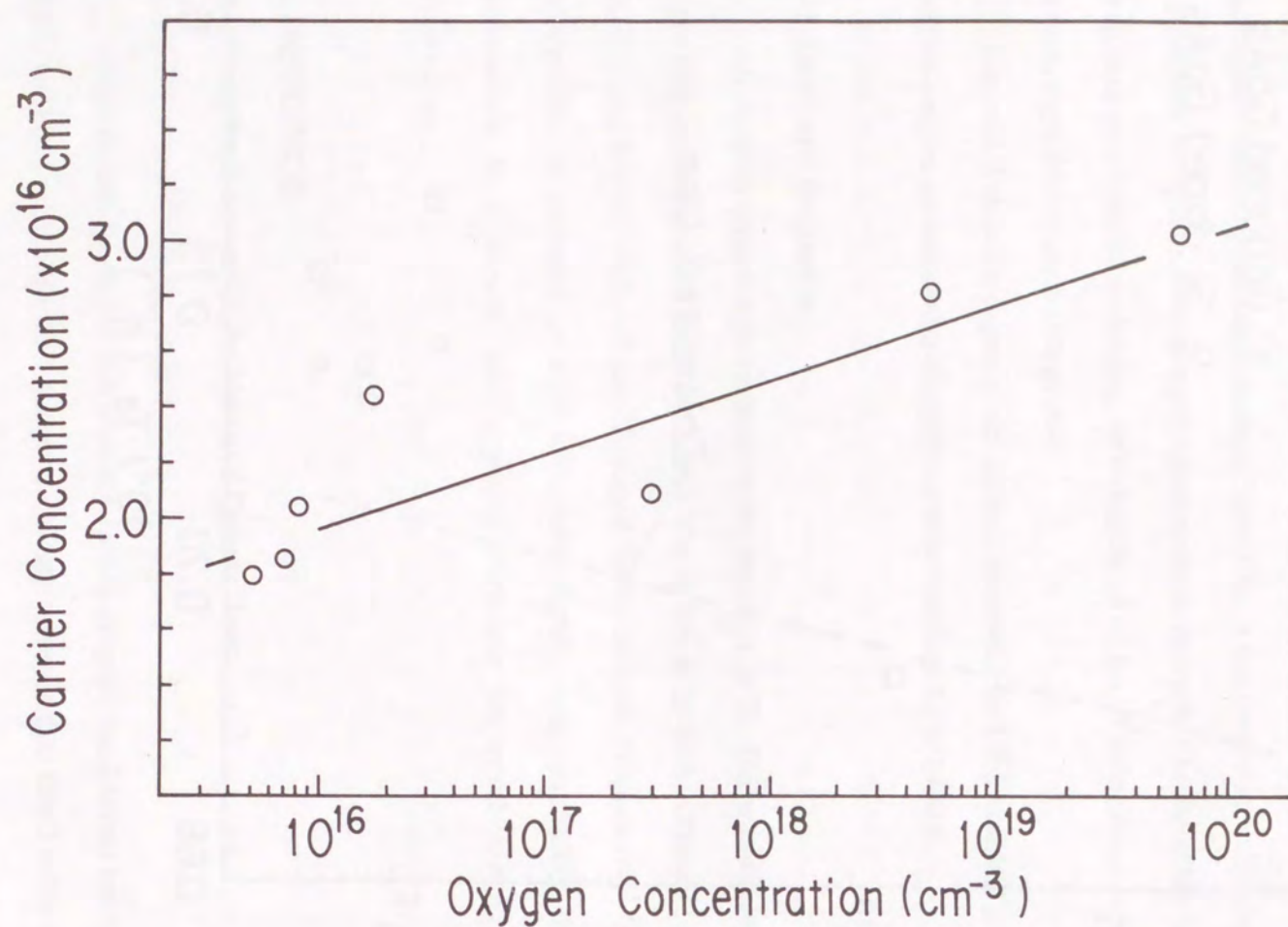


Fig. 4-3 Oxygen concentration in undoped GaAs crystals versus carrier concentration at 300 K.

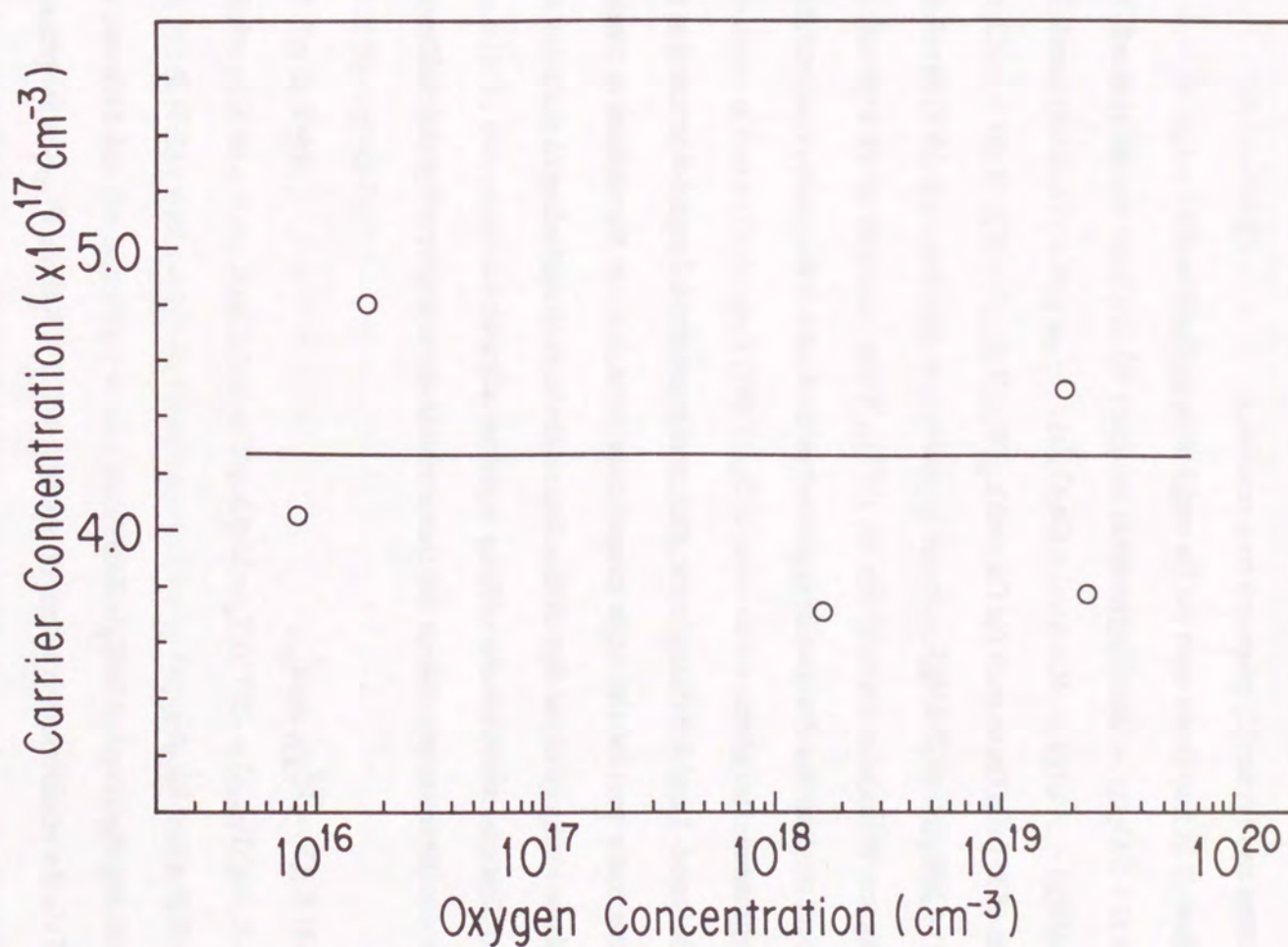


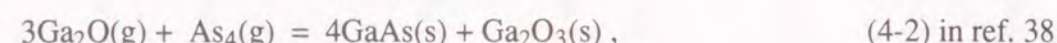
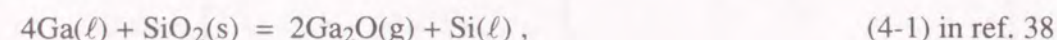
Fig. 4-4 Oxygen concentration in Si-doped GaAs crystals versus carrier concentration at 300 K. The initial Si concentration in GaAs melt was  $4.21 \times 10^{-5} \text{ cm}^{-3}$  by weight ratio.



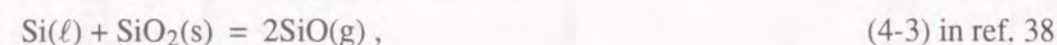
suggested to divide the reactions proposed by Cochran and Foster [38] into more fundamental reactions. Therefore, these reactions are reconsidered in detail using equilibrium calculations.

Cochran and Foster [2] proposed four reactions:

(1) Dissolution of Si into GaAs melt (or Ga melt) from a quartz boat



(2) Removal of Si from GaAs melt (or Ga melt)



where suffix ( $\ell$ ) means that the species is present in the GaAs or Ga melt, (s) means solid phase, and (g) means gas phase.

Reactions 4-1 and 4-3 occur in the melt, and reactions 4-2 and 4-4 proceed at the lowest temperature part of the high temperature zone, i.e., at the diffusion barrier. Basically, these reactions show that Si dissolves into the melt according to reactions 4-1 and 4-2, and Si is removed from the melt by reactions 4-3 and 4-4.

The equilibrium conditions of these reactions are given by the following equations:

$$\text{Reaction 4-1: } K_1(T) = P_{\text{Ga}_2\text{O}}^2 a_{\text{Si}}/a_{\text{Ga}}^4, \quad (4-5) \text{ in ref. 38}$$

$$\text{Reaction 4-2: } \log(P_{\text{Ga}_2\text{O}}) = -20710/T_g + 12.82, \quad (4-6) \text{ in ref. 39}$$

$$\text{Reaction 4-3: } K_3(T) = P_{\text{SiO}}^2/a_{\text{Si}}, \quad (4-7) \text{ in ref. 38}$$

$$\text{Reaction 4-4: } \log(P_{\text{SiO}}) = -16950/T_g + 7.639, \quad (4-8) \text{ in ref. 38}$$

where  $K_1(T)$  is the equilibrium constant of reaction 4-1 at T Kelvin,  $P_{\text{Ga}_2\text{O}}$  is the pressure of  $\text{Ga}_2\text{O}$  gas in the ampoule,  $a_{\text{Si}}$  is the activity of Si in the melt,  $a_{\text{Ga}}$  is the activity of Ga in GaAs melt (or the activity of Ga melt),  $T_g$  is the gas temperature in the high temperature zone,  $K_3(T)$  is the equilibrium constant of reaction 4-3 at T Kelvin, and  $P_{\text{SiO}}$  is the pressure of SiO gas. In this system,  $T_g$  means  $T_d$  because the solid phase in reactions 4-2 and 4-4 occurs at the diffusion barrier, i.e., the coldest part of the high temperature zone.

Ga could also react with the quartz ampoule to produce gaseous products that could diffuse back into the boat and be a origin of contamination. The reactions between Ga vapor and the quartz ampoule are shown by the following equations [41]:



The equilibrium constants for reactions 4-9 and 4-10 are:

$$\text{Reaction 4-9: } K_9(T) = P_{\text{Ga}}/a_{\text{Ga}}, \quad (4-11) \text{ in ref. 41}$$

$$\text{Reaction 4-10: } K_{10}(T) = P_{\text{Ga}_2\text{O}} P_{\text{SiO}}/P_{\text{Ga}}^2, \quad (4-12) \text{ in ref. 41}$$

where  $K_9(T)$  is the equilibrium constant of reaction 4-9 at T Kelvin,  $P_{\text{Ga}}$  is the pressure of Ga vapor in the ampoule, and  $K_{10}(T)$  is the equilibrium constant of reaction 4-10 at T Kelvin. In an atmosphere of arsenic vapor, the equilibrium Ga activity in the gas phase is the same as that in GaAs melt [38].  $\text{Ga}_2\text{O}$  is more easily produced by reaction of the melt in contact with the quartz boat. Ultimately, the equilibrium will be on the common condition whether the reaction is with the boat or with the walls.

Two relationships are introduced to explain the impurity concentration in GaAs crystals in this study: one for the activity, and the other for the segregation. It is well established that the relationship between activity  $a_I$  and impurity concentration in the melt  $N_I$  is given by:

$$a_I = \gamma_I N_I, \quad (4-13)$$

where  $\gamma_I$  is the activity coefficient of the impurity.

It is also well established that the relationship between the impurity concentration in the solid and the impurity concentration in the liquid is represented by the following equation:

$$n_I = k_I N_I, \quad (4-14)$$

where  $k_I$  is the segregation coefficient of the impurity.

The results of previous studies combined with equations 4-13 and 4-14 are summarized in Fig. 4-5, which shows the activity of Si in GaAs melt, Si concentration in the GaAs liquid, and Si concentration in the GaAs solid. The pressure of gases at  $T_d$  is calculated from the equilibrium conditions of reactions 4-1, 4-2, 4-3, and 4-4. Here,  $a_{\text{Ga}}$



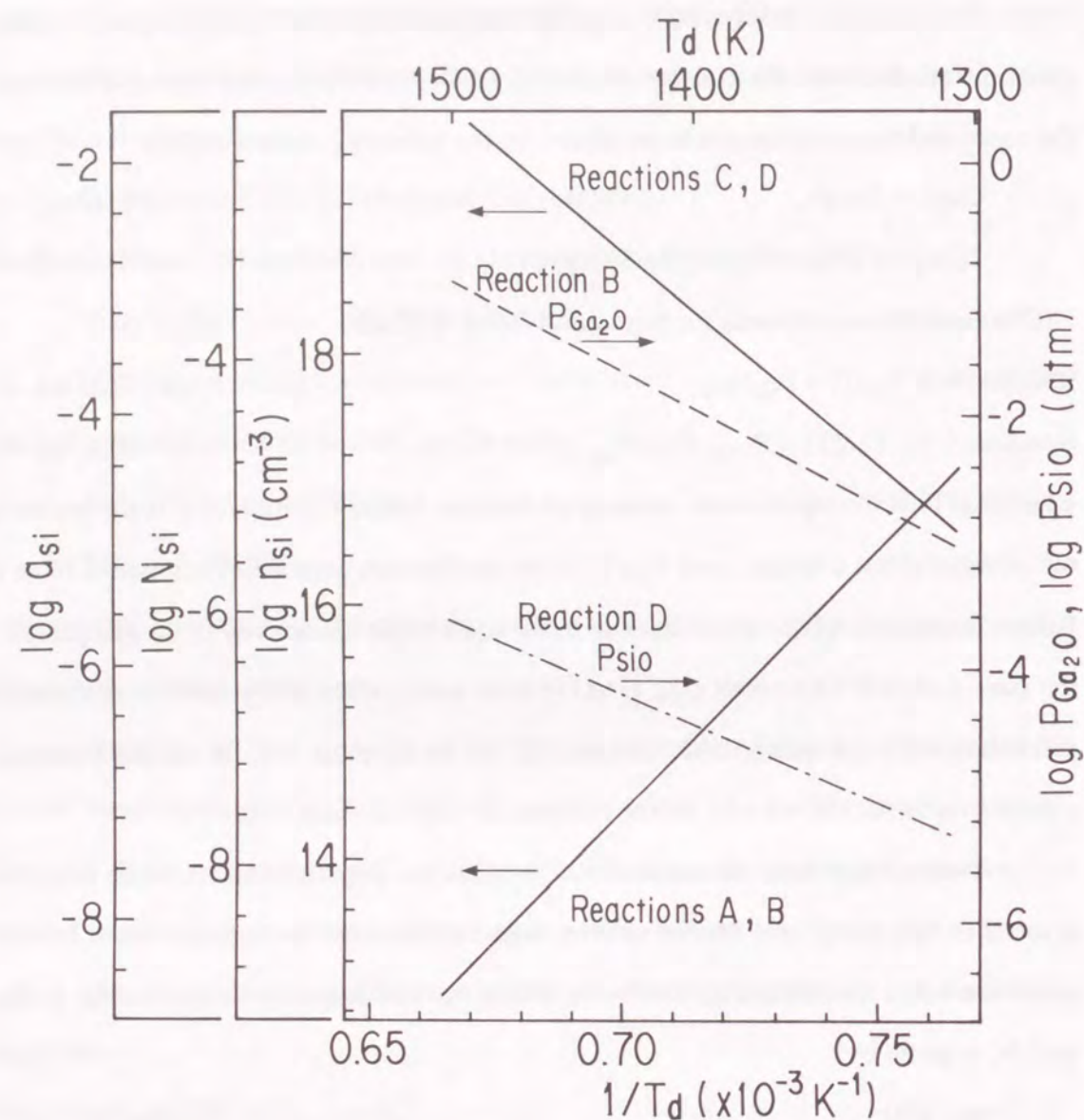


Fig. 4-5 Equilibrium relationships of reactions 4-1, 4-2, 4-3 and 4-4. The diffusion barrier temperature  $T_d$  determines the activity of Si in GaAs melt at 1511 K, Si concentration in GaAs melt at 1511 K (weight ratio), and Si concentration in GaAs crystals after solidification (atomic number).  $T_d$  also determines the pressure of gases in the ampoule.

was used for the Ga in GaAs melt. The temperature of GaAs melt was assumed to be the melting point of GaAs, 1511 K. Here,  $a_{Si}$ ,  $N_{Si}$  and  $n_{Si}$  mean the Si activity in GaAs melt, the Si concentration in GaAs melt by weight ratio, and the Si concentration in the GaAs solid by atomic number, respectively. The values of constants in used Fig. 4-5 were quoted by Akai et al. [43].

$$K_1(1511 \text{ K})' = K_1(1511 \text{ K})a_{Ga}^4 = 3.22 \times 10^{-11}$$

$$K_3(1511 \text{ K}) = 1.78 \times 10^{-6}$$

$$\gamma_{Si} = 2.62$$

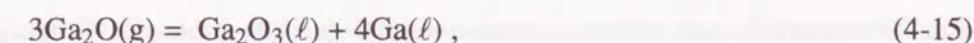
$$k_{Si} = 0.14$$

The following physical parameters were also used for the calculation: the density of the GaAs solid is 5.3 g/cm<sup>3</sup>, the average atomic weight of Ga and As is 70 g/mol, and Avogadro's number is  $6 \times 10^{23}$  atoms/cm<sup>3</sup>.

#### 4-4-1-b. Oxygen Contamination

There is some controversy over which reaction predominates in the problem of oxygen contamination. Akai et al. [43] and Leitner and Moravec [44] considered reaction 4-1 to be the predominant reaction, and derived theoretical relationships between  $N_{Si}$  and the oxygen concentration in the melt ( $N_O$ ). However, our experiments showed that  $N_O$  did not depend on  $N_{Si}$ , as shown in Table 4-1. A clear relationship was found between oxygen concentration in GaAs crystals and  $T_d$ , independent of  $N_{Si}$  as shown in Fig. 4-2.

These results suggest that oxygen concentration in GaAs crystals depends on reaction 4-2, which determines the relationship between  $T_d$  and  $P_{Ga_2O}$ . However, this reaction does not relate with oxygen concentration in GaAs crystals. Therefore, we introduced a new reaction for oxygen concentration in GaAs crystals. It involves the formation of  $Ga_2O$  from the reaction of  $Ga_2O_3$  with Ga [51].



The equilibrium constant of this reaction  $K_{15}(T)$  is given by:

$$\text{Reaction 4-15: } K_{15}(T) = a_{Ga_2O_3}a_{Ga}^4 / P_{Ga_2O}^3, \quad (4-16)$$



where  $a_{\text{Ga}_2\text{O}_3}$  is the activity of the  $\text{Ga}_2\text{O}_3$  in the melt. For  $\text{Ga}_2\text{O}_3$  in GaAs, there are defined the activity coefficient to be  $\gamma_{\text{Ga}_2\text{O}_3}$ , the concentration in GaAs melt to be  $N_{\text{Ga}_2\text{O}_3}$ , the segregation coefficient to be  $k_{\text{Ga}_2\text{O}_3}$ , and the concentration in the GaAs solid to be  $n_{\text{Ga}_2\text{O}_3}$ . From eqs. 4-13 and 4-14, and one obtain:

$$a_{\text{Ga}_2\text{O}_3} = \gamma_{\text{Ga}_2\text{O}_3} N_{\text{Ga}_2\text{O}_3}, \quad (4-17)$$

$$n_{\text{Ga}_2\text{O}_3} = k_{\text{Ga}_2\text{O}_3} N_{\text{Ga}_2\text{O}_3}. \quad (4-18)$$

The relationship between  $n_{\text{Ga}_2\text{O}_3}$  and  $P_{\text{Ga}_2\text{O}}$  is obtained from the equations 4-16, 4-17 and 4-18. This can be expressed as:

$$n_{\text{Ga}_2\text{O}_3} = \frac{k_{\text{Ga}_2\text{O}_3} K_{15}(T)}{\gamma_{\text{Ga}_2\text{O}_3} a_{\text{Ga}}^4} P_{\text{Ga}_2\text{O}}^3. \quad (4-19)$$

The temperature of GaAs melt can be regarded as constant in our experimental conditions. Thus, equation 4-19 can be written as:

$$n_{\text{Ga}_2\text{O}_3} = C P_{\text{Ga}_2\text{O}}^3, \quad (4-20)$$

where  $C$  is an unknown constant.

This suggests that the oxygen concentration in GaAs crystals is proportional to the third power of the  $\text{Ga}_2\text{O}$  pressure. The relationship between  $T_d$  and oxygen concentration in GaAs crystals can be derived from equations 4-6 and 4-16. The value of  $T_d$  and the oxygen concentration enable us to determine the constant  $C$  in equation 4-20. The constant  $C$  was fitted by using the point of  $T_d$  to be equaled 1477 K, and oxygen concentration to be equaled  $2.3 \times 10^{19} \text{ cm}^{-3}$  from the data in Table 4-1. The calculated line closely fits our experimental data as shown in Fig. 4-2.

It can be concluded that the oxygen contamination in GaAs crystals originates from  $\text{Ga}_2\text{O}$  gas in the ampoule by reactions 4-2 and 4-15. Therefore, reaction 4-1 supplies  $\text{Ga}_2\text{O}$  from the melt and the quartz boat and keeps the  $P_{\text{Ga}_2\text{O}}$  at equilibrium.

#### 4-4-1-c. Si Concentration

The ampoule was evacuated to eliminate oxygen adsorbed on the surface of quartz and the materials, and oxygen was not doped into the materials in the quartz ampoule. Reactions 4-1 and 4-2 require  $\text{Ga}_2\text{O}$  gas sources to satisfy the equilibrium condition. If Si did dissolve from the quartz boat into GaAs melt by reaction 4-1 to

supply  $\text{Ga}_2\text{O}$  gas to the inside of the quartz ampoule, Si concentration in GaAs crystals would increase with oxygen concentration. However, the experimental results show that the Si concentration in GaAs crystals does not increase with oxygen concentration, as shown in Table 4-1.

Reaction 4-1, which is the reaction between the Ga in the melt and quartz boat to produce  $\text{Ga}_2\text{O}$  gas, will produce dissolved Si near the inner surface of the quartz boat and near the top surface of GaAs melt. This reaction 4-1 continues to supply  $\text{Ga}_2\text{O}$  gas to the quartz ampoule until the  $\text{Ga}_2\text{O}$  pressure reaches the equilibrium condition. This condition promotes reaction 4-3, which is the reaction between Si in the melt and quartz to produce SiO gas.

The rate of reaction 4-3 depends on the Si concentration as shown in equation 4-7. Table 4-2 shows the relationship between the calculated Si concentration ( $n_e$ ) and the measured carrier concentration ( $n_c$ ) in undoped and Si-doped GaAs crystals.

Si concentration was calculated from the equation of distribution [1]:

$$n_e = k_{\text{Si}} N_{\text{Si}}^I (1-g)^{k_{\text{Si}}-1}, \quad (4-21)$$

where  $k_{\text{Si}}$  is the segregation coefficient of Si in GaAs melt,  $N_{\text{Si}}^I$  is the initial Si concentration in GaAs melt and  $g$  is the fraction solidified.

The measured carrier concentration was lower than the calculated value because of the amphoteric property of Si. When the initial Si doping concentration in GaAs melt is about  $1 \times 10^{-4}$  by weight ratio, the carrier concentration increases in proportion to the calculated Si concentration. This initial Si concentration corresponds to the range where Si concentration in the melt is reduced by reaction 4-3. This range is represented by the area above the equilibrium line for reactions 4-3 and 4-4 in Fig. 4-5. The rate of reaction 4-3 is assumed to be very low when the initial Si concentration is about  $1 \times 10^{-4}$  by weight ratio.

The Si concentration near the inner surface of the quartz boat and near the top surface of GaAs melt is probably higher than  $1 \times 10^{-4}$  because of reaction 4-1. The rate of reaction 4-3 of this region is probably faster than in other regions, and almost all of



Table 4-2 Calculated Si concentration ( $n_e$ ) versus measured carrier concentration ( $n_c$ ) at 300 K, with the fraction solidified  $g$  and diffusion barrier temperature  $T_d$  under different initial Si concentrations in GaAs melt (weight ratio). Carrier concentration is not reduced by reactions 4-3 and 4-4, when the initial Si concentration in GaAs melt is higher than  $1 \times 10^{-4}$  by weight ratio.

Initial $N_{Si}$	$T_d$ (K)	$g$	Seed side		$g$	Tail side	
			$n_e$ ( $cm^{-3}$ )	$n_c$ ( $cm^{-3}$ )		$n_e$ ( $cm^{-3}$ )	$n_c$ ( $cm^{-3}$ )
0	1361.5	0.15	—	$1.8 \times 10^{16}$	0.75	—	$8.2 \times 10^{15}$
$4.21 \times 10^{-5}$	1309.7	0.15	$7.7 \times 10^{17}$	$4.8 \times 10^{17}$	0.75	$2.2 \times 10^{18}$	$9.6 \times 10^{17}$
$1.06 \times 10^{-4}$	1300.8	0.15	$1.9 \times 10^{18}$	$1.0 \times 10^{18}$	0.75	$5.6 \times 10^{18}$	$2.1 \times 10^{18}$

the dissolved Si probably escape into the gas phase. Consequently, the Si concentration in GaAs crystals does not increase with increasing oxygen concentration.

#### 4-4-2. Effect of Oxygen in GaAs Crystals

##### 4-4-2-a. Electronic Properties

The relationship between oxygen concentration in GaAs crystals and carrier concentration is shown in Figs. 4-3 and 4-4. There is scarcely any difference between undoped and Si-doped GaAs crystals. In this section, whole discussion is concentrated on undoped GaAs crystals to investigate this relationship in detail. Here,  $T_d$  is used as an indication of the oxygen concentration in GaAs crystals, because  $T_d$  dominantly controls the oxygen concentration.

Figure 4-6 shows the relationship between  $T_d$  and  $\theta$  measured at 77 K.  $\theta$  is defined for n-type material by:

$$\theta = N_A^- / N_D^+, \quad (4-22)$$

where  $N_A^-$  is the ionized acceptor concentration and  $N_D^+$  is the ionized donor concentration. The value of  $\theta$  at 77 K is calculated from Hall measurements using the table supplied by Walukiewicz et al. [26].

In Fig. 4-6,  $\theta$  decreases with raising the temperatures  $T_d$ , so  $\theta$  decreases as the oxygen concentration in GaAs crystals increases. One can obtain  $N_A^-$  and  $N_D^+$  at 77 K from the following equation, using  $\theta$  and carrier concentration  $n_c$ :

$$N_A^- = \theta n_c / (1 - \theta), \quad (4-23)$$

$$N_D^+ = n_c / (1 - \theta). \quad (4-24)$$

Values of  $n_c$ ,  $N_A^-$ ,  $N_D^+$  and  $N_{tot}$  ( $N_{tot} = N_A^- + N_D^+$ ) are plotted against  $T_d$  in Fig. 4-7. Here,  $N_A^-$  decreases with raising  $T_d$ , and  $N_D^+$  does not change with the variation of  $T_d$ . The reason for the increase in carrier concentration with that of oxygen concentration in undoped GaAs crystals as shown in Fig. 4-3 is the decrease in the number of acceptors. So, oxygen in GaAs crystals is thought to suppress acceptors.

Oxygen in GaAs crystals can substitute at an As-site and act as a deep donor as confirmed with GaAs crystals grown with oxygen doping [42,45-47]. In undoped GaAs



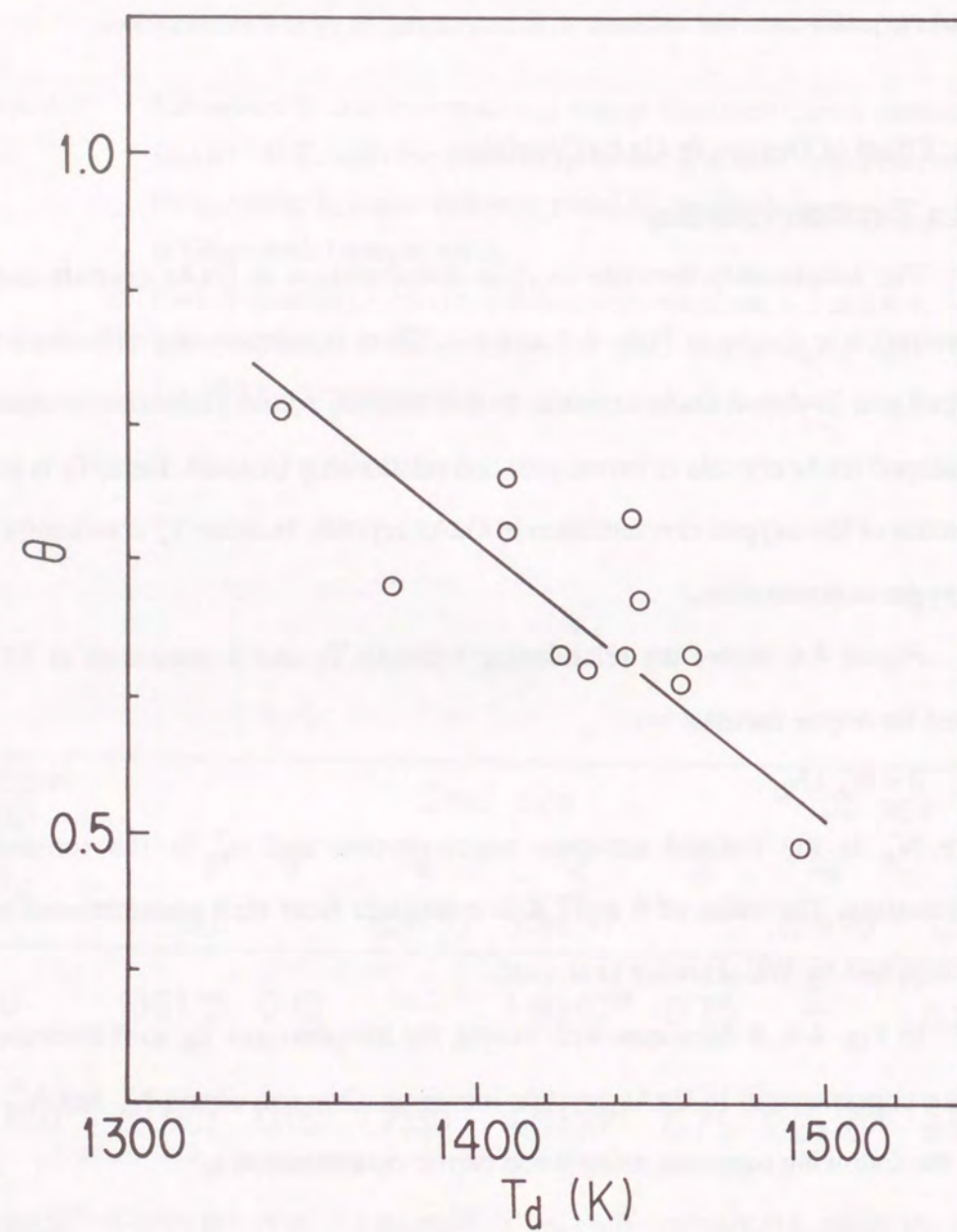


Fig. 4-6 Diffusion barrier temperature  $T_d$  versus compensation ratio  $\theta$  of undoped GaAs crystals at 77 K.

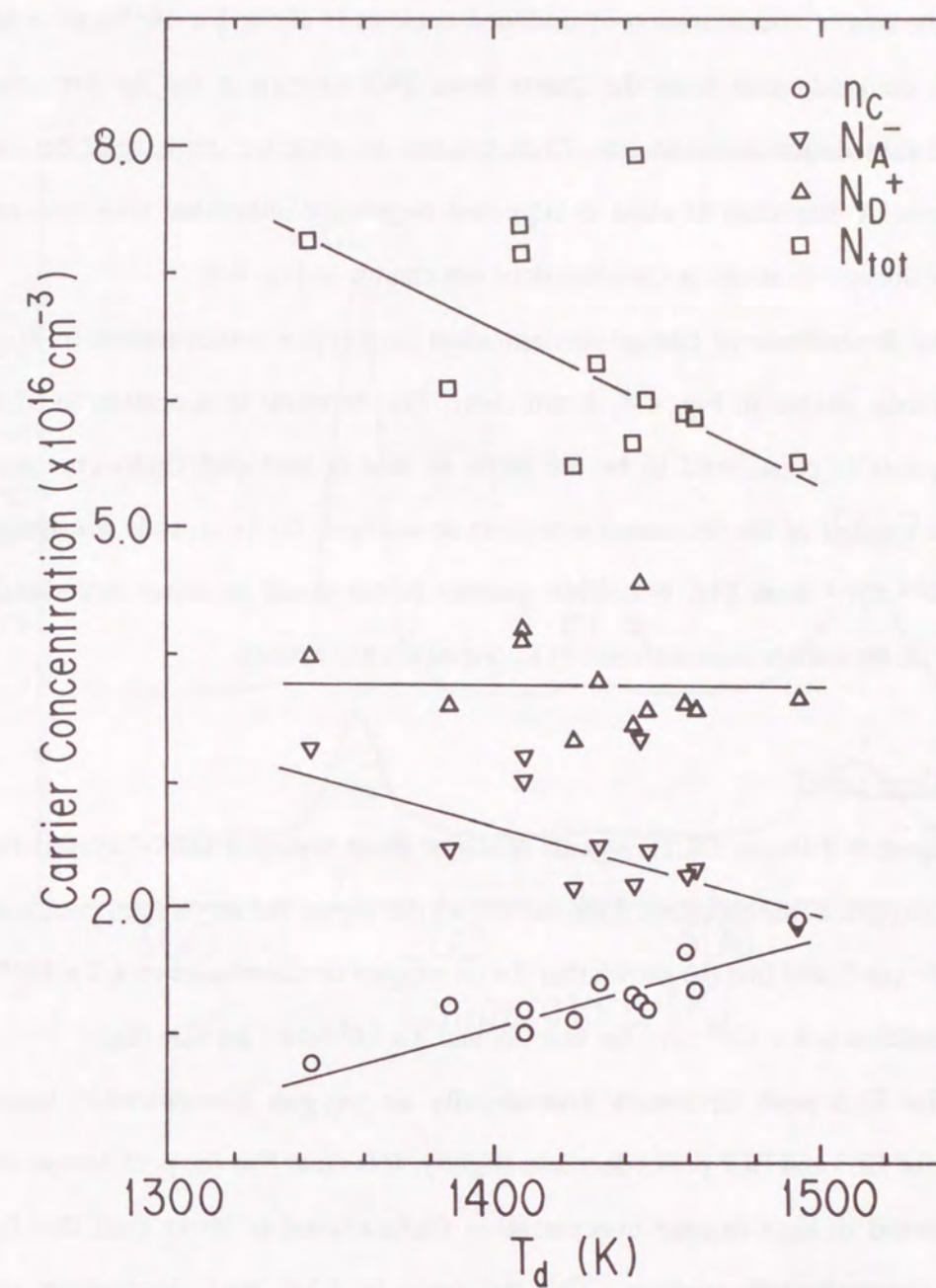


Fig. 4-7 Carrier concentration  $n_c$ , activated acceptor concentration  $N_A^-$ , activated donor concentration  $N_D^+$  and  $N_{\text{tot}}$  ( $N_{\text{tot}} = N_A^- + N_D^+$ ) at 77 K plotted against diffusion barrier temperature  $T_d$ .  $N_A^-$ ,  $N_D^+$ , and  $N_{\text{tot}}$  calculated from  $n_c$  and mobility at 77 K.



crystals, the existence of oxygen-induced deep donor levels can not be confirmed, because the carrier concentration of undoped crystals is about  $1 \times 10^{16} \text{ cm}^{-3}$  which is mainly Si contamination from the quartz boat. This oxygen at the As-site seems to prevent Si substitution at the As-site. Thus, it seems to cause the decrease of the number of acceptors. A displaced Si atom is supposed to occupy interstitial sites because the number of donors, Si atoms at Ga-sites, does not change in Fig. 4-7.

The dependence of carrier concentration on oxygen concentration in Si-doped GaAs crystals, shown in Fig. 4-4, is not clear. The decrease in acceptors in Si-doped GaAs crystals is considered to be the same as that in undoped GaAs crystals. The maximum number of the decreased acceptors in undoped GaAs crystals is estimated to be  $1 \times 10^{16} \text{ cm}^{-3}$  from Fig. 4-7. This number is too small to cause any significant influence on the carrier concentration in Si-doped GaAs crystals.

#### 4-4-2-b. Deep Level

Figure 4-8 shows DLTS signals obtained from undoped GaAs crystals for two different oxygen concentrations. Line (a) shows the signal for an oxygen concentration of  $5 \times 10^{15} \text{ cm}^{-3}$ , and line (b) shows that for an oxygen concentration of  $4.9 \times 10^{18} \text{ cm}^{-3}$ . Si concentration is  $4 \times 10^{16} \text{ cm}^{-3}$  for line (a), and  $3 \times 10^{16} \text{ cm}^{-3}$  for line (b).

The EL6 peak decreases dramatically as oxygen concentration increases, however the EL3 and EL2 peaks decrease slightly. It is clear that the peak temperature of EL2 observed in high oxygen concentration GaAs crystal is lower than that for low oxygen concentration crystals. The decrease in EL6 with increasing oxygen concentration has been reported with respect to the experiments on  $\text{Ga}_2\text{O}_3$  doped GaAs crystals by Martin et al. [46]. A shift of EL2 peak position has been reported by Gatos et al. [47] and Lagowski et al. [52]. This shift is well explained by an overlap of the oxygen-related peak of ELO with the EL2 peak.

Fang et al. [53] reported that EL2 was supposed to be  $\text{As}_{\text{Ga}}\text{-V}_{\text{As}}$ , and EL6 to be  $\text{V}_{\text{Ga}}\text{-V}_{\text{As}}$ .  $\text{V}_{\text{As}}$  is assumed to change to  $\text{O}_{\text{As}}$  with increasing oxygen concentration. The decrease in EL6 might explain the occupation of oxygen in  $\text{V}_{\text{As}}$ , i.e., the change of  $\text{V}_{\text{As}}$

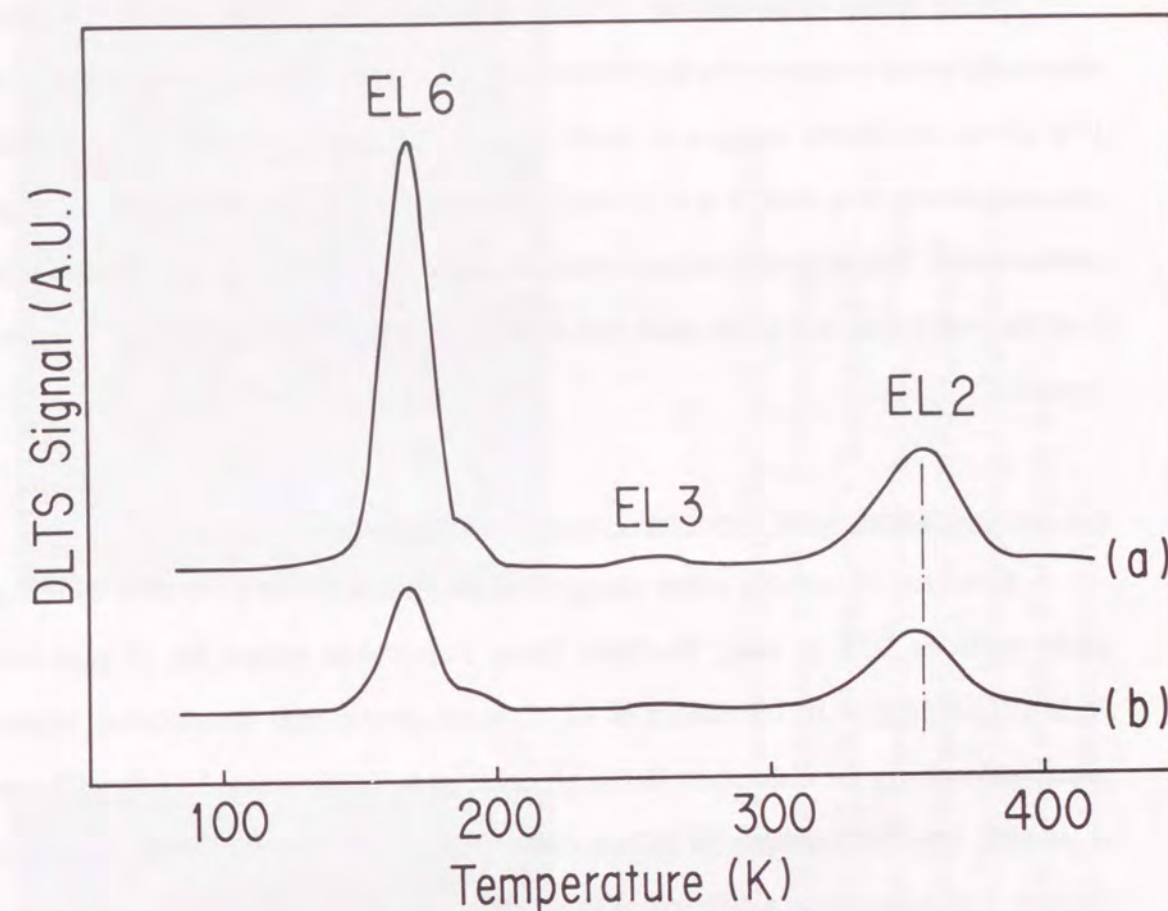


Fig. 4-8 DLTS signals obtained at two different oxygen concentrations in undoped GaAs crystals: line (a)  $5 \times 10^{15} \text{ cm}^{-3}$  and line (b)  $4.9 \times 10^{18} \text{ cm}^{-3}$ .



to  $O_{As}$ . The peak position shift of EL2 might also explain the change in complex state from  $As_{Ga}-V_{As}$  to  $As_{Ga}-O_{As}$ . The origin of EL3 is not clear, but is thought to be related to  $Si_{As}$  or  $V_{As}$  because of the change in peak height of oxygen concentration.

These results show that the oxygen contamination from the quartz boat brings electrically active centers in GaAs crystals, but the quantity of active oxygen is less than 1 % of the introduced oxygen in GaAs crystals because the calculated EL6 defect concentration is less than  $1 \times 10^{16} \text{ cm}^{-3}$  even in the samples with highest oxygen concentration. The activated oxygen atoms in GaAs crystals due to the contamination from the quartz boat acts in the same way as those generated from doped  $Ga_2O_3$  in GaAs crystals.

#### 4-4-2-c. Concentrations of Impurities Along Dislocation Lines

Existence of impurity atoms along dislocation lines is easy to observe by etching wafer surfaces [21]. In case, Si-doped GaAs wafers was etched for 25 min using  $H_2SO_4:H_2O_2:H_2O = 10:1:1$  etchant at  $10^\circ\text{C}$  under strong light illumination. Impurity precipitation along the dislocation line is observed as a contrast caused by the difference in etching rate. Photographs of etched (100) surfaces are shown in Fig. 4-9. These pictures were taken using a differential interference optical microscope: Figure 4-9(a) is the case of a higher oxygen concentration GaAs crystal, and Fig. 4-9(b) is that of a lower oxygen concentration one. These two crystals were grown from the same starting materials, on the common conditions except for the difference in  $T_d$ . There is a much greater precipitation of impurities along the dislocation line in the higher oxygen concentration GaAs crystal than in the lower oxygen concentration crystal. These results can be explained by assuming that the precipitation of impurities is due to oxide.

#### 4-4-2-d. Chemical Forms of Oxygen in GaAs Crystals

As already stated, oxygen can not be detected quantitatively by using SIMS, but large amounts of oxygen are detected by using CPA. From this impurity analytical result and from the wafer etching result, it is considered that almost all of the oxygen in GaAs

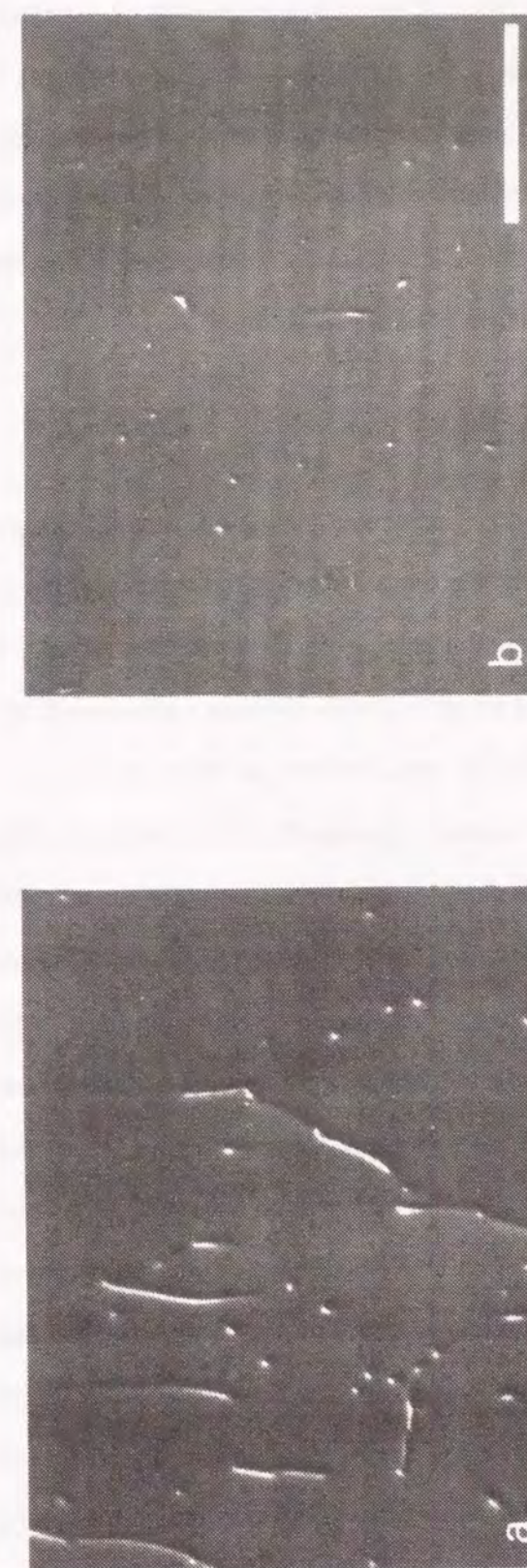


Fig. 4-9

Interference optical microscope photographs obtained from Si-doped GaAs wafers. The wafers were etched for 25 minutes using  $H_2SO_4:H_2O_2:H_2O = 10:1:1$  etchant at  $10^\circ\text{C}$  under strong light. The initial Si concentration in GaAs melt was  $1.06 \times 10^{-4}$  weight ratio and the fraction solidified  $g$  was 0.4. (a) diffusion barrier temperature  $T_d$  is  $1463.2 \text{ K}$  for photograph and etch pit density is  $2.8 \times 10^3 \text{ cm}^{-3}$ . (b)  $T_d$  is  $1300.8 \text{ K}$  and etch pit density is  $2.4 \times 10^3 \text{ cm}^{-3}$ . Marker represents  $500 \mu\text{m}$ .



crystals consists of segregated oxides (such as  $\text{Ga}_2\text{O}_3$ ,  $\text{As}_2\text{O}_3$ ,  $\text{GaAsO}_4$ , and  $\text{SiO}_2$ ) [54,55].

A small amount of oxygen, less than 1 %, introduced into GaAs crystals is supposed to substitute at As-sites without forming such oxides. This oxygen substitution at As-sites would explain the difference in the electronic properties of undoped GaAs crystals and the difference in DLTS signals [56]. These electrical phenomena would not be clear in Si-doped GaAs because of the presence of a large amount of Si.

#### 4-5. CONCLUSION

The concentration of oxygen in GaAs crystals grown by the GF method using a quartz ampoule can be controlled by adjusting the temperature of the diffusion barrier  $T_d$ , which is located between the higher temperature zone in the apparatus of crystal growth and the lower temperature zone placed so as to control the vapor pressure of As. In this growth system,  $T_d$  is the lowest temperature spot in the higher temperature zone. The oxygen concentration in GaAs crystals increases remarkably as  $T_d$  increases. This can be explained by the equilibrium between oxygen concentration in GaAs melt and  $\text{Ga}_2\text{O}$  vapor pressure generated from the reaction between quartz and Ga. Oxygen concentration in GaAs crystals is proportional to the third power of  $\text{Ga}_2\text{O}$  pressure. Most of the contaminating oxygen atoms in GaAs crystals are thought to exist as oxides, and some of the As-sites are substituted by the remainder oxygen. These oxygen atoms at As-sites prevent Si atoms from substitution at As-sites and acting as an acceptor. Almost all of the Si atoms, which came from the quartz boat and dissolved in melt, are removed from the melt because of the other equilibrium relationships. The DLTS results show that the EL6 in undoped GaAs crystals decreases with increasing oxygen concentration. This is considered to be caused that  $V_{\text{Ga}}-V_{\text{As}}$ , the origin of the EL6, change to  $V_{\text{Ga}}-\text{O}_{\text{As}}$ . The precipitation of impurities along dislocation lines in Si-doped GaAs crystals observed by etching that is enhanced with increasing the oxygen concentration. This precipitation seems to be the experimental support that oxygen atoms have been considered to

segregate in GaAs crystals as oxide. These phenomena are the same as those in intentionally added oxygen atoms in GaAs crystals.



## 5. THE EFFECT OF ARSENIC VAPOR PRESSURE ON THE SPATIAL DISTRIBUTION OF SILICON

### 5-1. INTRODUCTION

It is well known that Si atoms occupy Ga-sites where they act as donors, or As-sites where they act as acceptors. A lot of work has already been done to understand the characteristics of Si-doped GaAs. The site distribution of Si in GaAs under the influence of a second dopant has been studied by measuring the Hall effect [57] and Si localized vibrational modes (LVM) [58,59]. They reported that the concentration of Si on As-site to Si on Ga-site ratio ( $[Si_{As}]/[Si_{Ga}]$ ) was dependent on the species and the amount of the second dopant. The ratio of activated acceptor concentration to activated donor concentration ( $N_A^-/N_D^+ = \theta$ : compensation ratio) measured by the Hall effect was reported to be about 0.4 in the carrier concentration range from  $5 \times 10^{17} \text{ cm}^{-3}$  to  $1.5 \times 10^{18} \text{ cm}^{-3}$  [60]. The distribution of Si was to be described by a thermo-chemical model, and was expected to be influenced by melt stoichiometry [61,62]. Fornari [63] reported that the distribution of Si in GaAs grown by the liquid encapsulated Czochralski (LEC) method was dependent on the melt stoichiometry.

In this chapter, the effect of As vapor pressure on site distribution of Si will be discussed in the case of the crystal grown by the GF method [33,64] which can control As vapor pressure around the melt directly. The result is discussed, being compared with a thermo-chemical model.

### 5-2. EXPERIMENTS

All GaAs crystals in this study were grown by the GF method, and from a melt synthesized from elemental Ga and As. As vapor pressure was controlled by the temperature at the low temperature zone. The As source temperature was varied from 610 °C to 635 °C. The weight ratio of added Si was 43.75 wtppm. All samples were

sliced from the single crystals, and from the position of fraction solidified (g) equaled 0.15, in order to keep the same sample condition.

Si concentration in GaAs crystals was measured by FL-AAS and SIMS. Hall effect measurements were carried out at 77 K using the VDP method. The compensation ratio was determined from the carrier concentration and Hall mobility at 77 K, using the table reported by Walukiewicz et al. [49].

### 5-3. RESULTS AND DISCUSSION

Figure 5-1 shows the relation among the Si concentration, carrier concentration and the As source temperature. Figure 5-2 shows the Hall mobility plotted against the As source temperature. The Si concentration was widely scattered from sample to sample because the measurement of FL-AAS used this chapter is not precise enough. The Si concentration of several samples measured by SIMS is around  $8 \times 10^{17} \text{ cm}^{-3}$ . Although the measurements have a large error, the Si concentration is thought to be constant at about  $6.5 \times 10^{17} \text{ cm}^{-3}$  by FL-AAS. Carrier concentration and mobility measured by the Hall effect increases with raising As source temperature.

Using the electrical properties measured at 77 K, the compensation ratio was calculated [49] as shown in Fig. 5-3. It is clear that the compensation ratio decreases with raising the As source temperature. One can obtain  $N_A^-$  and  $N_D^+$  from the relationship stated in section 4-4-2. Values of  $N_A^-$ ,  $N_D^+$ ,  $N_A^- + N_D^+$  are plotted against As source temperature in Fig. 5-4. The decrease in  $N_A^-$ , the increase in  $N_D^+$ , and constancy of  $N_A^- + N_D^+$  were observed with the increase in As source temperature. The crystal grown by the LEC method were reported to have a similar trend with compensation ratios [63].

It was shown that the compensation ratio calculated from electrical properties cannot be entirely explained in terms of the amphoteric behavior of Si measured by LVM [57,58,63]. Chen et al. [65,66] proposed new LVM models, but the  $[Si_{As}]/[Si_{Ga}]$  ratio was not suitable when the compensation ratio is calculated from electric properties.



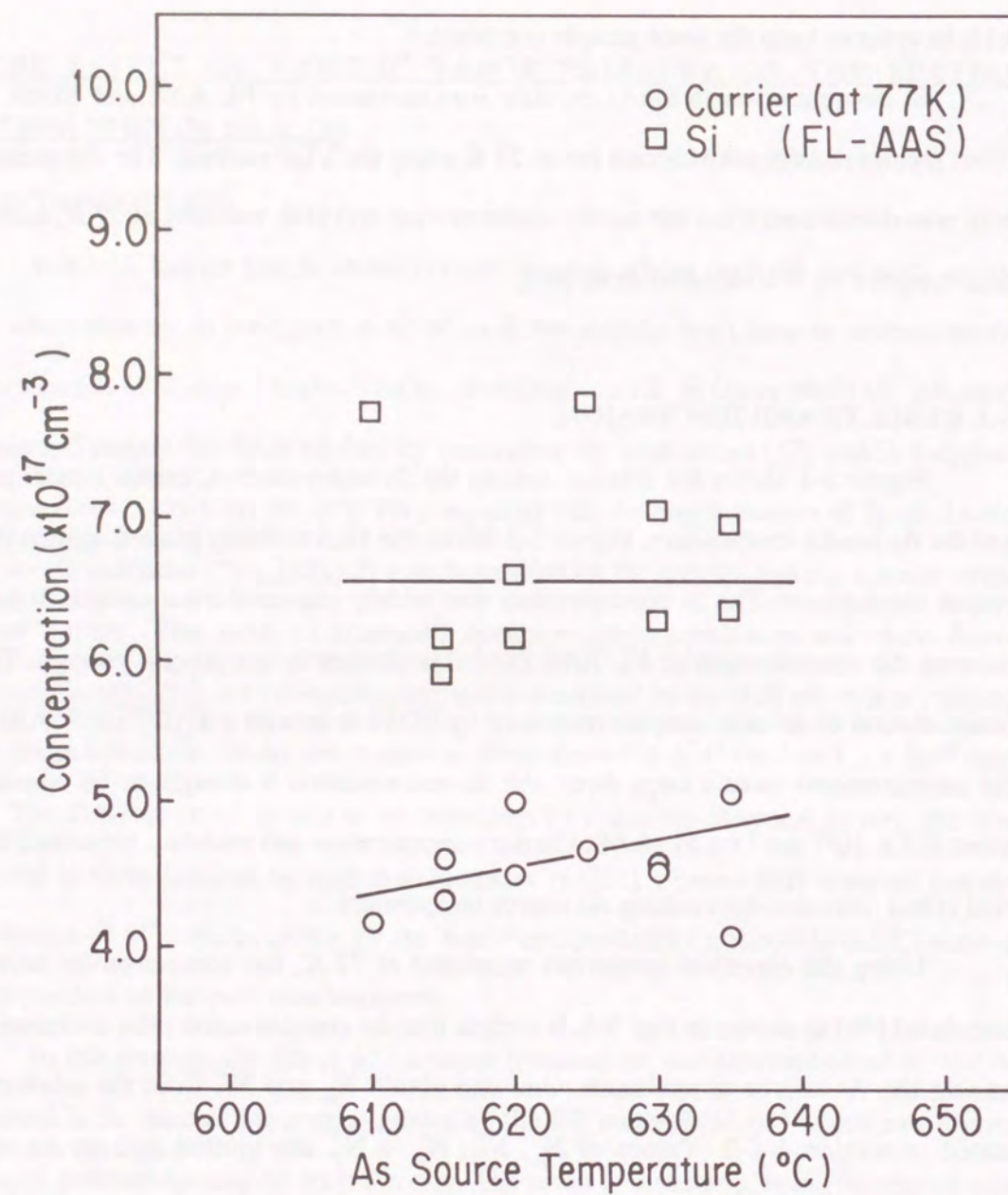


Fig. 5-1 The relationship between carrier concentration at 77 K, Si concentration, and As source temperature.

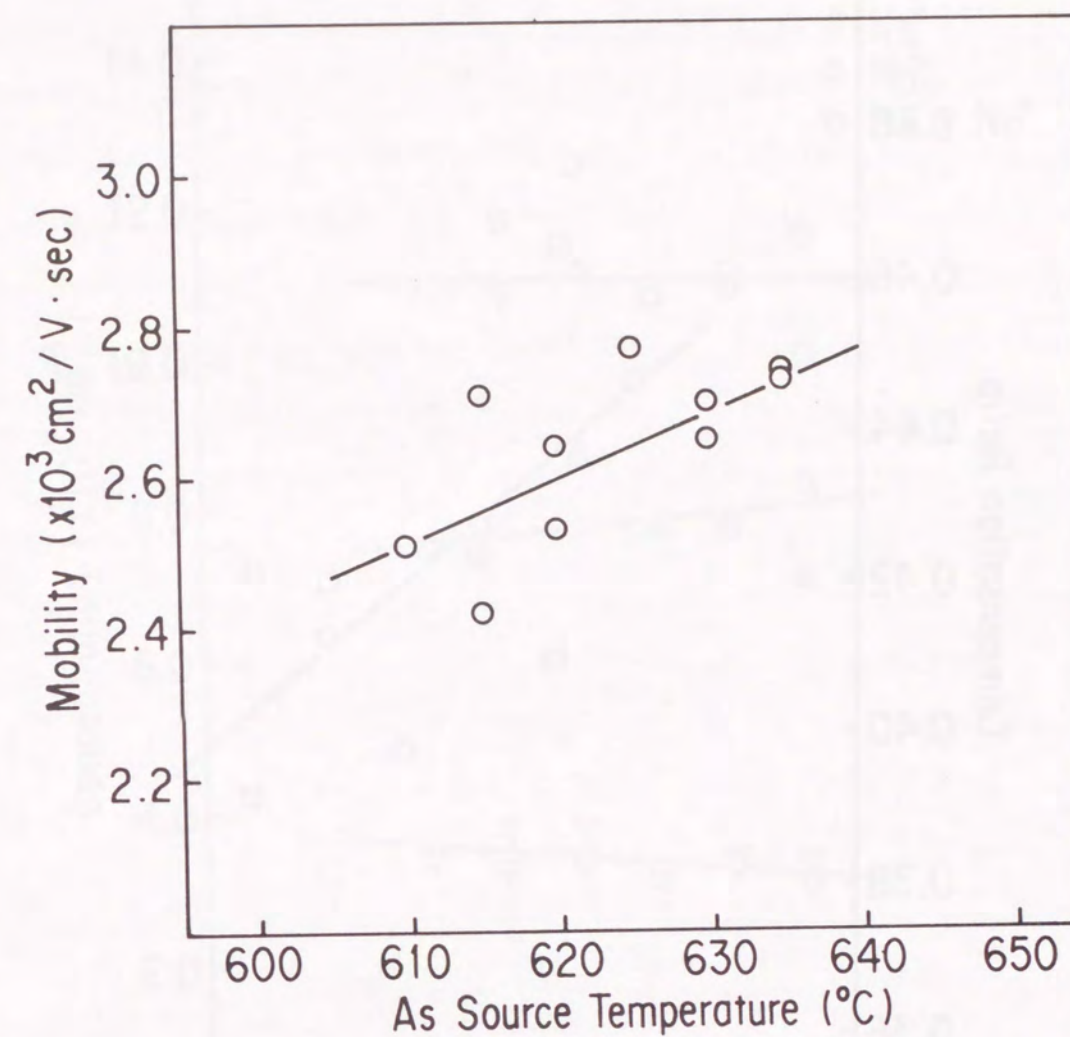


Fig. 5-2 The relationship between mobility at 77 K and As source temperature.



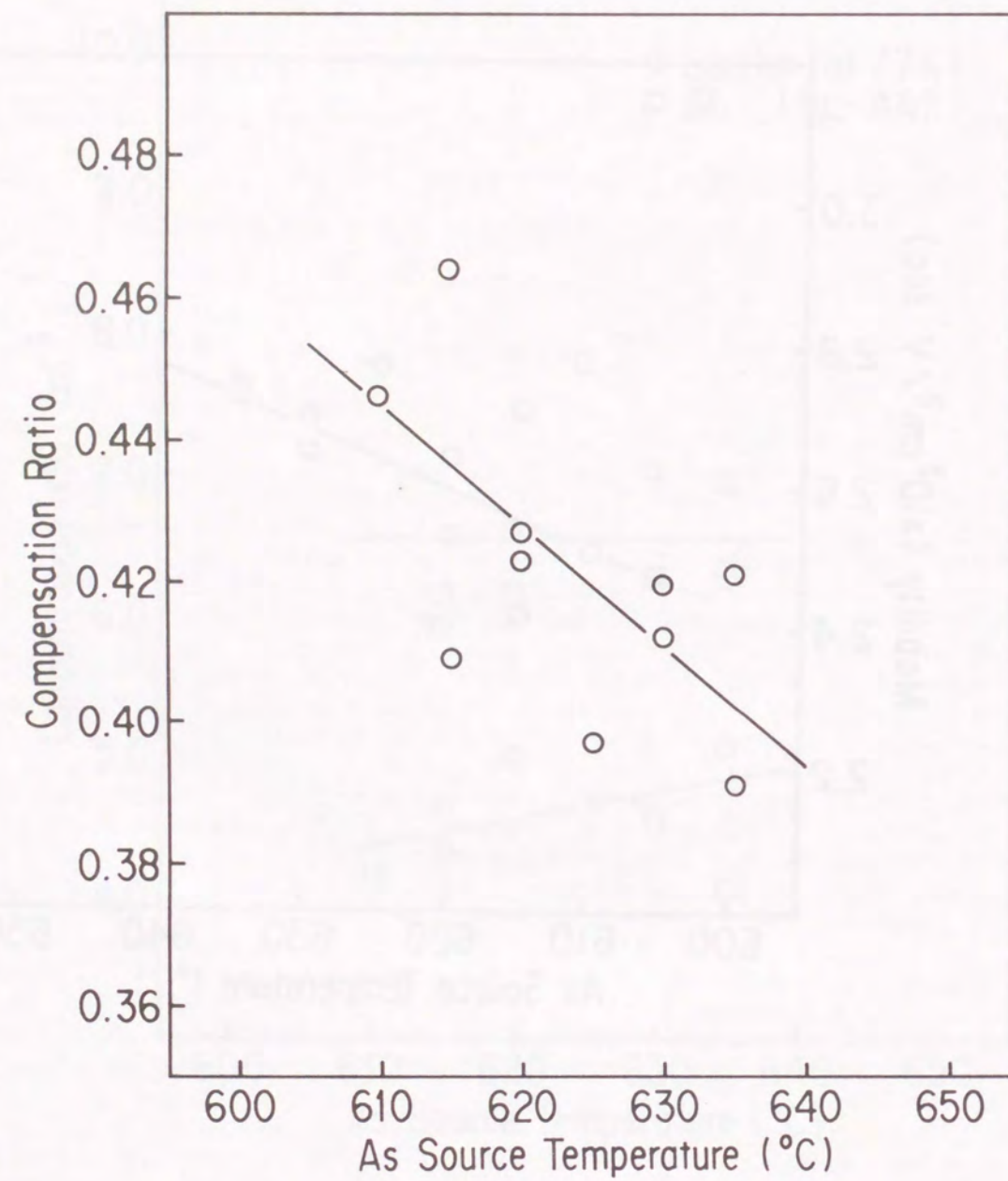


Fig. 5-3 Compensation ratio calculated from electrical properties versus As source temperature.

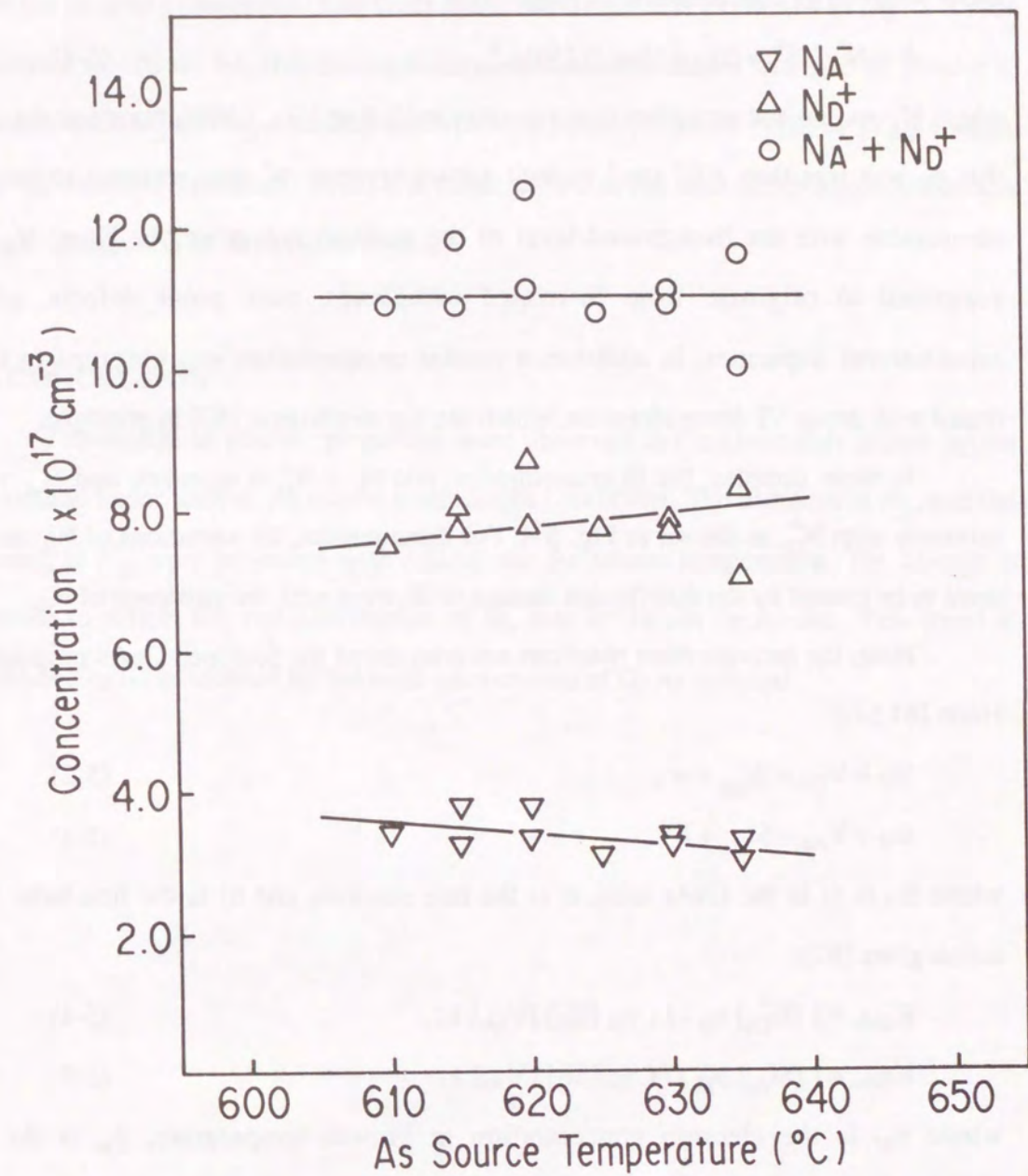


Fig. 5-4 Donor concentration and acceptor concentration calculated from electrical properties versus As source temperature.



Fornari [63] proposed the relationship which gives the compensation ratio in Si-doped GaAs with carrier concentration ( $n_c$ ) larger than  $10^{17} \text{ cm}^{-3}$ :

$$\theta = N_A^- / N_D^+ = (N_A' + [\text{Si}_{\text{As}}]) / [\text{Si}_{\text{Ga}}], \quad (5-1)$$

where  $N_A'$  are ionized acceptors concentration excluding  $[\text{Si}_{\text{As}}]$ . With regard to the cases that  $n_c$  was less than  $10^{17} \text{ cm}^{-3}$  in melt grown crystals,  $N_D^+$  was reported to become comparable with the background level of the residual acceptors [4]. Here,  $N_A'$  was suggested to originate from Si-related complexes, pure point defects, and/or substitutional impurities. In addition, a similar compensation was observed in GaAs doped with group VI donor elements, which are not amphoteric [60] in principle.

In these samples, the Si concentration and  $N_A + N_D^+$  is constant, and  $N_A^-$  varies inversely with  $N_D^+$ , as shown in Fig. 5-4. For these results, the variations of  $N_A^-$  and  $N_D^+$  seem to be caused by the distribution change of Si, even with the existence of  $N_A'$ .

Here, the incorporation reactions are considered for Si-doped GaAs proposed by Hurle [61,62]:



where  $\text{Si}_\ell$  is Si in the GaAs melt,  $e^-$  is the free electron, and  $h^+$  is the free hole. Mass action gives [62]:

$$K_{\text{SiGa}} = ([\text{Si}_{\text{Ga}}^+] n_{\text{gt}}) / (\gamma_{\text{Si}} [\text{Si}_\ell] [\text{V}_{\text{Ga}}]), \quad (5-4)$$

$$K_{\text{SiAs}} = ([\text{Si}_{\text{As}}^-] p_{\text{gt}}) / (\gamma_{\text{Si}} [\text{Si}_\ell] [\text{V}_{\text{As}}]), \quad (5-5)$$

where  $n_{\text{gt}}$  is the electron concentration at growth temperature,  $p_{\text{gt}}$  is the hole concentration at growth temperature, and  $\gamma_{\text{Si}}$  is the activity coefficient of Si in the GaAs melt.

Present experimental results were compared with the thermo-chemical model for undoped GaAs that was suggested by Wenzl et al. [5,67]. The influence of the foreign atoms was not considered in this calculation. When more detailed analysis is done, the influence of substitutional foreign atoms must be taken into account for the charge neutrality condition. The value of  $[\text{V}_{\text{Ga}}]$ ,  $[\text{V}_{\text{As}}]$ ,  $n_{\text{gt}}$ , and  $p_{\text{gt}}$  were calculated using the thermo-chemical constant proposed by Wenzl et al. [5] except for the regular solution

parameter. The value of this parameter, which was estimated to be  $\alpha = 13510 - 39.66 T$  from the present experiment. This thermo-chemical model is explained in Fig. 5-5. The calculated results on this thermo-chemical model are also shown in Fig. 5-6. Similar to the number of  $N_D^+$  and  $N_A^-$  from this experimental results, those of  $[\text{V}_{\text{Ga}}]$  or  $[\text{V}_{\text{As}}]$  change with As source temperature. Thus, it is considered that the melt composition influences the site distribution of Si in GaAs crystals.

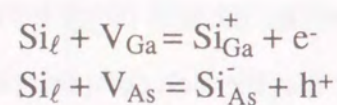
#### 5-4. CONCLUSION

The change in electric properties were observed in GaAs crystals grown by the GF method under various As source temperature conditions. The decrease in  $N_A^-$ , and the increase in  $N_D^+$  were observed with raising the As source temperature. The change is assumed to reflect the site distribution of Si, that is Ga-site or As-site. This trend is considered to be influenced by the melt composition of GaAs material.



### Si Incorporation Model

D. T. J. Hurle 5-th Conf. on  
Semi-Insulating III-V materials, 1988, p11



$$K_{\text{SiGa}} = ([\text{Si}_{\text{Ga}}^+] n) / (\gamma_{\text{Si}} [\text{Si}_\ell] [\text{V}_{\text{Ga}}])$$

$$K_{\text{SiAs}} = ([\text{Si}_{\text{As}}^-] p) / (\gamma_{\text{Si}} [\text{Si}_\ell] [\text{V}_{\text{As}}])$$

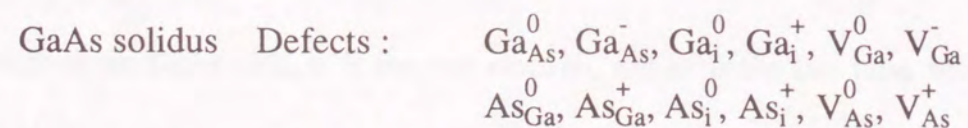
$\gamma_{\text{Si}}$  : activity coefficient of Si in GaAs melt

### GaAs Phase Diagram

H. Wenzl et al.  
J. Crystal Growth, 100 (1990), 377  
J. Crystal Growth, 109 (1991), 191

As vapor pressure (Ideal Gas)

GaAs liquidus (Regular solution model)



### When As Source Temperature Increase.

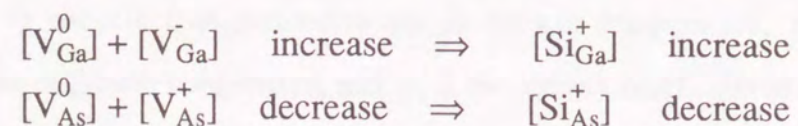


Fig. 5-5 (a)

## Thermo Chemical Model I

### As SOURCE

As pressure

$$P_{\text{As}_2\text{L}} = \exp\left(\frac{-22.72 \times 10^3}{T_L} + 19.23\right)$$

$$P_{\text{As}_4\text{L}} = \exp\left(\frac{-18.95 \times 10^3}{T_L} + 21.22\right)$$

Chemical potential

$$\Delta\mu_{\text{As}}^{\frac{1}{2}\text{As}_2(\text{g})} = 94428 - 79.93 T$$

$$\Delta\mu_{\text{As}}^{\frac{1}{4}\text{As}_4(\text{g})} = 39378 - 44.10 T$$

### LIQUIDUS

As pressure (Total Pressure)

$$P_H = P_{\text{As}_2\text{H}} + P_{\text{As}_4\text{H}} + P_{\text{Ga}} + P_{\text{AsL}}$$

$$P_{\text{As}_4\text{H}} = K_{\text{As}} P_{\text{As}_2\text{H}}^2$$

$$K_{\text{As}} = \exp\left(\frac{26.49 \times 10^3}{T_H} - 17.24\right)$$

Ga Pressure

$$\Delta\mu_{\text{As}}^\ell = \Delta G^0 - RT \ln(P_{\text{Ga}})$$

$$\Delta G^0 = -355186 + 134.82 T$$

Regular Solution Model

$$\Delta\mu_{\text{As}}^\ell = \Delta\mu_{\text{As}}^{0\ell} + \alpha(1-y)^2 + RT \ln(y)$$

$$\Delta\mu_{\text{As}}^{0\ell} = 23848 - 21.88T$$

$$\alpha = 13510 - 39.66T \quad (\text{from our results})$$

$$\Delta\mu_{\text{As}}^\ell = \Delta\mu_{\text{As}}^{\frac{1}{2}\text{As}_2(\text{g})} = \Delta\mu_{\text{As}}^{\frac{1}{4}\text{As}_4(\text{g})}$$

Liquidus

$$-\frac{1}{2}RT \ln(4y(1-y)) - \frac{1}{2}\Delta S^F(T^F - T) = \alpha\left(\frac{1}{2} - y\right)^2$$

$$\Delta S^F = 70 \quad (\text{J/mol})$$

$$T^F = 1513 \quad (\text{K})$$

Fig. 5-5 (b)



## Thermo Chemical Model II

**SOLIDUS**  $\Delta\mu_{As} = \Delta\mu_{As}^{\ell}$

$$As(c) = \frac{1}{2}As_{Ga}^0 + \frac{1}{2}As_{As}$$

$$\Delta\mu_{As} = BA0 + \frac{1}{2}RT \ln([As_{Ga}^0])$$

$$As(c) = \frac{1}{2}As_{Ga}^+ + \frac{1}{2}e^- + \frac{1}{2}As_{As}$$

$$\Delta\mu_{As} = BAP + \frac{1}{2}RT \ln([As_{Ga}^+] n)$$

$$As(c) + \frac{1}{2}Ga_{As}^0 = \frac{1}{2}Ga_{Ga} + As_{As}$$

$$\Delta\mu_{As} = AB0 - \frac{1}{2}RT \ln([Ga_{As}^0])$$

$$As(c) + \frac{1}{2}Ga_{As}^- + \frac{1}{2}h^+ = \frac{1}{2}Ga_{Ga} + As_{As}$$

$$\Delta\mu_{As} = ABM - \frac{1}{2}RT \ln([Ga_{As}^-] p)$$

$$As(c) = As_i^0$$

$$\Delta\mu_{As} = BI0 + RT \ln([As_i^0])$$

$$As(c) = As_i^+ + e^-$$

$$\Delta\mu_{As} = BIP + RT \ln([As_i^+] n)$$

$$As(c) + V_{As}^0 = As_{As}$$

$$\Delta\mu_{As} = VB0 - RT \ln([V_{As}^0])$$

$$As(c) + V_{As}^+ + e^- = As_{As}$$

$$\Delta\mu_{As} = VBP - RT \ln([V_{As}^+] n)$$

$$As(c) + Ga_i^0 = Ga_{Ga} + As_{As}$$

$$\Delta\mu_{As} = AI0 - RT \ln([Ga_i^0])$$

$$As(c) + Ga_i^+ + e^- = Ga_{Ga} + As_{As}$$

$$\Delta\mu_{As} = AIP - RT \ln([Ga_i^+] n)$$

$$As(c) = As_{As} + V_{Ga}^0$$

$$\Delta\mu_{As} = VA0 + RT \ln([V_{Ga}^0])$$

$$As(c) = As_{As} + V_{Ga}^- + h^+$$

$$\Delta\mu_{As} = VAM + RT \ln([V_{Ga}^-] p)$$

$$0 = e^- + h^+$$

$$0 = I + RT \ln(np)$$

$$As_{Ga}^0 : BA0$$

$$BA0 = 48500$$

$$As_{Ga}^+ : BAP$$

$$BAP = 84000 + 30T$$

$$Ga_{As}^0 : AB0$$

$$AB0 = -136000$$

$$Ga_{As}^- : ABM$$

$$ABM = -140000 - 21T$$

$$As_i^0 : BI0$$

$$BI0 = 155000$$

$$As_i^+ : BIP$$

$$BIP = 157000 + 69T$$

$$V_{As}^0 : VB0$$

$$VB0 = -194500$$

$$V_{As}^+ : VBP$$

$$VBP = -213500 - 66T$$

$$Ga_i^0 : AI0$$

$$AI0 = -210000$$

$$Ga_i^+ : AIP$$

$$AIP = -211000 - 69T$$

$$V_{Ga}^0 : VA0$$

$$VA0 = 193000$$

$$V_{Ga}^- : VAM$$

$$VAM = 194000 + 43T$$

$$e-h : I$$

$$I = 170000 + 54T$$

*Charge Neutrality*

$$p + [As_{Ga}^+] + [As_i^+] + [Ga_i^+] + [V_{As}^+] = n + [Ga_{As}^-] + [V_{Ga}^-]$$

Fig. 5-5 (c)

Fig. 5-5 Thermochemical model of Si incorporation model [62] and Ga-As phase diagram proposed by Wenzl et al. [5,67]. (a) Basic parameter. (b) Chemical potential of As source and liquidus. (c) Chemical potential of solidus.

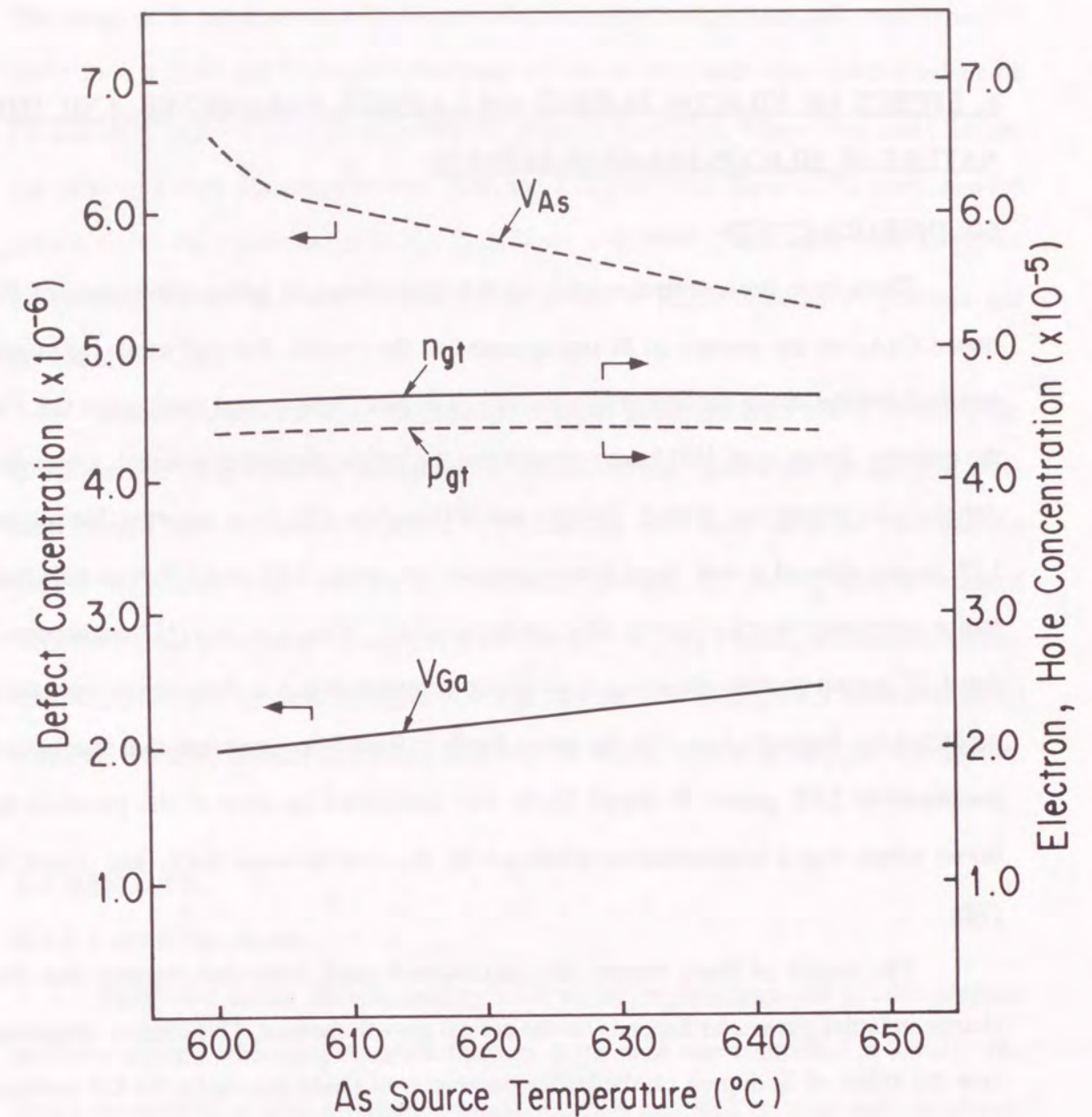


Fig. 5-6

Defect concentration per sublattice site at the melting point calculated from the model proposed by Wenzl et al. [5,67].

Here,

$$[V_{Ga}] = [V_{Ga}^-] + [V_{Ga}^0],$$

$$[V_{As}] = [V_{As}^+] + [V_{As}^0].$$



## **6. EFFECT OF SILICON DOPING ON LATTICE PARAMETER AND THE NATURE OF SILICON RELATED DEFECTS**

### **6-1. INTRODUCTION**

There have been several studies on the dependence of lattice parameters of Si-doped GaAs on the amount of Si incorporated in the crystal. Driscoll et al. [68] have reported that the lattice parameter of a heavily Si-doped GaAs crystal was contracted. On the contrary, Baker et al. [69] have reported that the lattice parameter of a melt grown Si-doped GaAs crystal was dilated. Fewster and Willoughby [70] have reported that p-type LPE layers showed a very large lattice contraction, while VPE and GF materials had lattice parameters much closer to their undoped values. Watson et al. [71] have reported that LEC grown crystals showed a large lattice contraction that is three times larger than predicted by Vegard's law. On the other hand, it has been reported that the lattice parameter of LEC grown Si-doped GaAs was contracted because of the presence of boron which was a contamination produced by reaction between  $B_2O_3$  and doped Si [72].

The results of these reports are inconsistent each other and suggest that the change in lattice parameter depends on the crystal growth method. This chapter describes how the effect of Si doping on the lattice parameter of GaAs grown by the GF method has been examined, and the effect of heat treatment of crystals and melt composition is considered. The crystals were studied using Hall measurement and by photoluminescence. Possible defect models based on these results will be discussed.

### **6-2. EXPERIMENTS**

The GaAs crystals were grown by the GF method [33,64], and from a melt synthesized from elemental Ga and As. The impurity concentrations in the crystals were measured by SIMS. The diffusion barrier temperature during crystal growth was around 1300 K. The impurity concentrations were less than the background levels, except for Si.

The range of Si concentration in the crystals, including undoped crystals, was from  $7 \times 10^{16}$  to  $4 \times 10^{19} \text{ cm}^{-3}$ . Atomic fractions of As in the melt were controlled to be  $[As]/([Ga]+[As]) = 0.5015$  by adjusting As pressure [6,62,73]. Where  $[As]$  and  $[Ga]$  are the value of As and Ga concentration in the melt, respectively. Some of the samples were grown under the condition of  $[As]/([Ga]+[As]) = 0.5000$ . There were used as-grown crystals and crystals that were bulk-annealed at 850 °C for 20 hr under As pressure and cooled at 30 °C/h.

Lattice parameters were measured by  $CuK\alpha_1$  radiation at  $25 \pm 1$  °C by using the Bond method [22]. Polished and etched 10 mm x 10 mm square shaped samples were used for this measurement. The electrical evaluations were done using the VDP method [26] at 300 K and 77 K. Then, the compensation ratio ( $\theta$ ),  $N_A$ , and  $N_D^+$  were determined from the carrier concentration and Hall mobility at 77 K [49]. Photoluminescence spectra [28] was analyzed on same samples at 4.2 K. An  $Ar^+$  ion laser (514.5 nm wavelength) was used to excite carriers and a Ge photodetector was used to detect the photo emission.

### **6-3. RESULTS**

#### **6-3-1. Lattice Parameter**

Figure 6-1 shows the relationship between lattice parameter and Si concentration in GaAs crystals where the As atom fraction in the melt was controlled at 0.5015. The lattice parameters of both as-grown crystals and bulk annealed crystals were measured. Under the present experimental condition, the observed lattice parameters seem to depend on Si concentration.

After etching in the solution of  $HNO_3:HF:H_2O = 3:1:4 + AgNO_3$  0.3 wt% [14], micro-sized roughness is recognized on the (111) As surface of the specimen, the Si concentration of which was higher than  $2 \times 10^{19} \text{ cm}^{-3}$ , as shown in Fig. 6-2. This surface is similar in roughness on etched surface of a heavily Te-doped GaAs [74]. This seems to be caused by something like segregation. In practice, stacking faults have been observed



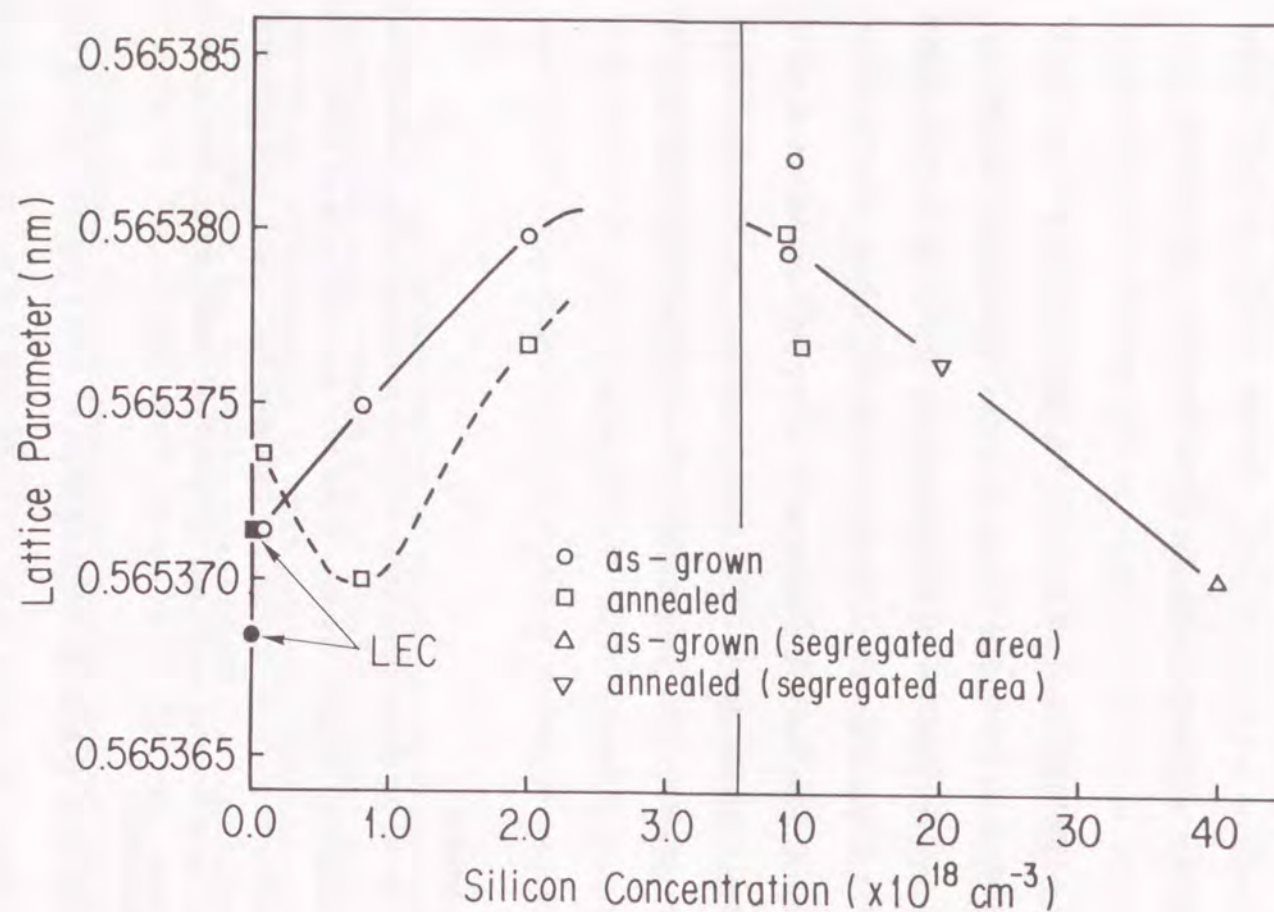


Fig. 6-1 Dependence of lattice parameter on Si concentration in as-grown and annealed GaAs crystals with As atom fractions of 0.5015 in the melt.

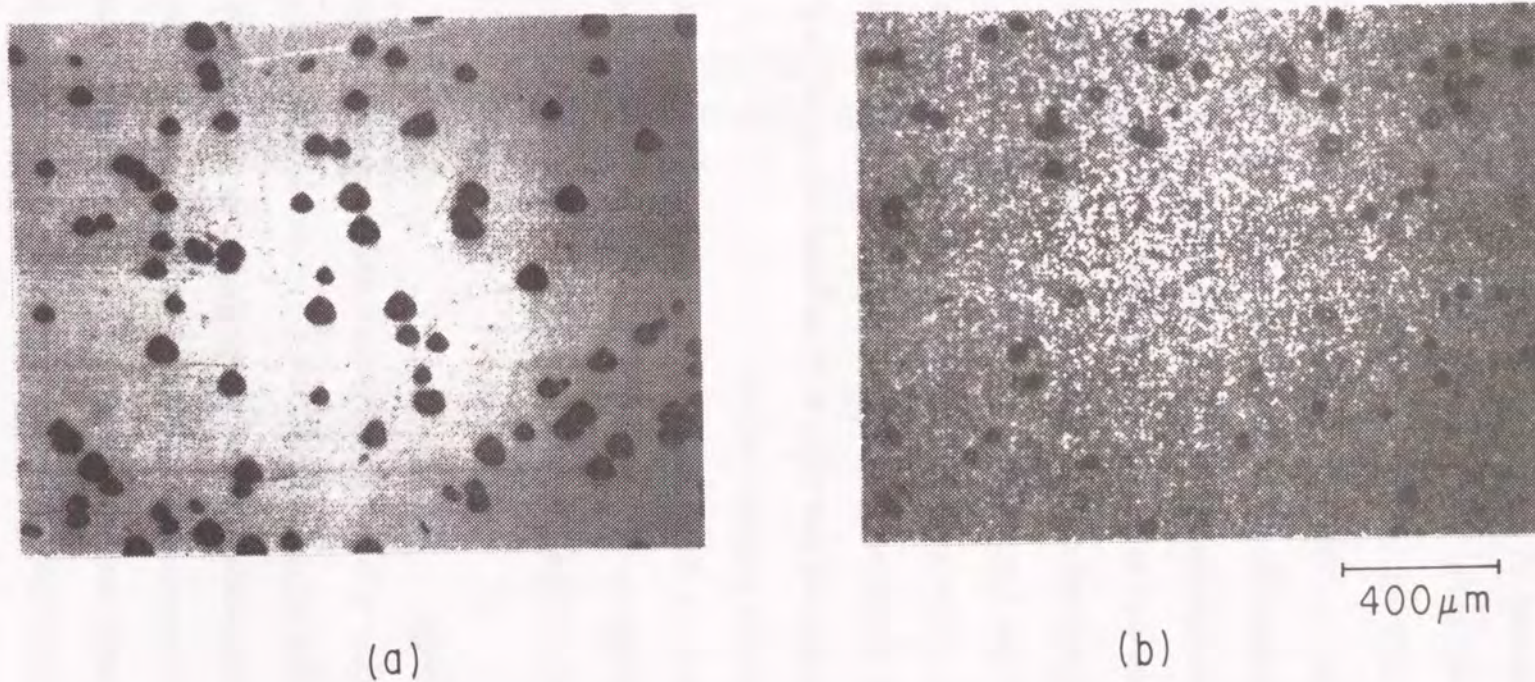


Fig. 6-2 Chemical etched (111) As surfaces using  $\text{HNO}_3:\text{HF}:\text{H}_2\text{O} = 3:1:4$  +  $\text{AgNO}_3$  0.3 wt% solution for 3 min. (a) Si concentration is  $5 \times 10^{18} \text{ cm}^{-3}$ , (b)  $2 \times 10^{19} \text{ cm}^{-3}$ . The surface background have very small roughness.



in heavily Si-doped GaAs by using TEM [34]. In addition, X-ray was scattered at the segregation region by using XRT as discussed in chapter 7.

The lattice parameters of undoped LEC GaAs crystals with low boron concentration are also plotted in Fig. 6-1. The lattice parameter of as-grown crystals with a Si concentration of  $8 \times 10^{16} \text{ cm}^{-3}$  is about 0.565370 nm, which is almost the same as that of undoped LEC GaAs crystals. The lattice parameter increases up to around 0.56538 nm with increasing the Si concentration up to about  $2 \times 10^{18} \text{ cm}^{-3}$ . However, above  $8 \times 10^{18} \text{ cm}^{-3}$ , the lattice parameter decreases with increasing Si concentration.

The annealed crystal with Si concentration of  $8 \times 10^{16} \text{ cm}^{-3}$  was observed to have a lattice parameter greater than that of as-grown crystal. This is the same as the change in lattice parameter of undoped LEC crystals. In the case of GaAs crystals with a Si concentration of between  $1 \times 10^{17} \text{ cm}^{-3}$  and  $2 \times 10^{18} \text{ cm}^{-3}$ , annealed specimens showed a smaller lattice parameter in comparison with that of as-grown crystals. The annealed crystals with a Si concentration of above  $2 \times 10^{18} \text{ cm}^{-3}$  showed scarcely any change in lattice parameter compared with as-grown crystals.

From these results, it becomes clear that the relationship between Si concentration and lattice parameter can be classified into four ranges of Si concentration: i.e., less than  $1 \times 10^{17} \text{ cm}^{-3}$ ,  $1 - 20 \times 10^{17} \text{ cm}^{-3}$ ,  $2 - 8 \times 10^{18} \text{ cm}^{-3}$ , and over  $8 \times 10^{18} \text{ cm}^{-3}$ .

### 6-3-2. Electrical Properties

Although the behavior of Si in GaAs crystals is amphoteric, all the samples used in this study exhibited n-type conductivity. Figure 6-3 shows the dependence of carrier concentration on the Si concentration in each specimen. Carrier concentration increased linearly with increasing Si concentration below  $2 \times 10^{18} \text{ cm}^{-3}$ . Above  $2 \times 10^{18} \text{ cm}^{-3}$ , this trend on the increase of carrier concentration became weaker. Eventually, in the range of Si concentration above  $8 \times 10^{18} \text{ cm}^{-3}$ , the carrier concentration of the crystals approached asymptotically around  $4 \times 10^{18} \text{ cm}^{-3}$ .

Annealed crystals exhibited the increase in carrier concentration which was larger than as-grown crystals when the Si concentration was below  $2 \times 10^{18} \text{ cm}^{-3}$ . In the range

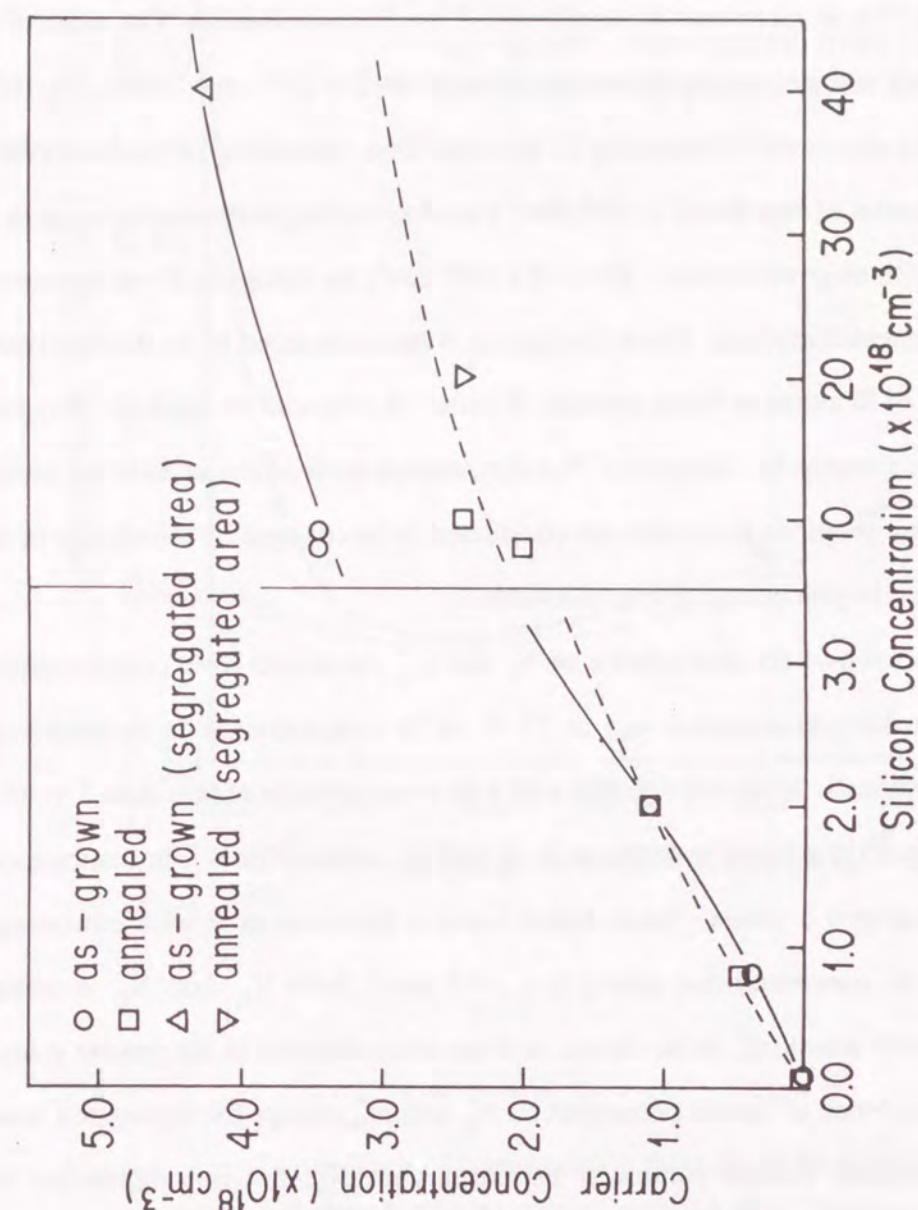


Fig. 6-3 Dependence of carrier concentration on Si concentration in as-grown and annealed GaAs crystals with As atom fractions of 0.5015 in the melt.



above  $2 \times 10^{18} \text{ cm}^{-3}$ , it was smaller than the carrier concentration of as-grown samples. As a result, the ratio of carrier concentration to Si concentration approaches 1/5 - 1/10 at high Si concentration range.

Figure 6-4 shows the dependency of  $\theta$ , which can be calculated from Hall measurement at 77 K as mentioned in section 4-2-2, on Si concentration. The value of  $\theta$  decreases abruptly with decreasing Si concentration below  $2 \times 10^{18} \text{ cm}^{-3}$ . Above  $2 \times 10^{18} \text{ cm}^{-3}$ ,  $\theta$  increases slowly with increasing Si concentration. Annealing of GaAs crystals with Si concentration of less than  $2 \times 10^{18} \text{ cm}^{-3}$  was observed to produce a decrease in  $\theta$  in comparison with as-grown crystal. Above  $2 \times 10^{18} \text{ cm}^{-3}$ , no change in  $\theta$  was observed in the case of annealed crystals. These changes in  $\theta$  are considered to be derived from occupation sites of Si atoms in GaAs crystals. Whether Si atoms sit on Ga-sites ( $\text{Si}_{\text{Ga}}$ ) or As-sites ( $\text{Si}_{\text{As}}$ ) is a matter for discussion. The distribution of Si atoms at different kinds of crystallographic positions in crystals are considered to be changed by the change of Si concentration and the processing of heat treatment.

Figure 6-5 shows the dependence of  $N_{\text{A}}^{-}$  and  $N_{\text{D}}^{+}$  calculated from compensation ratio ( $\theta$ ) and carrier concentration ( $n_{\text{c}}$ ) at 77 K on Si concentration in as-grown or annealed GaAs crystals. Annealed crystals with a Si concentration of less than  $2 \times 10^{18} \text{ cm}^{-3}$  were observed to achieve a decrease in  $N_{\text{A}}^{-}$  and an increase in  $N_{\text{D}}^{+}$  in comparison with that of as-grown crystals. These trend cause a decrease in  $\theta$  with annealing. Otherwise, for Si concentrations above  $8 \times 10^{18} \text{ cm}^{-3}$ , both  $N_{\text{A}}^{-}$  and  $N_{\text{D}}^{+}$  decrease simultaneously with annealing, so no change in  $\theta$  has been observed in the present study.

The dependence of lattice parameter on  $N_{\text{A}}^{-}$  and  $N_{\text{D}}^{+}$  except for segregated area was also investigated. Lattice parameter increases with  $N_{\text{A}}^{-}$ , but is independent of annealing, as shown in Fig. 6-6. Minimum of the lattice parameter is at  $N_{\text{D}}^{+}$  of  $1 \times 10^{18} \text{ cm}^{-3}$  and that becomes constant when  $N_{\text{D}}^{+}$  reaches above about  $2 \times 10^{18} \text{ cm}^{-3}$ , as shown in Fig. 6-7. From these results, it seems that the increase of lattice parameter with that of Si concentration is related to the increase in  $N_{\text{A}}^{-}$ . This change in  $N_{\text{A}}^{-}$  is considered to be mainly due to that of the amount of  $\text{Si}_{\text{As}}$ .

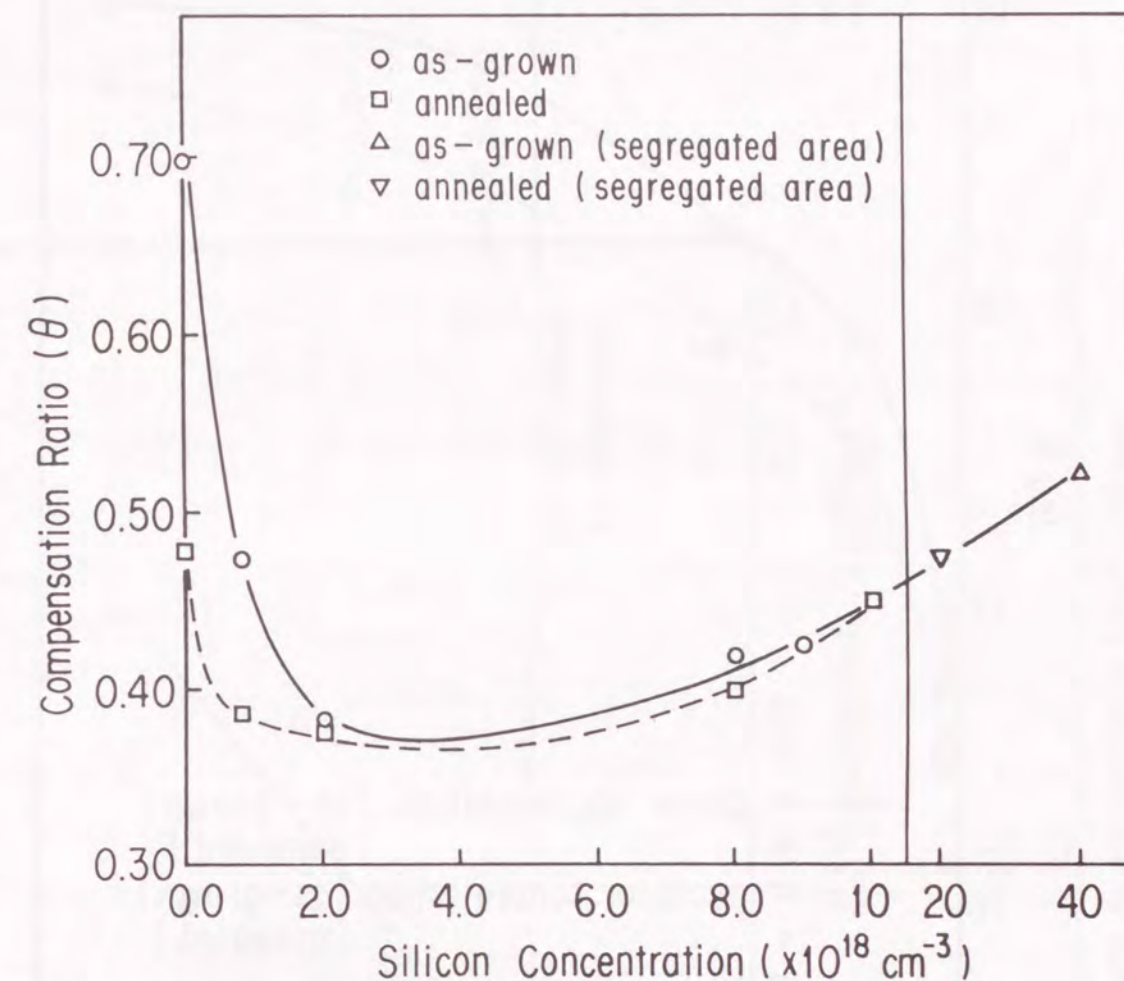


Fig. 6-4 Dependence of compensation ratio ( $\theta$ ) on Si concentration in as-grown and annealed GaAs crystals with As atom fractions of 0.5015 in the melt.



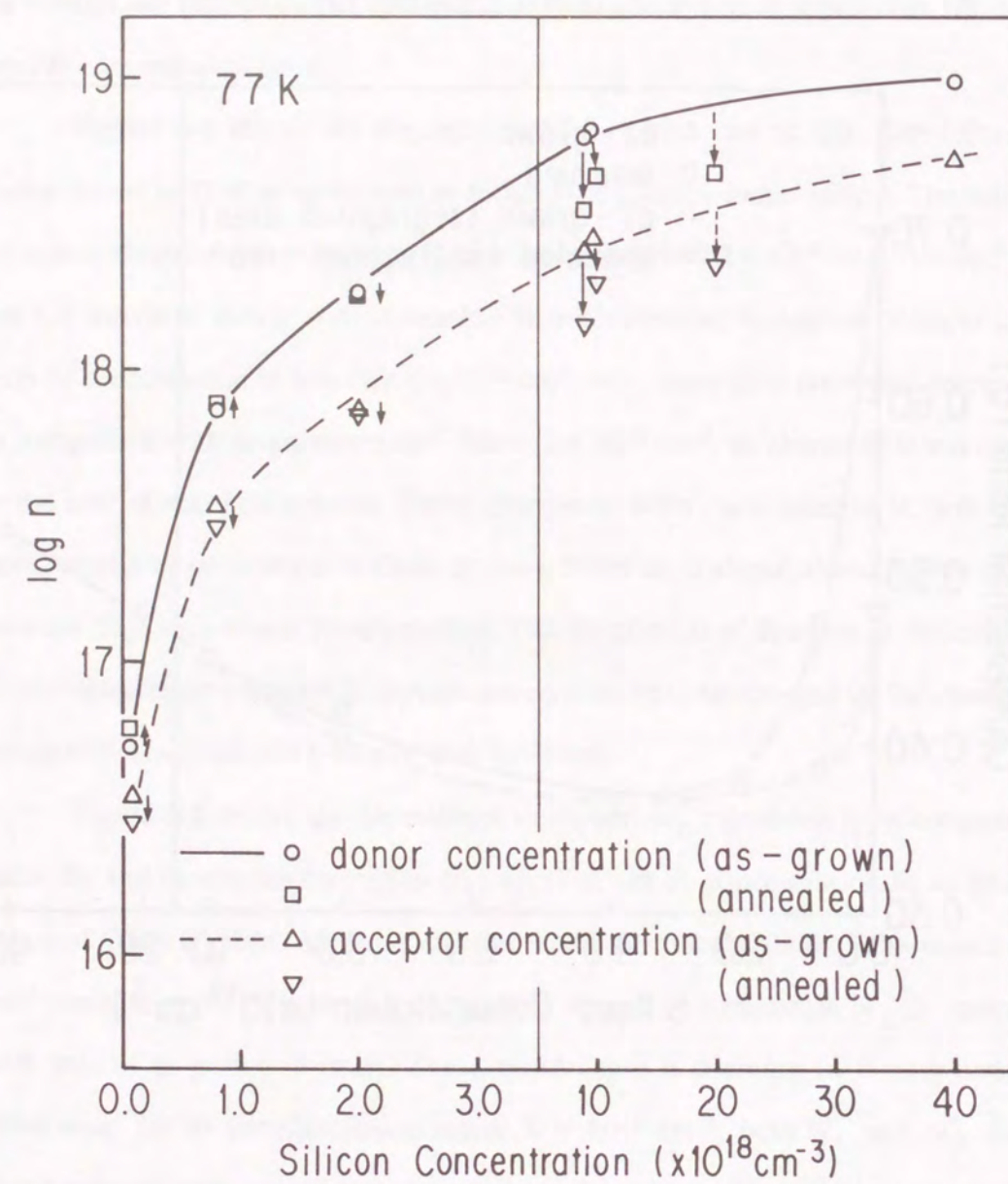


Fig. 6-5 Dependence of acceptor concentration and donor concentration on Si concentration in as-grown and annealed GaAs crystals with As atom fractions of 0.5015 in the melt.

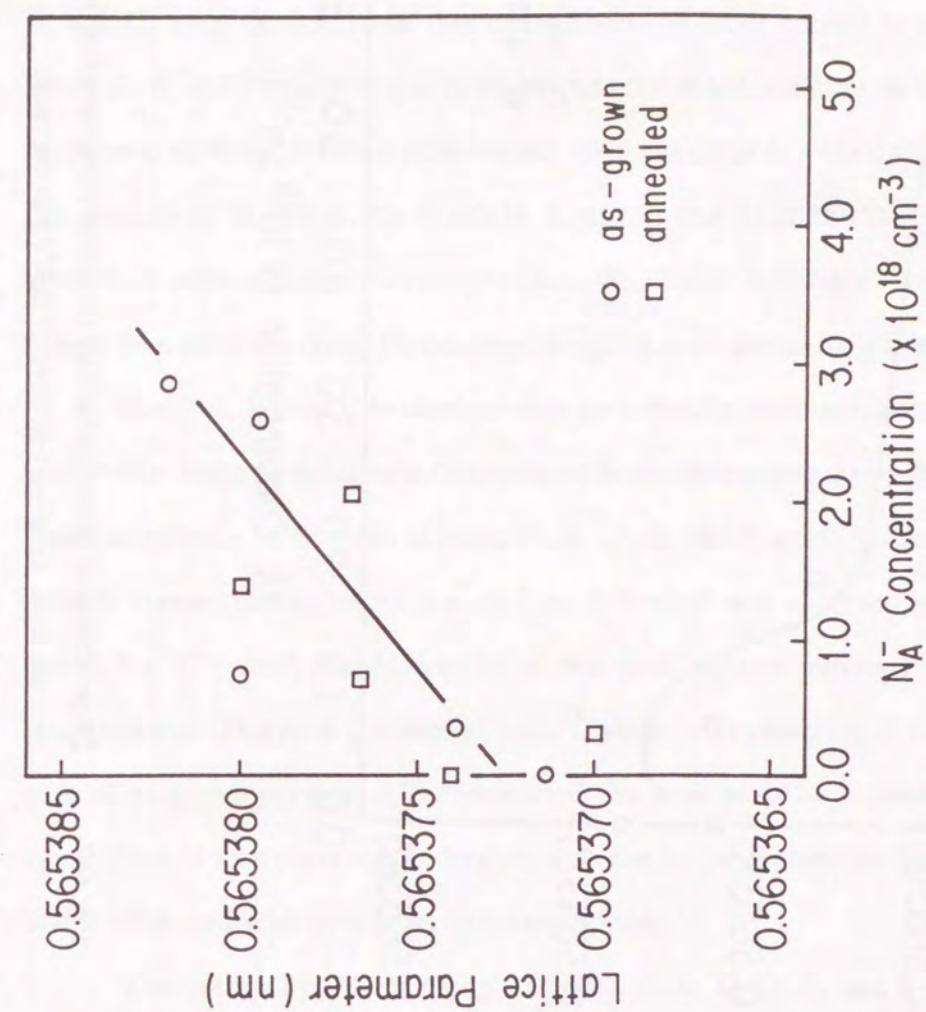


Fig. 6-6 Dependence of lattice parameter on acceptor concentration in GaAs crystals with As atom fractions of 0.5015 in the melt.



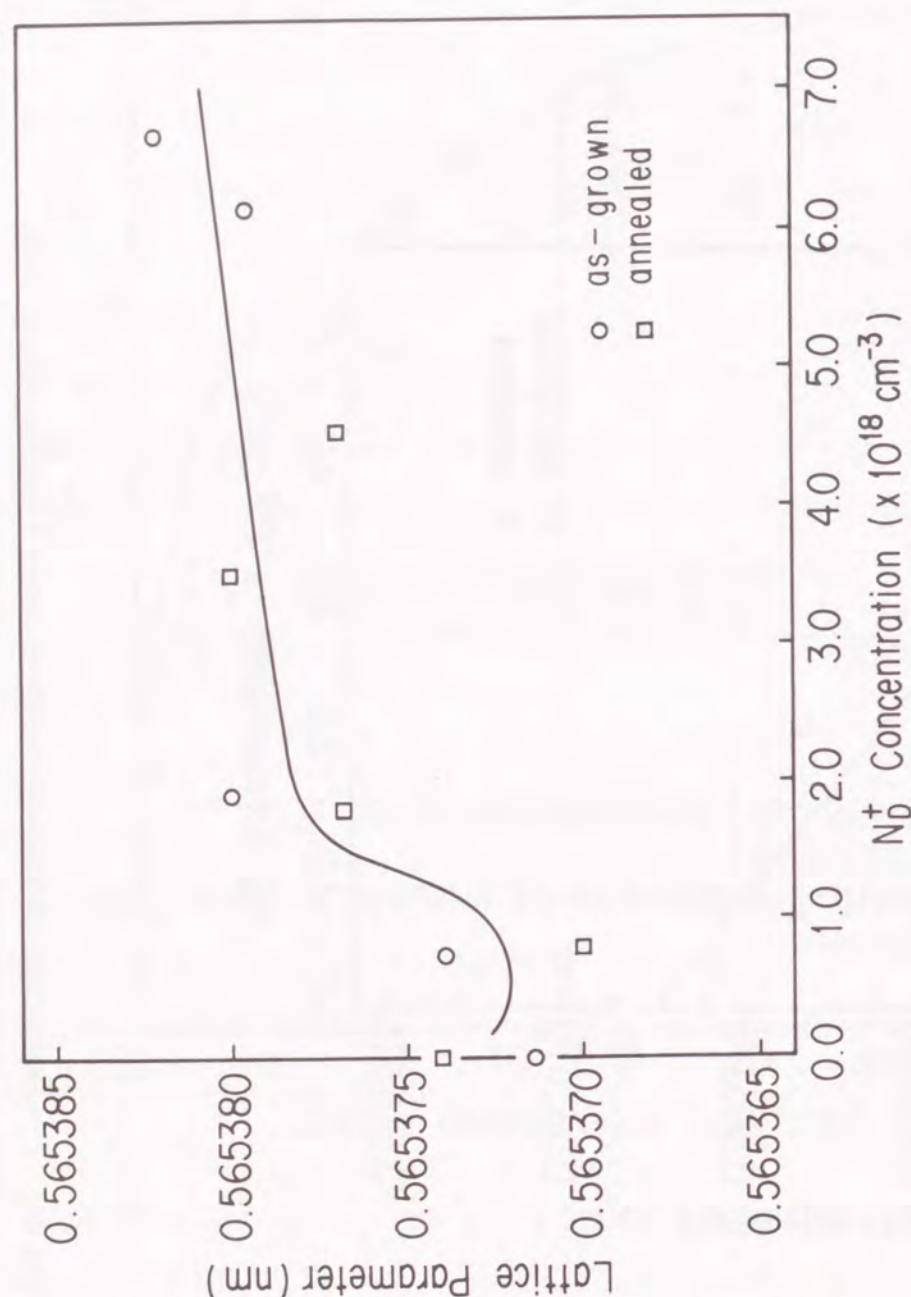


Fig. 6-7 Dependence of lattice parameter on donor concentration in GaAs crystals with As atom fractions of 0.5015 in the melt.

### 6-3-3. Photoluminescence

The PL spectra of as-grown and annealed GaAs crystals are shown in Figs. 6-8 and 6-9, respectively, where PL peaks are denoted by A through H. The peak wavelength of peak H may be longer than 1200 nm. After annealing, those crystals were observed to produce increase in peak height, except for peaks D, E, and F. The origin of these peaks has been clarified by Suezawa et al. [75,76]. Sharp peaks near the band edge (peaks A, B, and C) were thought to be due to the bound excitons related to residual impurities. Peaks D, E, and F might be due to emissions related to Cu sitting on Ga-sites ( $\text{Cu}_{\text{Ga}}$ ) and its phonon replicas. A broad peak around 1040 nm (peak G) was thought to be related to the clusters of Si atoms, for example, a pair of one Si atom sitting on a Ga-site and another Si atom sitting on an As-site ( $\text{Si}_{\text{Ga}}\text{-Si}_{\text{As}}$  pair). A broad PL peak at the range of longer than 1200 nm (peak H) has been assigned to be due to  $\text{Si}_{\text{Ga}}\text{-Si}_{\text{As}}$  pairs.

Peaks A, B, and C become weaker and broader with increasing Si concentration. Eventually, these peaks almost disappear at Si concentrations above  $2 \times 10^{19} \text{ cm}^{-3}$  where small assemblies of Si seem to exist. Peaks D, E, and F were observed only in crystals with Si concentrations below  $1 \times 10^{17} \text{ cm}^{-3}$ . Peak G was observed in crystals with that above  $5 \times 10^{17} \text{ cm}^{-3}$ , and half width of this peak became narrower with increasing Si concentration. The peak position of peak G shifts with changing Si concentration in the case of as-grown crystals. After annealing, the peak position of peak G is virtually the same. Peak H was observed in crystals with the Si concentrations below  $2 \times 10^{18} \text{ cm}^{-3}$ , and it weakened with increasing Si concentration.

The decreasing PL intensity of peaks A, B, C, D, E, and F with increasing Si concentration is thought to be related to the increase of carrier concentration. The behavior of Si in GaAs is assumed to be clarified from the changing of Si-related peaks G and H. The defect of  $\text{Si}_{\text{Ga}}\text{-Si}_{\text{As}}$  pairs is assumed to exist in GaAs crystals with the Si concentrations below  $1 \times 10^{17} \text{ cm}^{-3}$ . Both  $\text{Si}_{\text{Ga}}\text{-Si}_{\text{As}}$  pair and Si-cluster defects are thought to exist in crystals with the Si concentrations between  $1 \times 10^{17} \text{ cm}^{-3}$  and  $2 \times 10^{18} \text{ cm}^{-3}$ . Si-clusters may be dominant in the crystals with Si concentrations above  $2 \times 10^{18} \text{ cm}^{-3}$ . The size of these Si-clusters in the crystals is thought to be smaller than the



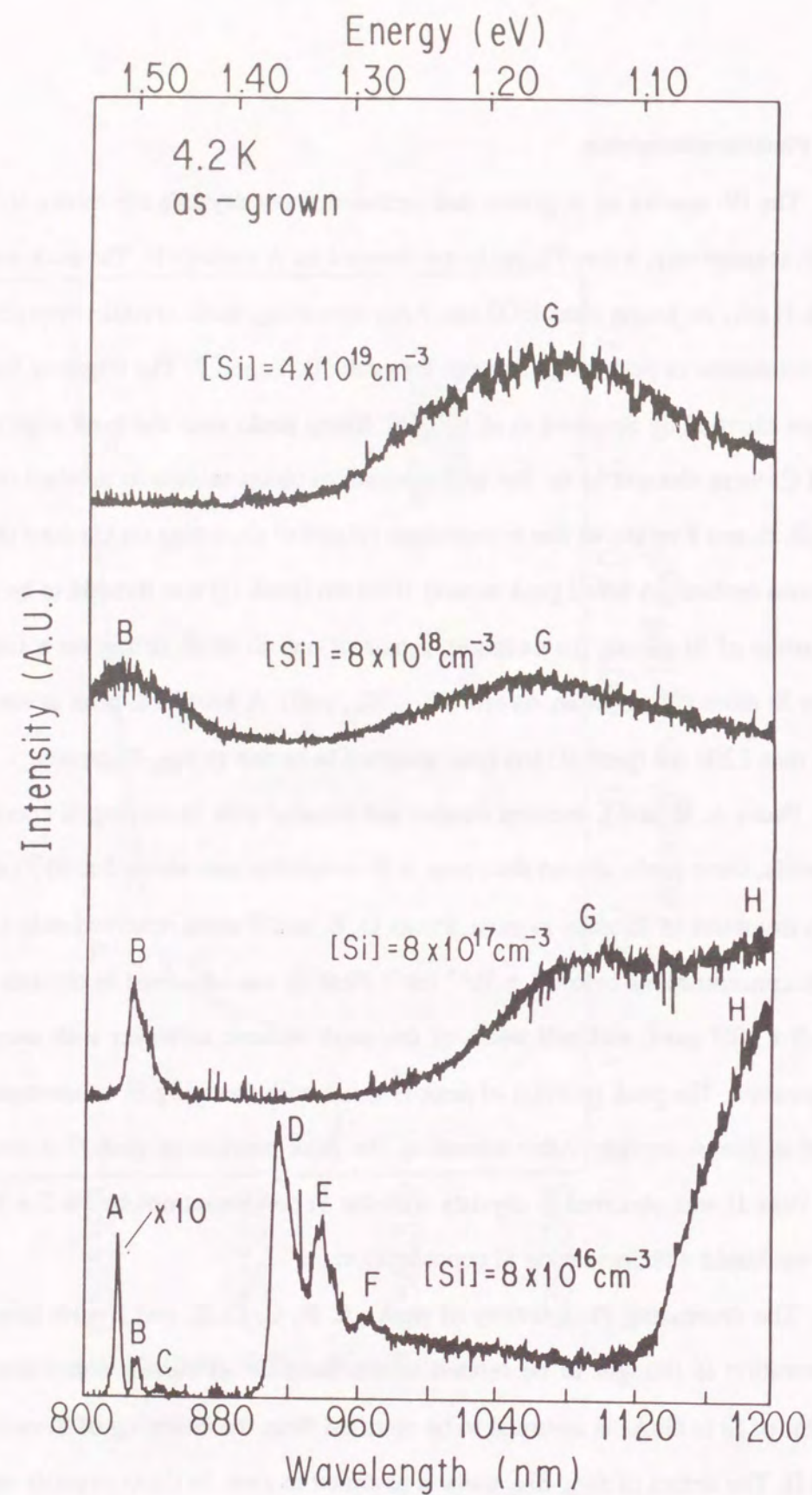


Fig. 6-8 PL spectra of as-grown GaAs crystals with As atom fractions of 0.5015 in the melt.

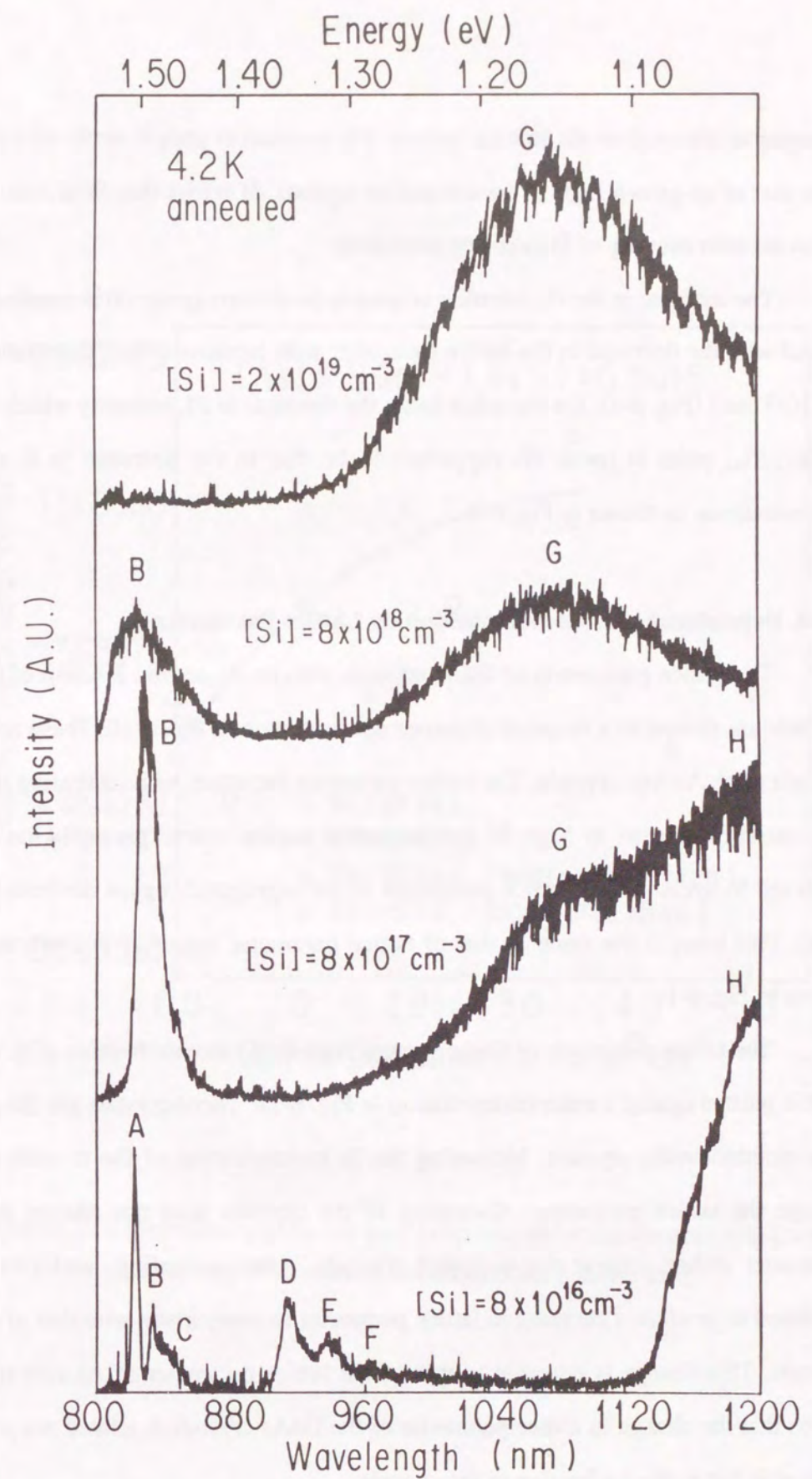


Fig. 6-9 PL spectra of annealed GaAs crystals with As atom fractions of 0.5015 in the melt.



segregation observed on the etching pattern. The position of peak G shifts after annealing from that of as-grown high Si concentration crystals. It seems that Si-clusters become stabilized after moving of Si atoms by annealing.

The increase in the PL intensity related to Si-clusters (peak G) is considered to be related with the decrease in the lattice parameter with increasing Si concentration above  $8 \times 10^{18} \text{ cm}^{-3}$  (Fig. 6-1). On the other hand, the decrease in PL intensity which is related to  $\text{Si}_{\text{Ga}}\text{-Si}_{\text{As}}$  pairs is (peak H) supported to be due to the decrease in  $\theta$  at low Si concentrations, as shown in Fig. 6-4.

#### 6-3-4. Dependence of Melt Composition on Lattice Parameter

The lattice parameters of GaAs crystals with an As atomic fraction of 0.5015 in the melt are plotted as a function of carrier concentration in Fig. 6-10. These crystals are thought to be As-rich crystals. The lattice parameter increases with increasing the carrier concentration except in high Si concentration region where precipitation effect is observed by etching. The lattice parameter of the segregated region deviates from this trend. This trend is the same as that of lattice parameter versus Si concentration plots shown in Fig. 6-1.

The lattice parameter of GaAs crystals with an As atomic fraction of 0.500 in the melt is plotted against carrier concentration in Fig. 6-11. These crystals are thought to be near-stoichiometric crystals. Increasing the Si concentration of the crystals does not change the lattice parameter. Annealing of the crystals does not change the lattice parameter either, except for undoped crystals. After annealing, undoped crystals exhibited to produce a decrease in lattice parameter in comparison with that of as-grown crystals. This change is opposite to that of the lattice parameter of As-rich crystals. It seems that the change in lattice parameter of the GaAs crystals is related not only to the sites of Si but to the As fraction in the crystals.

In LEC undoped GaAs, no correlation of lattice parameter with the stoichiometry in crystals has been reported [77,78]. Similarly, in GF undoped as-grown crystals, no correlation of lattice parameter with stoichiometry in crystals is exhibited. On the other

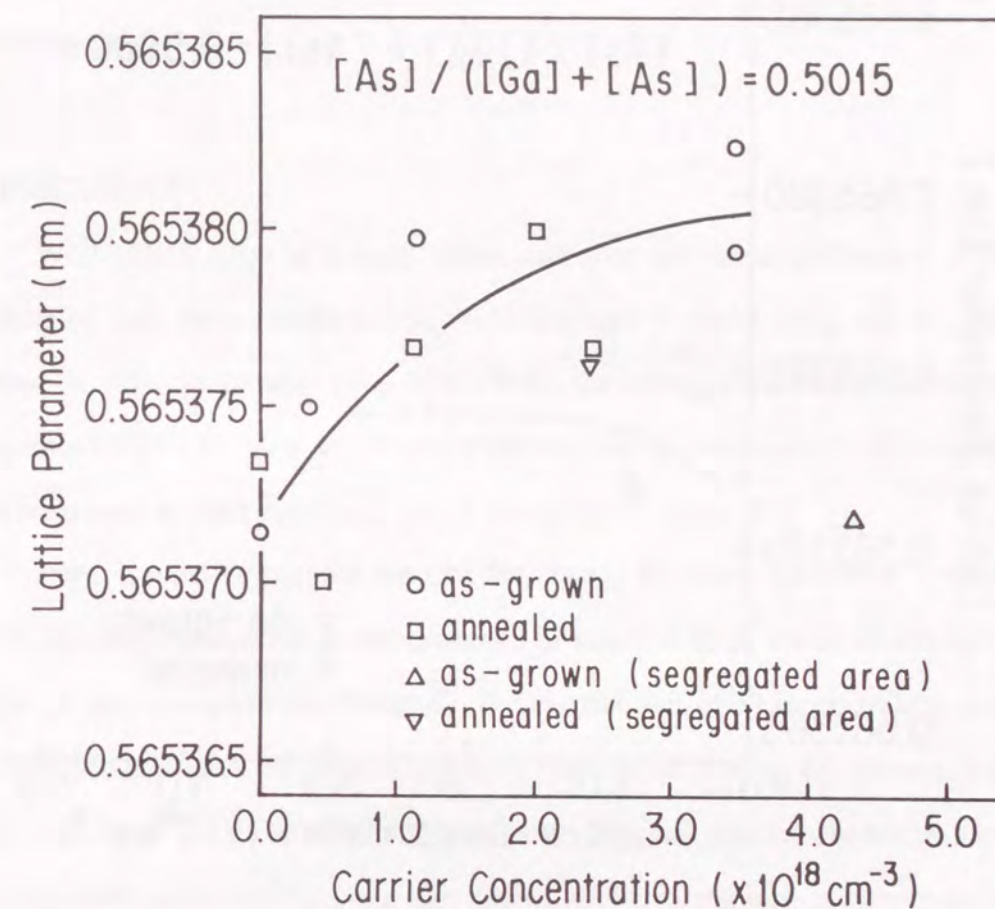


Fig. 6-10 Dependence of lattice parameter on carrier concentration in GaAs crystals with As atom fractions of 0.5015 in the melt.



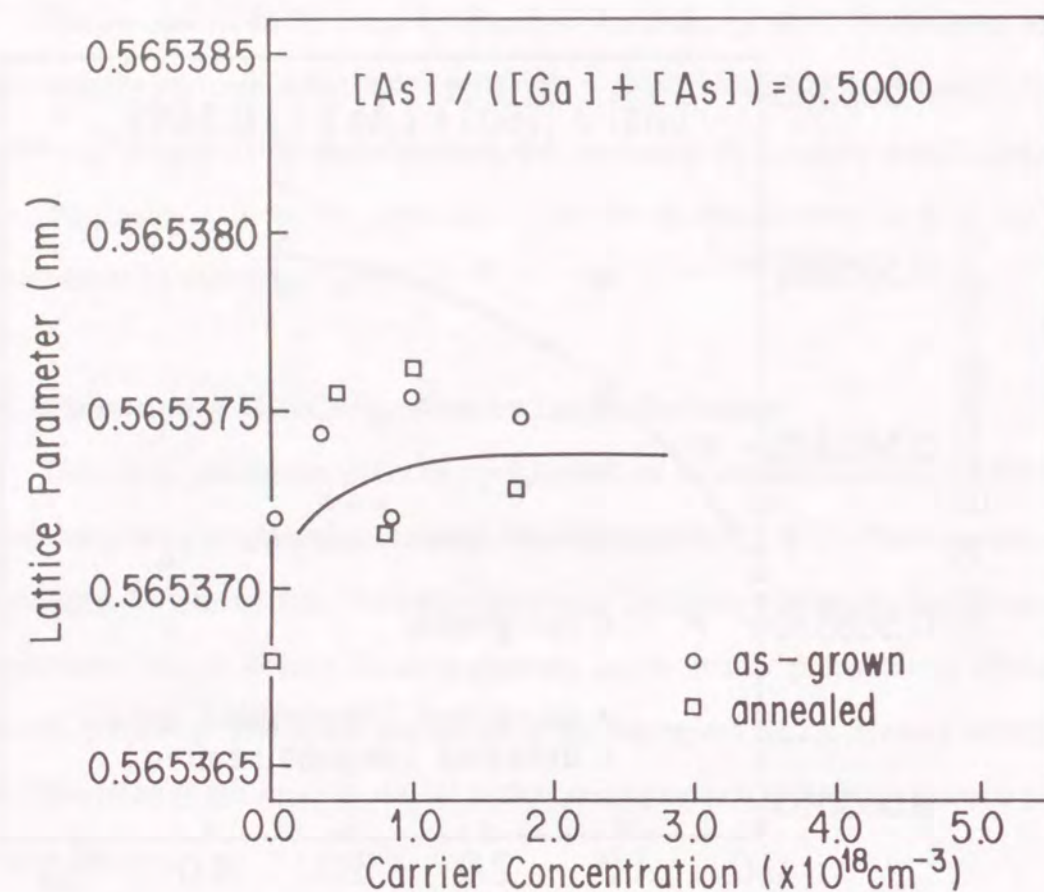


Fig. 6-11 Dependence of lattice parameter on carrier concentration in GaAs crystals with As atom fractions of 0.5000 in the melt.

hand, boron concentration due to the use of  $\text{B}_2\text{O}_3$  in the growth of LEC undoped crystals was reported to relate to the effect of  $V_{\text{As}}$  [79]. From this report, the change in lattice parameter of crystals with intentionally doped impurities has been considered to be the effect of the existence of native defects, especially As-related defects such as  $V_{\text{As}}$  and As interstitials ( $\text{As}_\text{I}$ ).

#### 6-4. DISCUSSION

Well talked sizes of dopant atoms and ions are listed in Table 6-1 [80-82]. Considering only these covalent radii, both kinds of Si atoms ( $\text{Si}_{\text{Ga}}$  and  $\text{Si}_{\text{As}}$ ) cause a decrease in lattice parameter [81]. If one talks the ionic radii into consideration,  $\text{Si}_{\text{Ga}}^+$  atoms must cause a decrease in lattice parameter, and  $\text{Si}_{\text{As}}^-$  atoms cause an increase [81]. It has been reported that even  $\text{Si}_{\text{Ga}}^+$  caused expansion of lattice [82].

Here, it must be pointed out that the change in lattice parameter is related not only to Si concentration but to the existence of native defects which is affected by the change of melt composition. Certainly, the distribution of Si in crystals is not to be simple, if one considers the present results of compensation ratio, PL measurement, and TEM observation [34]. The relationship between Si concentration and lattice parameter of the crystals can be classified into four ranges of Si concentration as mentioned before. A defect model for each group is considered below.

First, for Si concentrations of below  $1 \times 10^{17} \text{ cm}^{-3}$ , the form in which Si exists in crystals is supposed to be  $\text{Si}_{\text{Ga}}$ ,  $\text{Si}_{\text{As}}$  and  $\text{Si}_{\text{Ga}}\text{-Si}_{\text{As}}$  pairs. The dominant defects in the as-grown crystals are considered to be excess  $V_{\text{As}}$  and excess  $\text{As}_\text{I}$  induced during the process of crystal growth. The lattice parameter is thought to be affected by defects at normal lattice sites rather than interstitial defects. In addition, the defect concentrations of as-grown crystals are supposed to be the same as that of the equilibrium state at the growth temperature and may change to the equilibrium concentration at the annealing temperature. In this case, the lattice parameter may be affected by the existence of  $V_{\text{As}}$  more than by that of  $\text{As}_\text{I}$ . The  $V_{\text{As}}$  density in as-grown crystals affected by stoichiometry



Table 6-1

Predicted radii ( $R$ ) for Ga, As, and Si on the basis of different chemical models.  $R$  represents radius of atom (ion),  $\Delta r$  represents the difference in radii between atom (ion) and host atom (ion) in dictated by the subscript,  $a$  represents lattice parameter,  $\Delta a$  represents the amount of change in lattice parameter,  $N_i$  represents impurity concentration in crystal and  $\beta$  represents the strain parameter of a charge-dependent ionic model.

	Covalent Model		Ionic Model		$\beta$
	$R$ (nm)	$\Delta r$ (nm)	$R$ (nm)	$\Delta r$ (nm)	$(\frac{\Delta a}{a} = \beta \cdot N_i)$
Ga	1.24	—	0.64	—	—
As	1.21	—	1.81	—	—
Si <sub>Ga</sub>	1.17	-0.07	0.40	-0.24	+0.97
Si <sub>As</sub>	1.17	-0.04	1.95	+0.14	—

may have small effect to lattice parameter because the change of  $V_{As}$  density is not so large enough. Annealing of these crystals probably cause a reaction between excess  $V_{As}$  and excess  $As_I$ , and which reaction is thought to change the lattice parameter. Annealing of the As-rich crystals is thought to cause a decrease in  $V_{As}$  and an increase in lattice parameter. If the annealing of near stoichiometric crystals brings the increase of the number density of  $V_{As}$  in those crystals, and a decrease of lattice parameter.

Next, in the range of Si concentrations between  $1 \times 10^{17} \text{ cm}^{-3}$  and  $2 \times 10^{18} \text{ cm}^{-3}$ , the sites on which a Si atom exists in crystal are assumed to be in the  $Si_{Ga}$ ,  $Si_{As}$ ,  $Si_{Ga}-Si_{As}$  pairs,  $Si_{As}-As_I$  complexes and smaller Si-clusters. The lattice parameter of As-rich crystals increases with increasing Si concentration, as shown in Fig. 6-6. From this result, the dominant defects in these crystals are assumed to be  $Si_{As}-As_I$  complexes, which may cause an increase in lattice parameter of As-rich crystals. It is thought that annealing of As-rich crystals causes a decomposition of  $Si_{As}-As_I$  complexes, i.e.,  $Si_{As}$  atom parts from  $As_I$  and form an isolated Si interstitials ( $Si_I$ ) and  $V_{As}$ . Then the  $V_{As}$  is occupied by  $As_I$ , and finally a Ga atom on the normal position is substituted by the  $Si_I$  atom. These reactions may cause a decrease of lattice parameter, a decrease of acceptor concentration, and an increase of donor concentration. In near-stoichiometric crystals, the number density of  $Si_{As}-As_I$  complexes is thought to be negligibly small because of the small concentration of  $As_I$ . This may be the reason why the lattice parameter changes with changing the Si concentration.

In the range of Si concentrations between  $2 \times 10^{18} \text{ cm}^{-3}$  and  $8 \times 10^{18} \text{ cm}^{-3}$ , Si atoms exist in crystals are supposed to be in the forms,  $Si_{Ga}$ ,  $Si_{As}$ ,  $Si_{Ga}-Si_{As}$  pairs,  $Si_{As}-As_I$  complexes, and Si-clusters. The dominant defects in these crystals may be  $Si_{As}-As_I$  complexes and Si-clusters. It is considered that Si-clusters increase their density and to grow into larger sized clusters by the aggregation of  $Si_{Ga}$ ,  $Si_{As}$ , and  $Si_I$  atoms with increasing Si concentration. Therefore, the lattice parameter is thought to decrease with growing Si-clusters. The change in Si concentration and annealing proceeds exhibited scarcely any change in the lattice parameter of As-rich crystals because the effects of



forming  $\text{Si}_{\text{As}}\text{-As}_\text{I}$  complexes and Si-clusters are supposed at the same time in the present case.

In last stage, the case of Si concentrations above  $8 \times 10^{18} \text{ cm}^{-3}$ , the defects including Si-clusters,  $\text{Si}_{\text{Ga}}$  and  $\text{Si}_{\text{As}}$  may be dominant. Si may simply be incorporated into Ga-sites and As-sites in the mother phase because the presence of plenty of Si-clusters might have gathered excess Si and As. As a result, the lattice parameter simply decreases with increasing Si concentration. Annealed crystal exhibited the decrease in both acceptor and donor concentrations, because the Si-clusters were thought to react with substitutional Si. As the reaction of  $\text{Si}_{\text{Ga}}$  and  $\text{Si}_{\text{As}}$  may occur at the same time, the lattice parameter achieves no change by annealing. The dominant process of this stage will be discussed in chapter 7.

The above results are summarized in Table 6-2.

## 6-5. CONCLUSION

The effect of Si doping on lattice parameter in GaAs crystals grown by the GF method was investigated. The lattice parameter of As-rich crystals changes with changing the Si concentration. The relationship between Si concentration and lattice parameter can be classified into four ranges of Si concentration in which the trend of change in lattice parameter with increasing Si concentration were observed to be: increase, increase, no change, and decrease. Annealing of the crystals caused the change of lattice parameter in each range and those were: increase, decrease, no change, and no change, respectively. The relationship between Si concentration and lattice parameter of stoichiometric crystals is not clear, and the effect of annealing is also not clear too, except in the lowest Si concentration region. Therefore, the lattice parameter of crystals affected by Si exhibits complicated changes. It is summarized that the change in lattice parameter is affected not only by the sites of Si but by native defects in GaAs crystals.

Table 6-2

Summary of the relationship between lattice parameter and Si concentration. The model is for an As ratio of 0.5015 in the melt. In this model,  $\text{Si}_\text{I}$  is assumed to aggregate to Si-clusters.  $\uparrow$  indicates increase,  $\downarrow$  indicates decrease, and  $\rightarrow$  indicates no change.

Region	I	II	III	IV
$[\text{Si}] \text{ (cm}^{-3}\text{)}$	$1 \times 10^{17}$	$2 \times 10^{18}$	$8 \times 10^{18}$	
$[\text{As}] / ([\text{Ga}] + [\text{As}]) = 0.5015$				
Lattice Parameter	$\uparrow$	$\uparrow$	$\uparrow$	$\uparrow$
Donor Concentration	$\uparrow$	$\uparrow$	$\uparrow$	$\uparrow$
Acceptor Concentration	$\uparrow$	$\uparrow$	$\downarrow$	$\downarrow$
Photoluminescence	$\uparrow$	$\uparrow$	$\downarrow$	$\downarrow$
	$\text{Si}_{\text{Ga}} - \text{Si}_{\text{As}}$	$\text{Si}_{\text{Ga}} - \text{Si}_{\text{As}} + \text{Si-Cluster}$		Si-Cluster
$[\text{As}] / ([\text{Ga}] + [\text{As}]) = 0.5000$				
Lattice Parameter	$\uparrow$	$\uparrow$	$\uparrow$	$\uparrow$
Annealing	$\uparrow$	$\uparrow$	$\uparrow$	$\uparrow$
Model : $[\text{As}] / ([\text{Ga}] + [\text{As}]) = 0.5015$				
$[\text{Si}] \uparrow$	$\uparrow$	$\uparrow$	$\uparrow$	$\uparrow$
Annealing	$\downarrow$	$\downarrow$	$\downarrow$	$\downarrow$
	$[\text{V}_{\text{As}}]$	$[\text{Si}_{\text{As}} - \text{As}_\text{I}] \uparrow$	$[\text{Si}_{\text{As}} - \text{As}_\text{I}] \uparrow$	Si-Cluster $\uparrow$
	$[\text{As}_\text{I}] \uparrow$		Si-Cluster $\uparrow$	$[\text{Si}_{\text{Ga}}], [\text{Si}_{\text{As}}] \uparrow$
	$\text{As}_\text{I} + \text{V}_{\text{As}} \rightarrow \text{As}_{\text{As}}$	$\text{Si}_{\text{As}} \rightarrow \text{Si}_\text{I} + \text{V}_{\text{As}}$	Region II and IV	$\text{Si}_{\text{As}} \rightleftharpoons \text{Si}_\text{I}$
		$\text{Si}_\text{I} + \text{V}_{\text{Ga}} \rightarrow \text{Si}_{\text{Ga}}$		$\text{Si}_{\text{Ga}} \rightleftharpoons \text{Si}_\text{I}$
		$\text{V}_{\text{As}} + \text{As}_\text{I} \rightarrow \text{As}_{\text{As}}$		
				$\uparrow$ Increase
				$\downarrow$ Decrease
				$\rightarrow$ No change



## **7. DEFECT REACTIONS BY HEAT TREATMENT OF HEAVILY SILICON DOPED GALLIUM ARSENIDE**

### **7-1. INTRODUCTION**

An important point in the production of the substrate for epitaxial growth is the change of the crystal characteristics by annealing. There have been number of studies of annealing-induced effects on the properties of Si-doped GaAs. Chen and Spitzer [66] reported that carrier concentration, infrared absorption due to the defect-induced localized vibrational mode (LVM), micro structure observed by TEM, and critical resolve shear stress of Si-doped GaAs reveal temperature-dependent annealing-induced changes in several specific defect concentrations. The effect of heat treatment on PL spectra of Si-doped GaAs was investigated by Suezawa et al. [75]. According to these reports, Si-related defects affect the characteristics of Si-doped GaAs.

Si-related segregation seems to be generated when the Si concentration increases above  $8 \times 10^{18} \text{ cm}^{-3}$ , as discussed in chapter 6. This segregation is due to large extrinsic stacking faults and small dislocation loops, as determined by TEM [66]. The structure of these two types of segregation was determined to be planer defects lying on adjacent two {111} net planes of Si atoms [83].

In this chapter, the behavior of defects in heat-treated heavily Si-doped GaAs is discussed. Isothermal annealing produces a change in the distribution of Si-related segregation, as shown by etching and XRT. Similar changes in lattice parameter, carrier concentration, and Hall mobility in the regions, where segregation was observed, were produced by heat treatment. Defect reactions due to the heat treatment are discussed on the basis of the change in these characteristics.

### **7-2. EXPERIMENTS**

The crystal growth condition was exactly the same as that of chapter 6. Several types of specimens such as as-grown crystals and bulk-annealed crystals after 18

different annealing processing were prepared. They were annealed at the temperatures of 400 °C, 550 °C, 700 °C, 850 °C, 1000°C, or 1150 °C. The heat treatment was done for 20 hr then cooled at 30 °C/h, for 20 hr then quenching, or for 0.5 hr then quenching.

Specimens of {111} orientated wafers of 1 mm thickness were sliced from GaAs ingots grown in the <111> As direction. The concentration of Si in a GaAs ingot increases with increasing the fraction solidified (g) because the segregation coefficient of Si in GaAs is less than unity [1]. The samples, where the g value was over 0.9, were used in order to find the regions of Si-related segregation. There is no Si-related segregation near the free surface of a sliced sample, but near the bottom of the boat such segregation was found. Such segregation is depend on the solidification conditions. The distribution of such segregation is illustrated in Fig. 7-1.

The Si concentration in each sample was measured by SIMS. The value of Si concentration of most crystals distributed between  $5$  and  $8 \times 10^{18} \text{ cm}^{-3}$  near the free surface and between  $1.5$  and  $3 \times 10^{19} \text{ cm}^{-3}$  near the bottom of the boat. The distribution of Si-related segregation was examined on the (111) As surface etched with a solution of  $\text{HNO}_3:\text{HF}:\text{H}_2\text{O} = 3:1:4$  with  $\text{AgNO}_3$  0.3 wt% for about 3 min at room temperature [14]. Micro-sized roughness on the etched surface was observed in the segregation region, as discussed in chapter 6. The (220) reflection of GaAs by  $\text{CuK}\alpha 1$  X-rays and nuclear plates were used for the XRT observations [25]. The lattice parameters of the Si-segregated region were measured by  $\text{CuK}\alpha 1$  radiation at  $25 \pm 1$  °C by using the Bond method [22,77]. For this measurement, polished and etched 10 mm x 10 mm square shaped samples were used. The carrier concentration and Hall mobility were estimated by using the VDP method [26] at 300 K.

### **7-3. RESULTS**

#### **7-3-1. Distribution of Si-Related Segregation**

The change of distribution of Si-related segregation produced by heat treatment was observed by chemical etching [14] and XRT [25]. Figure 7-2 shows typical



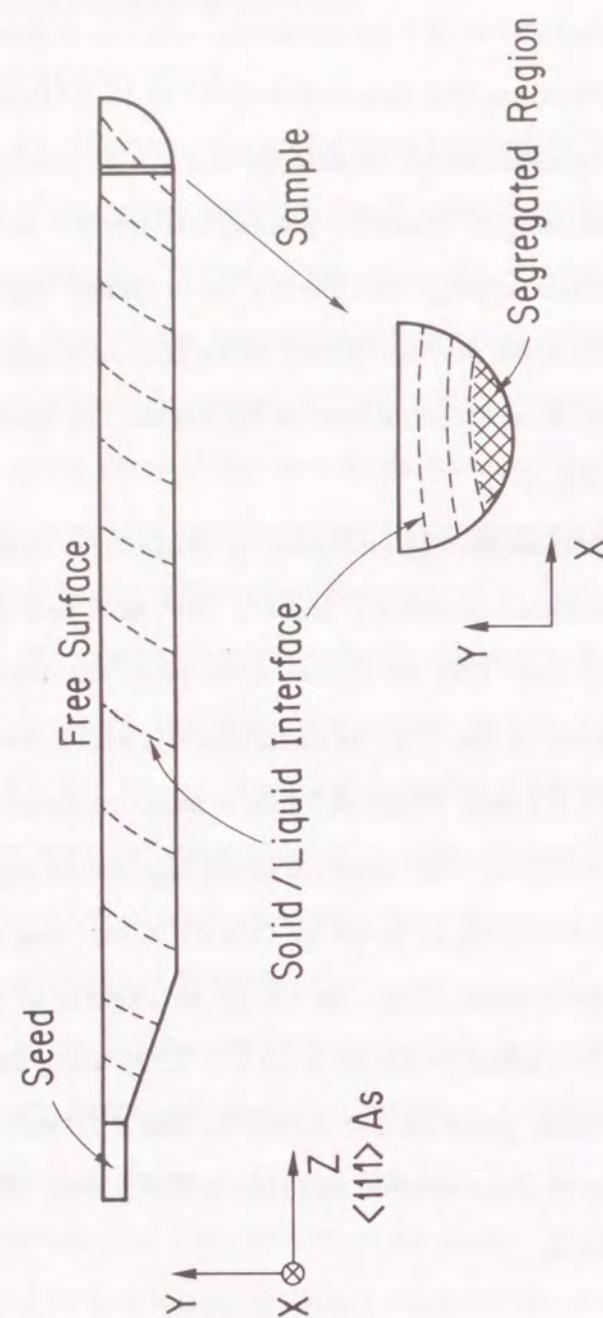


Fig. 7-1 Sketch of solid-liquid interface of solidification in GaAs ingot grown by the GF method, and the sampling positions. Sample {111} wafers are also shown schematically. The hatched region is where Si-related segregation was observed.

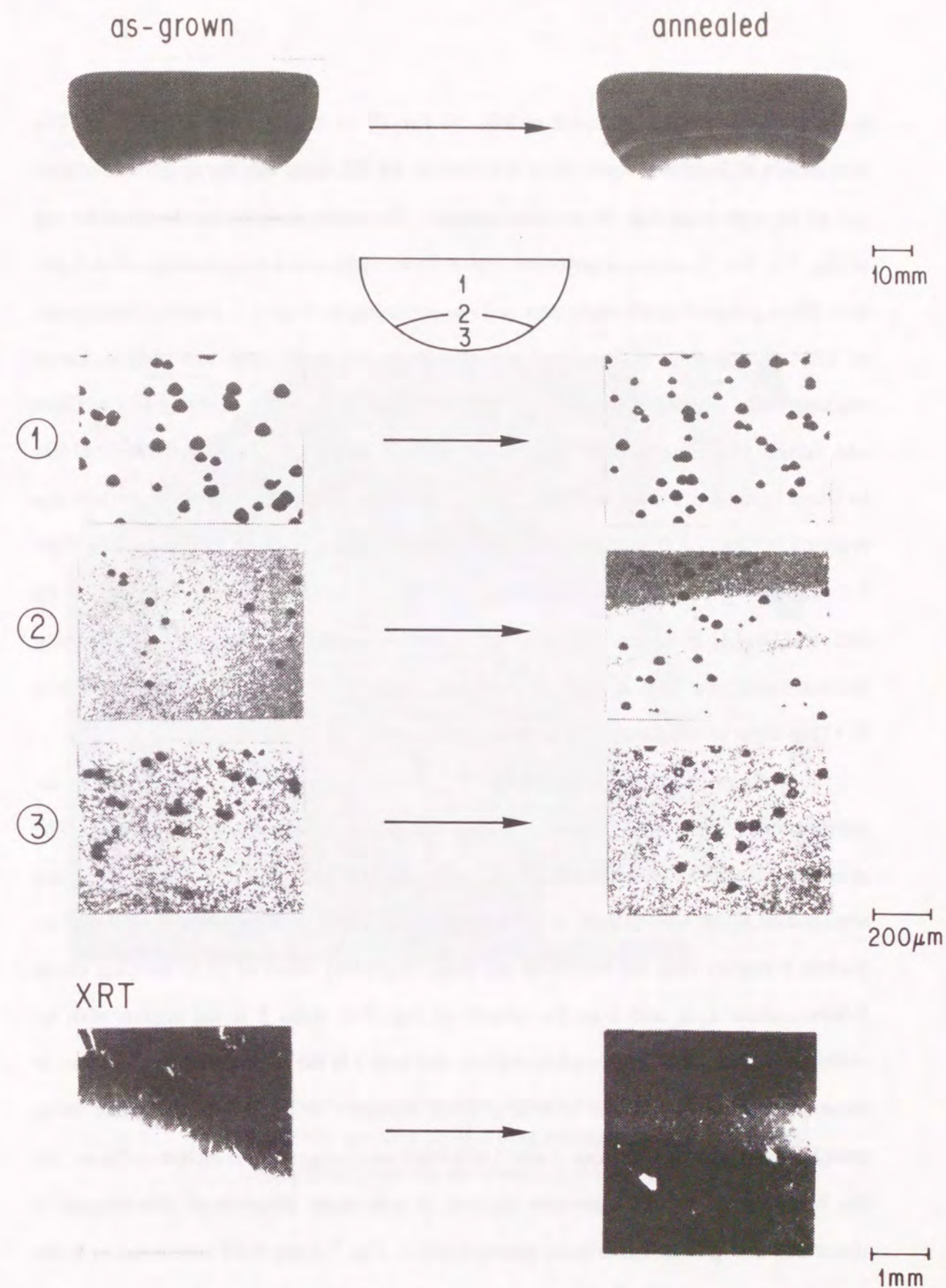


Fig. 7-2 Change in Si-related segregation region observed after heat treatment. The crystals were annealed at 850 °C for 20 hr then cooled at 30 °C/h. This figure shows entire samples, the magnified areas of etched surfaces, and XRT observations.



examples which were annealed at 850 °C for 20 hr then cooled at 30 °C/h. The distribution of Si-related segregation is shown on the left-hand side for as-grown samples and on the right-hand side for annealed samples. The entire samples are shown at the top of Fig. 7-2. The Si-related segregation region looks white and a large number of etch pits look like a group of small white dots in these photographs. Figure 7-3 shows an example of TEM photographs of Si-related segregation region in an as-grown sample. Large stacking faults and small dislocation loops were observed, similar to the results of Chen and Spitzer [63]. High resolution end-on views of large and small loops with  $\langle 110 \rangle$  incident beam are shown in Figs. 7-4 (a) and (b), respectively. Burgers circuits are depicted in Figs. 7-4 (c) and (d), which are magnified images of the framed parts in Figs. 7-4 (a) and (b), respectively. The Burgers vectors of both loops are determined to be  $(a/3) \langle 111 \rangle$  [83]. It is seen in both images that an extra  $\{111\}$  array is inserted, forming the interstitial type loop. A schematic diagram of the crystal structure is thought to be a Si  $\{111\}$  layer inserted in the GaAs matrix as shown in Fig. 7-5 [83].

In the photographs at the top of Fig. 7-2, the Si-related segregation in an as-grown sample can be seen to have an unclear boundary, near the bottom of the boat. The annealed sample can be seen to have a clearly distinguishable region of zone-distributed segregation at the middle part of the sample, and shows the segregated region with an unclear boundary near the bottom of the boat. Magnified views of these samples are as follows: areas 1, 2, and 3 in the middle of Fig. 7-2. Area 1 is the region with no segregation; Area 2 is the boundary region; and area 3 is the region with segregation. In these photographs, etch pits look like black triangles or black circles. When these samples were annealed, regions 1 and 3 exhibited no changes in the etched surfaces, but the boundary of region 2 became clearer. A schematic diagram of this change is illustrated in Fig. 7-6. The bottom photographs in Fig. 7-2 are XRT results taken at the boundary region (region 2). The segregation region appears white in these photographs because of X-ray scattering by the segregation. The results obtained from XRT were the same as that obtained from chemical etching.

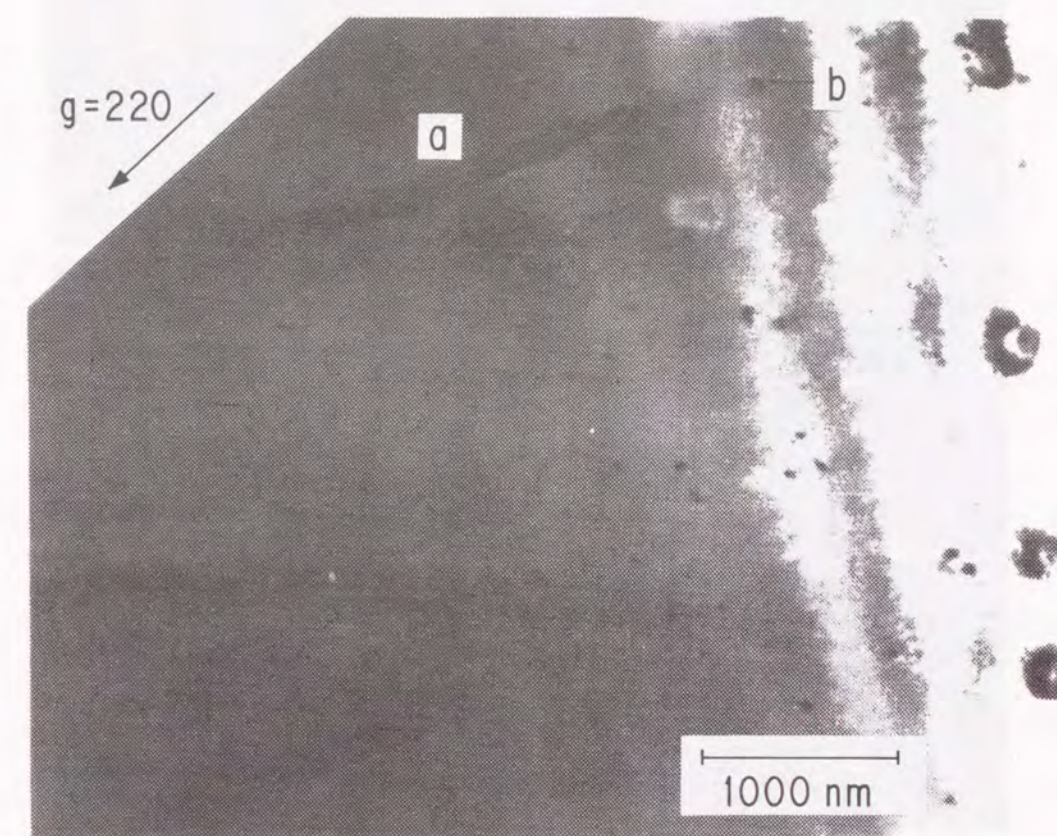


Fig. 7-3 Si-related segregation in as-grown heavily Si-doped crystals, observed by using TEM. Large stacking faults (a) and small dislocation loops (b) are observed in this photograph.



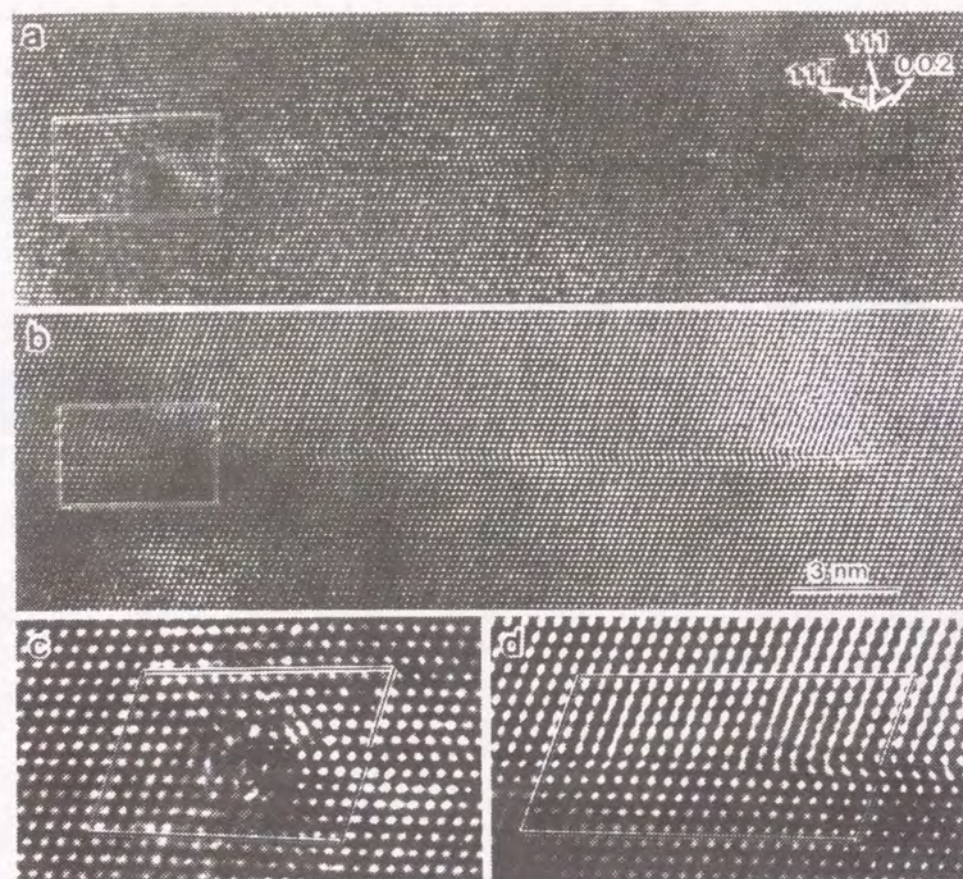


Fig. 7-4 High resolution micrographs of (a) large and (b) small planar defect, with the incident beam parallel to the defect plane. (c) and (d) are the Burgers circuits in the framed areas of (a) and (b), respectively.

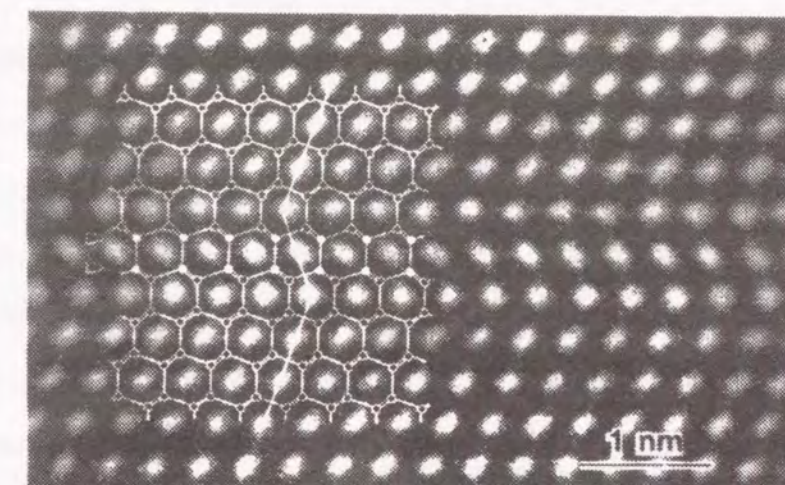
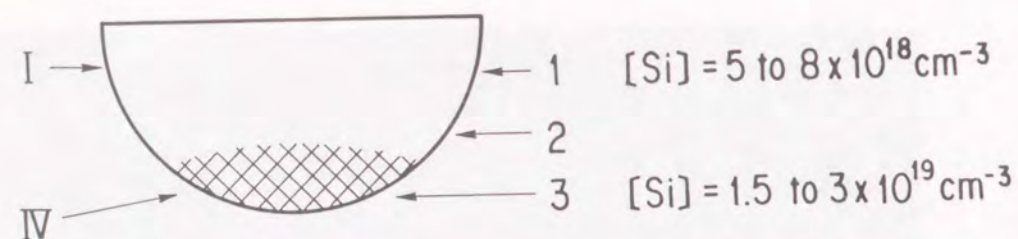


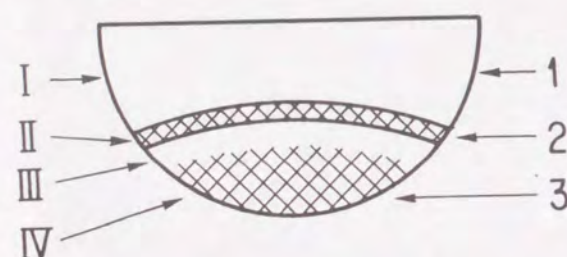
Fig. 7-5 Magnified image of Fig. 7-4 (b), on which the projected atomic possible structure is superimposed. The full circles represent extra atoms (Si atoms?) and the arrow heads indicate the extra plane.



as-grown



annealed



I, III : no segregation  
II, IV : segregated region

Fig. 7-6

Schematic diagram of the change in Si-related segregation region due to heat treatment. No segregation is observed in regions I and III after etching, but segregation is observed in regions II and IV. The hatched regions show where Si-related segregation was observed and the solid lines indicate clear boundaries of the segregation region.

The results of chemical etching tests and XRT observations were carried out. They were annealed at 550 °C, 850 °C, or 1150 °C, for 20 hr then cooled at 30 °C/h, for 20 hr then quenched, or for 0.5 hr then quenched are shown in Figs. 7-7 and 7-8, respectively. The XRT results taken at the boundary region of heat-treated samples were similar to results of chemical etching. The distribution of Si-related segregation varies with changing the conditions of heat treatment. Zone-distributed segregation was observed after annealing at 700 °C, 850 °C, or 1000 °C for 20 hr. This zone-distribution was particularly clear after annealing at 700 °C and 850 °C.

### 7-3-2. Lattice Parameter, Carrier Concentration and Mobility in Si-Related Segregation Region

Figure 7-9 shows the relationship between lattice parameter and Si concentration in GaAs crystals with the Si concentration was above  $8 \times 10^{18} \text{ cm}^{-3}$ . A typical value measured by using SIMS was adopted as the Si concentration of the samples because localized high Si concentrated parts existed in heavily Si-doped GaAs crystals. The lattice parameter of as-grown crystals, which had a Si concentration of  $1.0 \times 10^{19} \text{ cm}^{-3}$ , was estimated to be around 0.565380 nm. The broken line shows the values predicted by Vegard's law calculated from the covalent radii of Si, Ga, and As [80,81], as discussed in chapter 6, and using this estimated initial value. The lattice parameter decreases with increasing Si concentration in the crystals. The reduction rate when the Si concentration was below about  $2.5 \times 10^{19} \text{ cm}^{-3}$  was about 1.6 times larger than the rate predicted by Vegard's law. The lattice parameter with a Si concentration above  $2.5 \times 10^{19} \text{ cm}^{-3}$  was constant at about 0.565360 nm, which is lower than that of undoped GaAs (0.565370 nm : see chapter 6).

The lattice parameter of as-grown GaAs crystals with an Si concentration of above  $8 \times 10^{18} \text{ cm}^{-3}$  was strongly affected by variations of Si concentration. For this reason, the effect of heat treatment was evaluated as a change in lattice parameter, which was defined to be the difference between the lattice parameter of a heat-treated sample and that of the as-grown sample. These two specimens were cut from two parts, next to



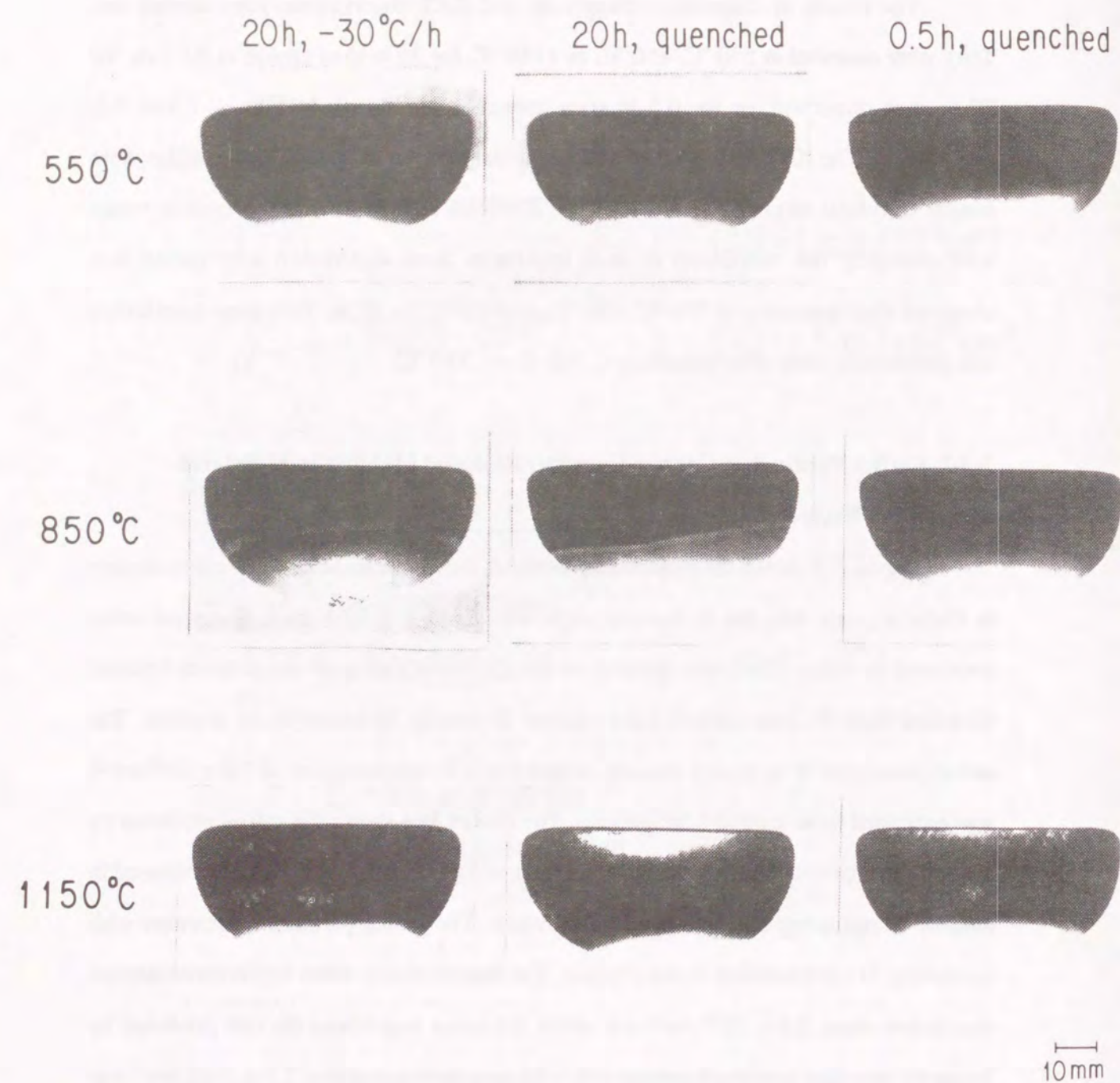


Fig. 7-7 Etched surfaces of nine entire samples. The samples were annealed at 550 °C, 850 °C, or 1150 °C, and for 20 hr then cooled at 30 °C/h, for 20 hr then quenched, and for 0.5 hr then quenched.

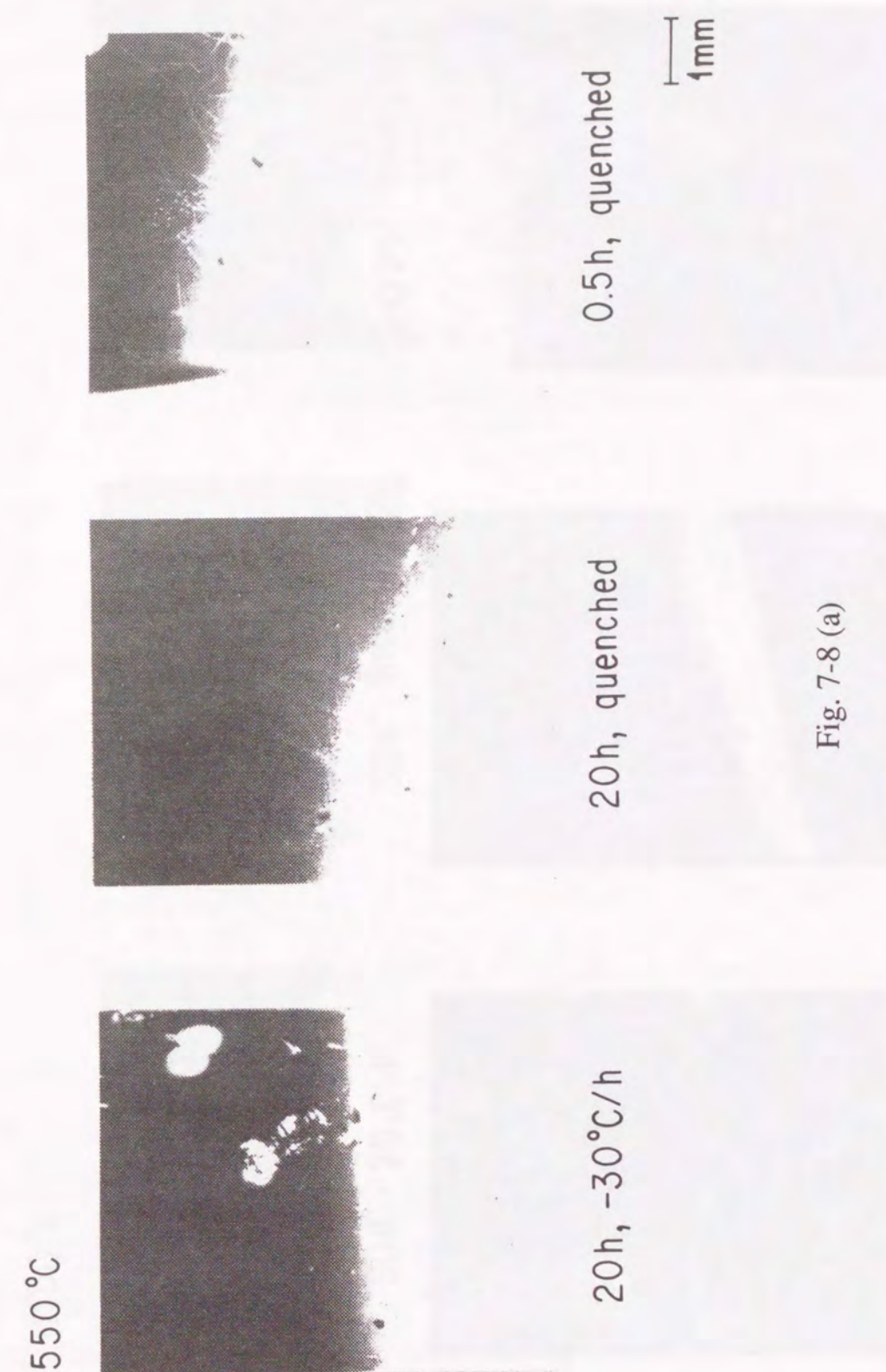
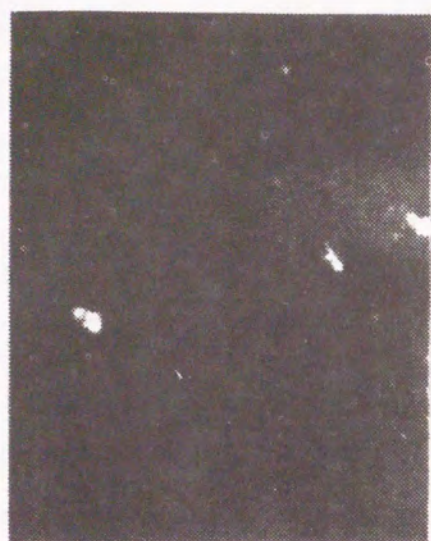


Fig. 7-8 (a)



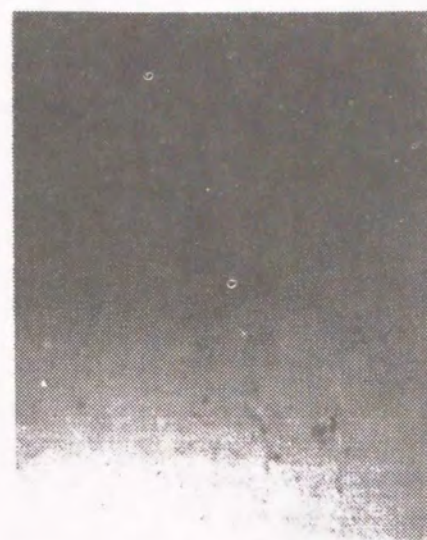
850 °C



20h, -30 °C/h



20h, quenched



0.5h, quenched

1mm

Fig. 7-8 (b)

1150 °C



20h, -30 °C/h



20h, quenched



0.5h, quenched

1mm

Fig. 7-8 (c)

Fig. 7-8 XRT observation of nine entire samples. The samples were annealed at 550 °C (a), 850 °C (b), and 1150 °C (c), for 20 hr then cooled at 30 °C/h, for 20 hr then quenched, and for 0.5 hr then quenched.



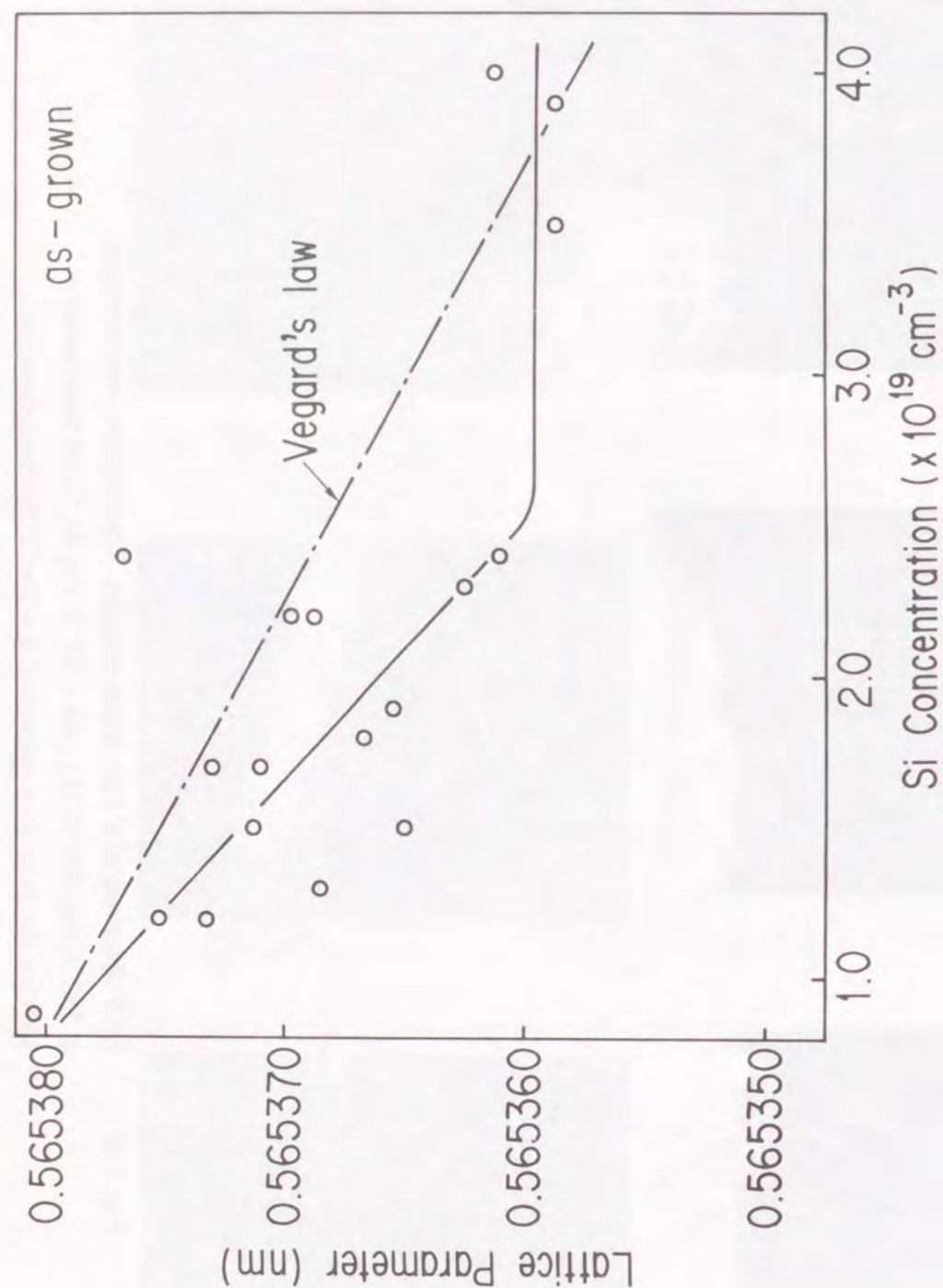


Fig. 7-9 Relationship between lattice parameter and Si concentration in region where as-grown Si-related segregation was observed. The broken line shows the value predicted by Vegard's law using the covalent radius of Si, Ga, and As.

each other in the materials. The effects of heat treatment are shown in Fig. 7-10. In general, annealing below 850 °C decreased the lattice parameter, while annealing above 850 °C either produced no change or increase in lattice parameter. The change in lattice parameter due to heat treatment depend slightly on the annealing process. Crystals which have been annealed for 0.5 hr then quenched are supposed not to have reached the equilibrium state at annealing temperature, and crystals annealed for 20 hr then cooled at 30 °C/h are thought to be affected by the cooling process. Consequently, crystals annealed for 20 hr then quenched are considered to be the most suitable to evaluate the effect of temperature thermal defects on these three annealing conditions.

Figure 7-11 shows the relationship between annealing temperature and the ratio of electrical properties of annealed crystals to those of as-grown crystals for crystals annealed for 20 hr then cooled at 30 °C/h (a), and for 20 hr then quenched (b), and for 0.5 hr then quenched (c). In the case of crystals annealing for 20 hr then quenched, the carrier concentration and mobility exhibited the largest decrease at 700 °C. Annealing at 1150 °C decreased the carrier concentration and increased the mobility. The change of electrical properties after other annealing processing have brought almost the same trend as the change of lattice parameter.

#### 7-4. DISCUSSION

The existence of complex Si and As related defects has been pointed out [84,85]. The GaAs crystals used for the samples were grown under As-rich conditions. This condition consists very important meaning in the defect reactions in the process of heat treatment. First, the defect reactions of crystals annealed for 20 hr then quenched were considered, which were suitable for evaluating the temperature dependence of defects.

Lattice parameter, carrier concentration, and mobility decreased when crystals had been annealed at 400 °C. The change in electrical properties indicates an increase in acceptors. It was supposed that a complex of a Si atom sitting on a Ga-site and a Ga vacancy ( $\text{Si}_{\text{Ga}}\text{-V}_{\text{Ga}}$ ) proposed by Chen and Spitzer [66] was formed by this heat



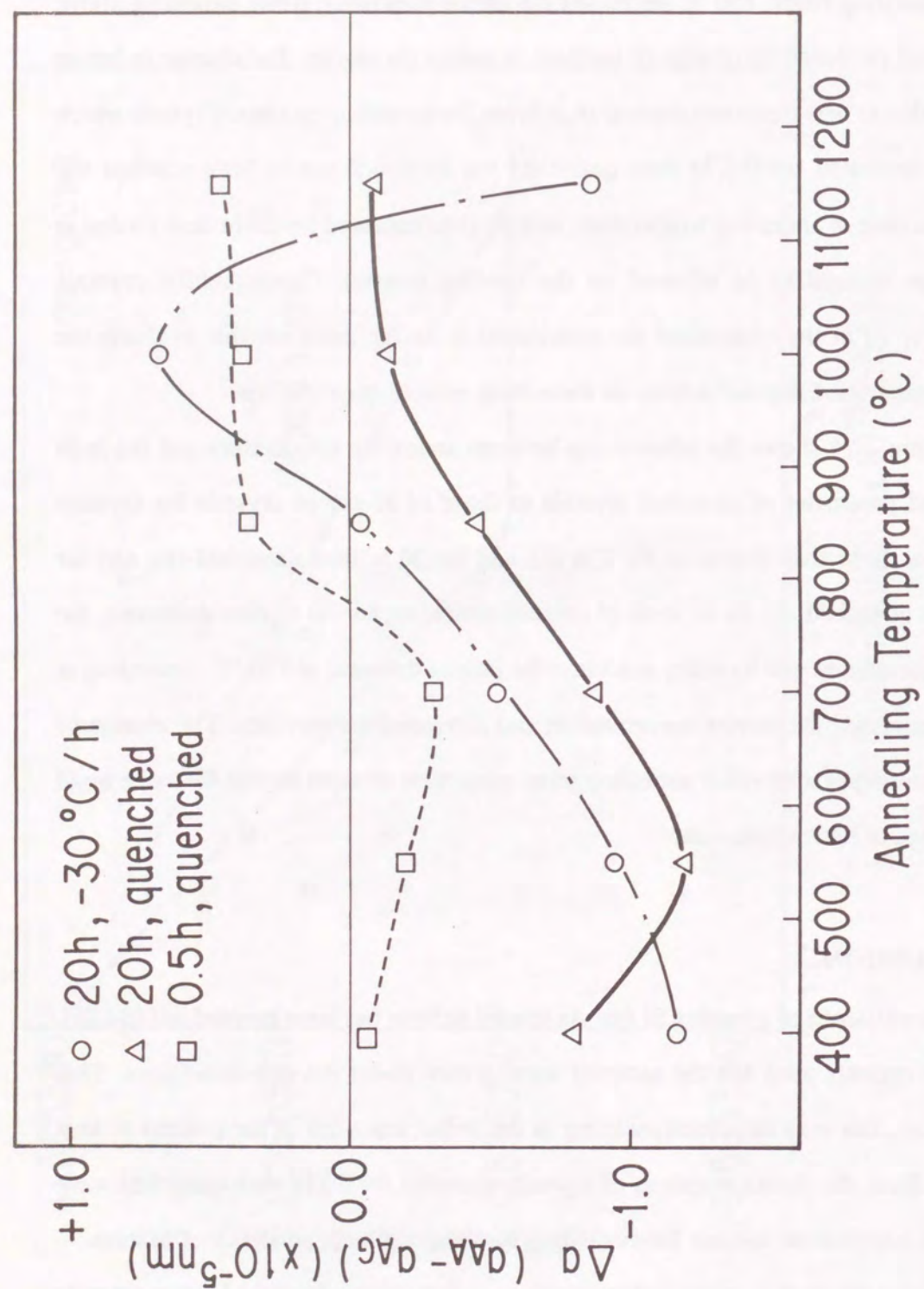


Fig. 7-10 Relationship between change in lattice parameter and annealing temperature.  $\Delta a$  shows the difference in lattice parameter (the lattice parameter of an annealed sample minus that of an as-grown sample).

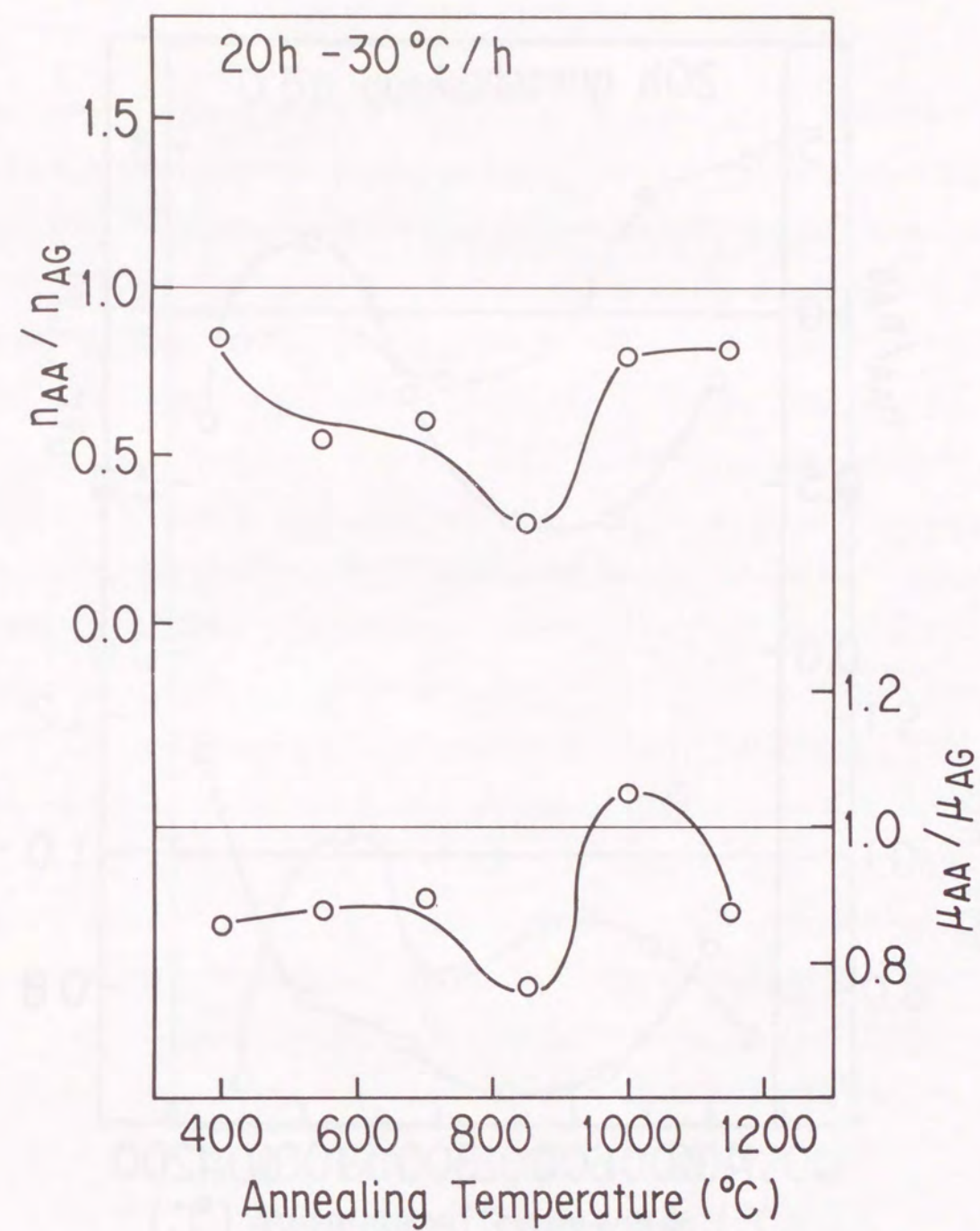


Fig. 7-11 (a)



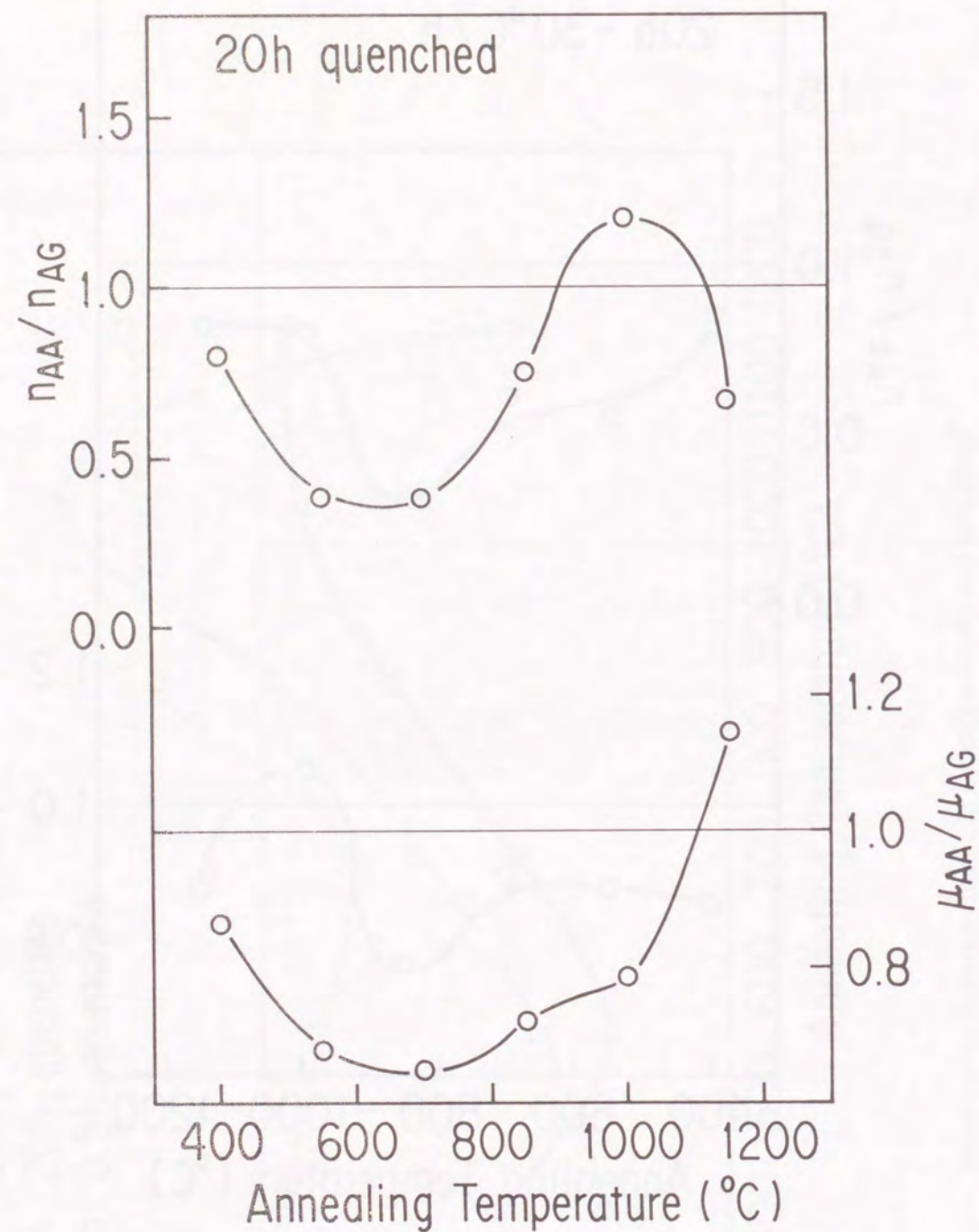


Fig. 7-11 (b)

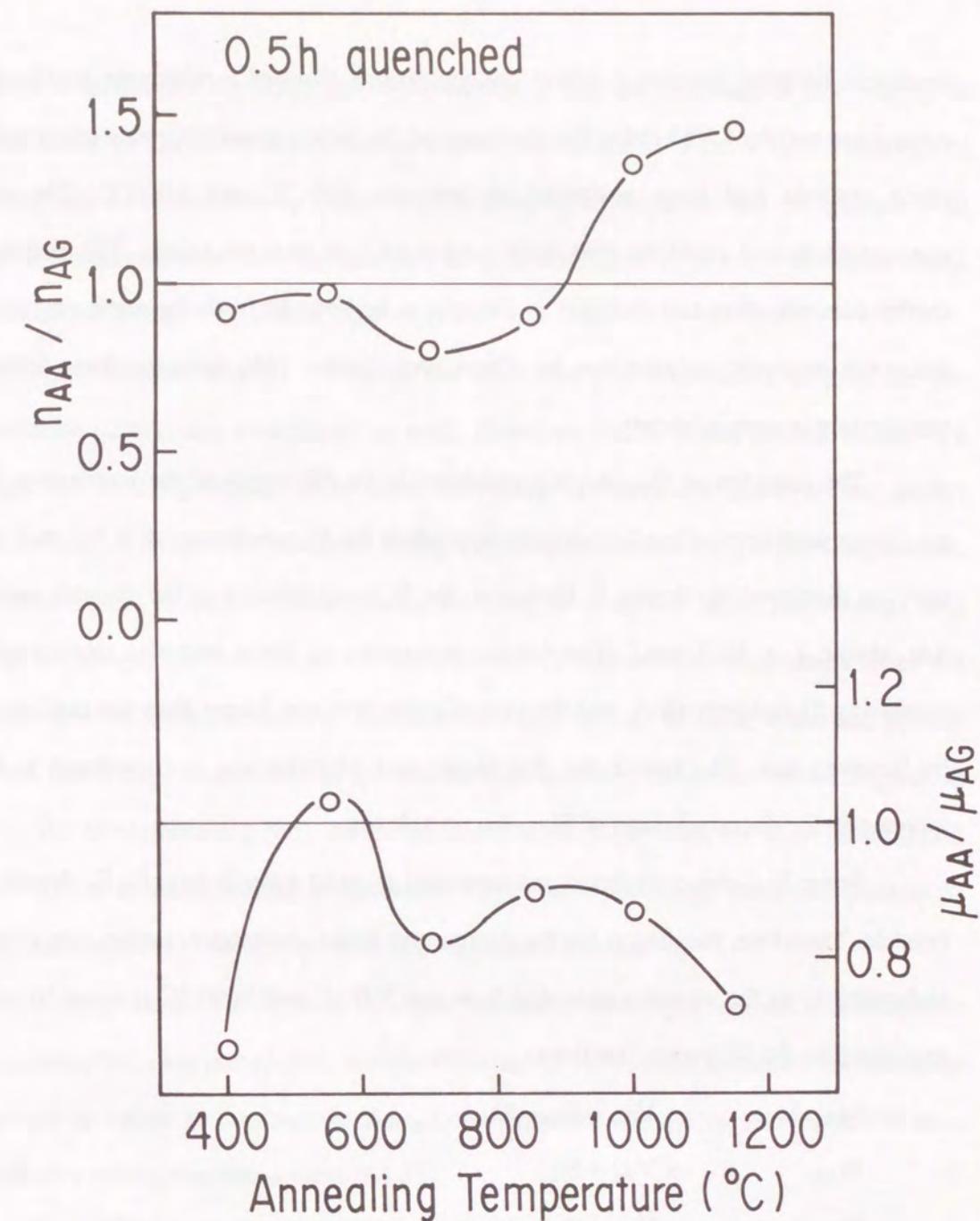


Fig. 7-11 (c)

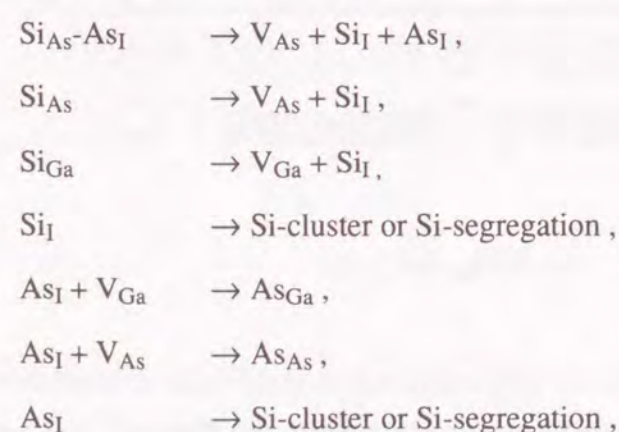
Fig. 7-11 Change in carrier concentration and mobility due to heat treatment in region where Si-related segregation was observed.  $n_{AA}/n_{AG}$  is the ratio of carrier concentration of annealed sample to that of as-grown sample,  $\mu_{AA}/\mu_{AG}$  is the ratio of mobility of annealed sample to that of as-grown sample. Heat treatment condition were annealed for 20 hr then cooled at  $30^{\circ}\text{C/h}$  (a), for 20 hr then quenched (b), and for 0.5 hr then quenched (c).



treatment because Si-related defect concentrations showed a relatively small change when observed by LVM [66]. The decrease of the lattice parameter was observed after these crystals had been annealed at between 500 °C and 1000°C. The carrier concentration and mobility also decreased with this heat treatment. The decrease in carrier concentration and mobility is thought to be derived from the same origin as the unknown acceptor pointed out by Chen and Spitzer [66] because their formation temperature is approximately.

The complex of  $\text{Si}_{\text{As}}\text{-As}_{\text{I}}$  is considered to be the origin of the increase in lattice parameter with increasing Si concentration when the Si concentration is below  $2 \times 10^{18} \text{ cm}^{-3}$ , as discussed in chapter 6. However, the Si concentration of the crystals used here was above  $8 \times 10^{18} \text{ cm}^{-3}$ . The lattice parameter of these samples decreased with increasing Si concentration, and the rate of reduction was larger than the rate predicted by Vegard's law. The reason for this larger rate of reduction is considered to be the increase in the decomposition of  $\text{Si}_{\text{As}}\text{-As}_{\text{I}}$  complexes.

Some  $\text{Si}_{\text{As}}\text{-As}_{\text{I}}$  complexes are supposed to exist even in heavily Si-doped GaAs crystals. Therefore, the reason for the decrease in lattice parameter, carrier concentration, and mobility in the samples annealed between 500 °C and 1000 °C is considered to be explained by the following reactions:



where  $\text{Si}_{\text{I}}$  is a Si interstitial and  $\text{As}_{\text{As}}$  is an As atom at an As-site.

When the Si concentration of GaAs crystals is relatively low, i.e., below  $2 \times 10^{18} \text{ cm}^{-3}$ , annealing of the crystals is considered to simulate the produce dissociation process of  $\text{Si}_{\text{As}}\text{-As}_{\text{I}}$  complexes. After that, each Si atom is considered to occupy a Ga-site and the

As atom is considered to occupy a normal As-site, as discussed in chapter 6. When the Si concentration of GaAs crystals becomes higher, above  $8 \times 10^{18} \text{ cm}^{-3}$ , heat treatment of such crystals is considered to produce a different reaction from that of crystals with lower Si concentration. The reaction due to heat treatment in heavily Si-doped GaAs crystals is described in the following paragraph.

Annealing of heavily Si-doped GaAs crystals is considered to produce the dissociation of  $\text{Si}_{\text{As}}\text{-As}_{\text{I}}$  complexes as well. However the Si atoms at lattice sites are thought to be fully occupied at this annealing temperature because the defect concentration of as-grown crystals is thought to be quenched at the growth temperature. From this reason, it can be deduced that a liberated Si atom in a heavily Si-doped GaAs crystal is thought not to occupy a Ga-site. Even Si atoms at normal lattice sites are considered to be incorporated into the Si-related segregation because Chen and Spitzer reported that a large decrease in  $\text{Si}_{\text{Ga}}$  concentration and  $\text{Si}_{\text{As}}$  concentration takes place in the first 0.5 hr of annealing [66]. As the numbers of  $\text{As}_{\text{Ga}}$  and  $\text{As}_{\text{As}}$  seems to be saturated in equilibrium at the annealing temperature, which have previously been occupied by Si atoms, are supposed to be occupied by decomposed As atoms.

In other words, the decrease in lattice parameter is thought to cause a dissociation of remaining  $\text{Si}_{\text{As}}\text{-As}_{\text{I}}$  complexes, and the decrease in carrier concentration and mobility is thought to cause an increase in  $\text{As}_{\text{Ga}}$  concentration. This  $\text{As}_{\text{Ga}}$  is reported to be a nonradiative recombination centers [84,85].

Use of TEM showed that no Si-related segregation was observed in the crystals were annealed above 1000 °C [83]. Although, the carrier concentration of the crystals decreased and while the mobility of the crystals increased, compared with as-grown crystals. Annealing of the crystals produced no change in lattice parameter. The reason for this change seems to be the formation of small clusters in heavily Si-doped crystals. They could not be observed by TEM, after the decomposition of Si-related segregations in the crystals. However, the clusters can be observed by etching as shown in Fig. 7-7 and by XRT as shown in Fig. 7-8. The Si atoms at lattice sites are considered to become



incorporated into clusters, judging from the change of electrical properties. Defect models of crystals annealed for 20 hr then quenched are summarized in Table 7-1.

The origin of zone-distributed Si-related segregation caused by the annealing between 700 °C and 1000 °C is considered to be related to the increase of the number of anti-site As atoms,  $As_{Ga}$  because of a similar formation temperature [66]. The model of this segregation will be considered below using Fig. 7-6 for reference. Segregation was not observed in the low Si concentration region (region I). When the Si concentration was about  $1 \times 10^{19} \text{ cm}^{-3}$  (region II), segregation process was thought to start from Si-As nuclei joining being attached with Si and excess As atoms (segregation A). Such Si-As nuclei are assumed not to form below 700 °C and to dissociate above 1000 °C. When the Si concentration was between  $1 \times 10^{19} \text{ cm}^{-3}$  and  $1.5 \times 10^{19} \text{ cm}^{-3}$ , the segregation of Si nuclei may have already formed due to the large number of excess Si atoms. In this region, no micro-sized roughness was observed on the etched surface, and the X-rays of XRT were not scattered by clusters (region III). These experimental results suggest that the clusters in this region are very tiny. The character of the defect existing this region is still not clear. When the Si concentration was above  $1.5 \times 10^{19} \text{ cm}^{-3}$ , segregation (segregation B) was considered to be formed from Si nuclei (region IV) dominantly. These Si nuclei must be relatively stable on this logic. These possible models of Si-related segregation and experimental results are summarized in Table 7-2.

## 7-5. CONCLUSION

Defect reactions on heat-treated heavily Si-doped GaAs crystals grown by the GF method were investigated. The lattice parameter of GaAs crystals where the Si concentration was above  $8 \times 10^{18} \text{ cm}^{-3}$  decreased with increasing Si concentration. The rate of reduction is 1.6 times larger than the value predicted by Vegard's law. The reason for this increase in reduction is considered to be the dissociation of  $Si_{As}-As_I$  complexes, which is thought to be the cause of the increase in lattice parameter of crystals with a Si concentration of below  $2 \times 10^{18} \text{ cm}^{-3}$ .

Table 7-1  
Tendency of changes in lattice parameter and electrical properties of annealed samples that were annealed for 20 hr then quenched. The defect model, which seems to explain these changes, is also shown in this table.

Annealing Temperature (°C)	Lattice Parameter	Carrier Concentration / Mobility	Defect Model Silicon      Arsenic
400 - 500	decreased	decreased / decreased	$Si_{Ga} - V_{Ga}$ —
500 - 1000	decreased	decreased / decreased	Si-segregation $As_{Ga}$
1000 - 1150	no change	decreased / increased	micro-clusters      micro-clusters



Table 7-2 Summary of model of zone-distributed segregation formed between 700 °C and 1000 °C.

Region	Nuclei		Comments
	Si + As	Si	
I	×	×	no segregation
II	○	×	segregation (A)
III	△	△	micro - clusters
IV	×	○	segregation (B)

Crystals annealed for 20 hr then quenched are considered to be the most suitable ones for evaluating the temperature dependence of equilibrium defects under three different annealing conditions. Crystals annealed at 400 °C exhibited a decrease in lattice parameter and an increase in acceptors. This change is explained by the formation of  $\text{Si}_{\text{Ga}}\text{-V}_{\text{Ga}}$  pairs. All crystals annealed at between 500 °C and 1000 °C exhibited a decrease in lattice parameter and a large decrease in carrier concentration and mobility. This change in lattice parameter is explained by the dissociation of remaining  $\text{Si}_{\text{As}}\text{-As}_{\text{I}}$  complexes, with the Si atoms incorporating into Si-related segregation. The decrease in carrier concentration and mobility seems to be caused by  $\text{As}_{\text{Ga}}$  formation, which is considered to be a nonradiative recombination center. Crystals annealed above 1000 °C exhibited no change in lattice parameter, a decrease in carrier concentration, and an increase in mobility. The Si-related segregation observed in as-grown crystals could not be found by TEM. Probably, the number density of such defects seems not to be large enough. This change is explained by the formation of clusters after the decomposition of Si-related segregation and the incorporation of Si atoms at lattice sites into clusters.

Zone-distributed segregation formed by annealing between 700 °C and 1000 °C are considered to be those related to anti-site As atoms,  $\text{As}_{\text{Ga}}$ .



## 8. CONCLUSION AND SUMMARY

Both of semi-conducting and semi-insulating bulk GaAs single crystals were grown by the gradient freeze method. The dopant impurities added in the crystals were Si for n-type dopant, Zn for p-type, and Cr for semi-insulating. Si-doped GaAs is a particularly interesting material because they comprise group IV impurities in III-V compound semiconductors.

Distribution of structural defects were found to be closely related to the concave solid-liquid interface. This effect was found by chemical etching. Defects were observed mainly in regions near the concave interface. Defects with complex structures were found around these defects by TEM observation. By taking into account the volume expansion at solidification, the interface shape is the most important item in growing defect free crystals.

Crystals grown by the boat growth method are contaminated by the quartz boats and ampoules. Here, the mechanism of Si contamination is well established, but the effect of oxygen contamination has not been clarified yet. Oxygen contamination in crystals was found to depend on the temperature of the lowest temperature position in the crystal growth reactor. This can be explained by the equilibrium between the oxygen concentration in the melt and the vapor pressure of the oxide of gallium. The characteristics of oxygen contaminated gallium arsenide crystals are the same as those of intentionally oxygen doped crystals.

Under the condition of various arsenic vapor pressures, Si-doped GaAs crystals were grown. The electrical properties of specimens with a common Si concentration changed with changing the arsenic vapor pressure. This change in the electrical properties is considered to reflect the spatial distribution of Si, which is influenced by the melt composition.

The relationship between Si concentration and the lattice parameter was investigated. It was found that the change in lattice parameter of Si-doped crystals was

not consistent with the change predicted by the atomic radii. It is pointed out that the change in lattice parameter is related not only to Si concentration but to the existence of native defects affected by the melt composition. The characteristics and the lattice parameter of crystals were drastically changed after heat treatment, especially in the case of heavily Si-doped crystals.



## ACKNOWLEDGMENTS

I am very obliged to Prof. Dr. M. Hirata and Dr. S. Takeda of Osaka University, Dr. Y. Okada of electrotechnical Laboratory and Dr. F. Orito and Mr. H. Fujita of Mitsubishi Kasei Corporation for their continuous guidance and advice in both scientific and administrative matters through this study.

I would like to express my sincere thanks to Messrs. E. Nishihara, K. Nakamura, M. Yokota, T. Kasuga and Ms. T. Uehara of Mitsubishi Kasei Corporation for their kind help in the present experiments. I am grateful to Dr. Y. Yamaguchi, Dr. K. Okazaki, and Mr. Masanobu Ishida of Mitsubishi Kasei Corporation for their help in simulation study. Many thanks are due to Messrs. Mototoshi Ishida, Y. Kohashi, H. Takahashi, and T. Sato of Mitsubishi Kasei Corporation for fruitful discussions. I am also grateful Dr. S. Muto of Osaka University and Dr. M. Suezawa of Tohoku University for giving me technical information. I also would like to thank Ms. E. Nishimoto for assistance with SIMS.

I also would like to thank Mr. J. Saito, Dr. H. Gotoh, Mr. T. Okano, Dr. F. Yajima and Mr. T. Yuki of Mitsubishi Kasei Corporation for their continuous encouragement.

Finally, I am thankful to many person not listed here, including the members of Semiconductor Production Division and Opto-electronics Laboratory, Mitsubishi Kasei Corporation.

## REFERENCES

- [ 1 ] B. R. Pamplin, "Crystal Growth (Second Edition)", (Pergamon Press, Oxford, 1980)
- [ 2 ] "Semiconductors and semimetals, Vol. 20, Semi-insulating GaAs", edited by R. K. Willardson and Albert C. Beer (Academic Press, Orland, 1984)
- [ 3 ] A. S. Jordan, J. Appl. Phys. 49 (1980) 631
- [ 4 ] S. E. Miller, in "Compound Semiconductor, Vol. 1, Preparation of III-V Compounds", edited by R. K. Willardson and H. L. Goering (Reinford, New York, 1962), p274
- [ 5 ] H. Wenzl, A. Dahlen, A. Fattah, S. Peterson, K. Mika, and D. Henkel, J. Cryst. Growth 109 (1991) 191
- [ 6 ] J. van den Boomgaard and K. Schol, Philips Res. Rep. 12 (1957) 127
- [ 7 ] "Kagoubutsu Handoutai Debaisu", edited by Nihon Sangyo Gijyutsu Shinko Kyokai and Shin-Zairyo Gijyutsu Iinkai (Kogyo Cyosa Kai, Tokyo, 1973) <in Japanese>
- [ 8 ] Dieter K. Schroder, "Semiconductor material and device characterization", (John Wiley and Sons, New York, 1990)
- [ 9 ] T. Ikoma and H. Hasegawa, "Handoutai Zairyo no Kekkan Hyouka Gijyutsu", (Science Forum, Tokyo, 1985) <in Japanese>
- [10] J. Krauskopf, P. Misaelides, G. Wolf, and K. Bethge, J. Trace and Microprobe Techniques 6 (1988) 17
- [11] M. Valladson and J. L. Debrum, J. Radioanal. Chem. 39 (1977) 385
- [12] E. Hanna Bakraji, G. B. Blordiaux, G. Ducouret and J. L. Debrun, Nuclear Instruments and Methods in Physics Research, B56/57 (1991) 896
- [13] G. Thomas and M. J. Goringe, "Transmission Electron Microscopy of Materials", (John Wiley and Sons, New York, 1979)
- [14] J. L. Richards and A. J. Crocker, J. Appl. Phys. 31 (1960) 611



- [15] M. S. Abrahams and C. J. Buiochi, *J. Appl. Phys.* 36 (1965) 2855
- [16] J. G. Grabmaier and C. B. Watson, *Phys. Status Solidi* 32 (1969) k13
- [17] M. Ishii, R. Hirano, H. Kan, and A. Ito, *Jpn. J. Appl. Phys.* 15 (1976) 645
- [18] T. Iizuka, *J. Electrochem. Soc.* 118 (1971) 1190
- [19] G. A. Rozgonyi and T. Iizuka, *J. Electrochem. Soc.* 120 (1973) 673
- [20] J. L. Weyher and P. C. Montgomery, *J. Cryst. Growth*, 106 (1990) 476
- [21] K. Terashima and T. Fukuda, *Proc. of the Symp. on III-V Opto-electronics, Epi. and Dev. Related Processes The ECS 83-13* (1983) 79
- [22] W. L. Bond, *Acta Cryst.* 13 (1960) 814
- [23] Y. Okada, *Bunseki* (1988.3) 168 <in Japanese>
- [24] R. D. Deslattes and A. Hennis, *Phys. Rev. Lett.* 31 (1973) 972
- [25] B. D. Cullity, "Elements of X-ray diffraction", (Addison-Wesley, Massachusetts, 1956)
- [26] L. J. van der Pauw, *Philips Res. Rep.* 13 (1958) 1
- [27] D. V. Lang, *J. Appl. Phys.* 45 (1974) 3023
- [28] J. A. Rossi, C. M. Wolfe, G. E. Stillman, and J. O. Dimmock, *Solid State Commun.* 8 (1970) 2021
- [29] C. E. Huang, D. Elwell and R. S. Feigelson, *J. Crystal Growth* 64 (1983) 441
- [30] C. E. Huang, D. Elwell and R. S. Feigelson, *J. Crystal Growth* 69 (1984) 275
- [31] C. E. Schvezov, I. V. Samarasekera and F. Weinberg, *J. Crystal Growth* 92 (1988) 489
- [32] T. Suzuki, S. Akai, K. Kohe, Y. Nishida, K. Fujita and N. Kito, *Sumitomodenshi* 113 (1983) 111 <in Japanese>
- [33] F. Orito, Y. Tsujikawa and M. Tajima, *J. Appl. Phys.* 55 (1984) 1119
- [34] M. Hirata, S. Takeda and K. Fujii, *Mat. Res. Soc. Symp. Proc.* 104 (1988) 495
- [35] M. Hirata, S. Takeda and K. Fujii, *Proc. of 5-th Conf. on Semi-insulating III-V Materials, Malmö, Sweden, 1988*, Eds. by G. Grossmann and L. Ledebø (Hilger, Bristol, 1988), p549
- [36] W. J. P. van Enkevort, R. Janssen-van Rosmalen, H. Klapper and

- W. H. van der Linden, *J. Crystal Growth* 60 (1982) 67
- [37] L. J. Segerlind, *Applied Finite Element Analysis* (John Wiley & Sons., New York, 1976)
- [38] C. N. Cochran and L. M. Foster, *J. Electrochem. Soc.* 109 (1962) 149
- [39] J. R. Knight, *Nature* 185 (1961) 1001
- [40] R. I. Stearns and J. B. McNeely, *J. Appl. Phys.* 37 (1966) 933
- [41] T. Kobayashi, J. Lagowski and H. C. Gatos, *5th Conf. on Semi-insulating III-V Materials, Malmö, Sweden, 1988*, Eds. by G. Grossmann and L. Ledebø (Hilger, Bristol, 1988), p435
- [42] T. Suzuki and T. Akai, *Bussei* (1971.3) 144 <in Japanese>
- [43] S. Akai, K. Fujita, M. Sasaki and K. Tada, *Int. Symp. GaAs and Related Compounds, Japan, 1981*, *Inst. Phys. Conf. Ser.* 63, p13
- [44] J. Leitner and F. Moravec, *J. Crystal Growth* 83 (1987) 376
- [45] J. F. Woods and N. G. Ainslie, *J. Appl. Phys.* 34 (1963) 1469
- [46] G. M. Martin, G. Jacob, J. P. Hallais, F. Grainger, J. A. Roberts, B. Clegg, P. Blood and G. Poiblaud, *J. Phys. C (Solid State Phys.)* 15 (1982) 1841
- [47] H. C. Gatos, M. Skowronski, L. Pawlowicz and J. Lagowski, *Int. Symp. GaAs and Related Compounds, Biarritz, 1984*, *Inst. Phys. Conf. Ser.* 74, p41
- [48] P. Mo, J. Yang, S. Li, D. Jiang and H. Zhao, *J. Crystal Growth* 65 (1983) 243
- [49] W. Walukiewicz, J. Lagowski and H. C. Gatos, *J. Appl. Phys.* 53 (1982) 769
- [50] C. N. Cochran and L. M. Foster, *J. Electrochem. Soc.* 109 (1962) 144
- [51] N. N. Greenwood, *Adv. Inorg. Chem. Radiochem.* 5 (1963) 91
- [52] J. Lagowski, D. G. Lin, T. Aoyama and H. C. Gatos, *Appl. Phys. Lett.* 44 (1984) 336
- [53] Zhao-Qiang Fang, T. E. Schlesinger and A. G. Milnes, *J. Appl. Phys.* 61 (1987) 5047
- [54] S. Mizutani, M. Mori, T. Ono, T. Miyazawa and I. Ohdomari, *Jpn. J. Appl. Phys.* 19 (1980) 1107
- [55] G. Sun and A. Liu, *Int. Symp. GaAs and Related Compounds, Biarritz,*



- 1984, Inst. Phys. Conf. Ser. 74, p107
- [56] M. Kaminska, J. Lagowski, J. Parsey, K. Wada and H. C. Gatos, Int. Symp. GaAs and Related Compounds, Japan, 1981, Inst. Phys. Ser. 63, p197
  - [57] P. D. Greene, J. Crystal Growth 50 (1980) 612
  - [58] J. K. Kung and W. G. Spitzer, J. Appl. Phys. 45 (1974) 2254
  - [59] M. R. Brozel, K. Laithwaite, R. C. Newman and B. Ozbay, J. Crystal Growth 50 (1980) 619
  - [60] J. B. Mullin, A. Royle and S. Benn, J. Crystal Growth 50 (1980) 625
  - [61] D. T. J. Hurle, J. Crystal Growth 50 (1980) 638
  - [62] D. T. J. Hurle, Proc. of 5-th Conf. on Semi-Insulating III-V Materials, Malmö, Sweden, 1988, Eds. by G. Grossmann and L. Ledebø, (Hilger, Bristol, 1988), p11
  - [63] R. Fornari, J. Crystal Growth 94 (1989) 433
  - [64] T. P. Chen, Y. D. Guo, T. S. Huang and L. J. Chen, J. Crystal Growth 103 (1990) 243
  - [65] R. T. Chen, V. Rana, and W. G. Spitzer, J. Appl. Phys. 51 (1980) 1532
  - [66] R. T. Chen and W. G. Spitzer, J. Electronic Materials 10 (1981) 1085
  - [67] H. Wenzl, K. Mika and D. Henkel, J. Crystal Growth 100 (1990) 377
  - [68] C. M. H. Driscoll, A. F. W. Willoughby, J. B. Mullin and B. W. Straughan, Int. Phys. Conf. Ser. No. 24 (1975), p.275
  - [69] J. F. C. Baker, M. Hart, M. A. G. Halliwell and R. Heckingbottom, Solid State Electron. 19 (1976) 331
  - [70] P. F. Fewster and A. F. W. Willoughby, J. Cryst. Growth 50 (1980) 648
  - [71] G. P. Watson, D. Ast and A. G. Elliot, Appl. Phys. Lett. 54 (1989) 271
  - [72] F. Orito, K. Fujii and Y. Okada, J. Appl. Phys. 68 (1990) 5696
  - [73] C. D. Thurmond, J. Phys. Chem. Solids 26 (1965) 785
  - [74] T. Iizuka, Jpn. J. Appl. Phys. 7 (1968) 490
  - [75] M. Suezawa, A. Kasuya, Y. Nishina and K. Sumino, J. Appl. Phys. 69 (1991) 1618

- [76] M. Suezawa, K. Kasuya, Y. Nishina and K. Sumino, Materials Science Forum 83-87 (1992) 953
- [77] Y. Okada, Y. Tokumaru and Y. Kadota, Appl. Phys. Lett. 48 (1986) 975
- [78] K. Usuda, S. Yasuami, T. Fujii, Y. Higashi, H. Kawata and M. Ando, J. Appl. Phys. 69 (1991) 182
- [79] Y. Okada and F. Orito, Appl. Phys. Lett. 52 (1988) 582
- [80] L. Pauling, "The Nature of the Chemical Bond (Third Edition)", (Cornell Univ. Press, Ithaca, New York, 1960)
- [81] R. Heckingbottom, M. A. G. Hallwell, J. F. C. Baker and M. Hart, Solid State Electronics 19 (1976) 335
- [82] U. Pietsch and K. Unger, Phys. Stat. Sol. (a) 80 (1983) 165
- [83] S. Muto, S. Takeda, M. Hirata, K. Fujii and K. Ibe, Phil. Mag. A 66 (1992) 257
- [84] C. Frigeri and J. L. Weyher, J. Appl. Phys. 65 (1989) 4646
- [85] E. P. Visser, P. J. van der Wel, J. L. Weyher and L. J. Giling, J. Appl. Phys. 68 (1990) 4242



## Published Papers

### <Chapter 3>

K. Fujii, M. Hirata, H. Fujita and S. Takeda, Defect Control in Semiconductors, Yokohama, Japan, 1989, Ed. by K. Sumino (Elsevier, Amsterdam, 1990), p667-672, "Solid-Liquid Interface Shape and Characteristic Structural Defects in Gallium Arsenide Single Crystals Grown by the Gradient Freeze Method"

### <Chapter 4>

K. Fujii, F. Orito, H. Fujita and T. Sato, J. Crystal Growth 121 (1992) 255-266, "The Role of Diffusion Barrier Temperature in Gallium Arsenide Single Crystals Grown by the Gradient Freeze Method"

### <Chapter 5>

K. Fujii, F. Orito and H. Fujita, Mat. Sci. Forum 117-118 (1993) 393-398, "The Effect of Arsenic Vapor Pressure on Site Distribution of Silicon in Gallium Arsenide Grown by the Gradient Freeze Method"

### <Chapter 6>

K. Fujii, Y. Okada and F. Orito, J. Appl. Phys. 73 (1993) 88-94, "The effect of Silicon Doping on Lattice Parameter and Silicon Related Defects in Gallium Arsenide Grown by the Gradient Freeze Method"

### <Chapter 7>

Y. Okada, K. Fujii, F. Orito and S. Muto, J. Appl. Phys. 73 (1993) 1675-1680, "Defect Reactions by Heat Treatment of Heavily Silicon Doped Gallium Arsenide"

S. Muto, S. Takeda, M. Hirata, K. Fujii and K. Ibe, Philos. Mag. A 66 (1992) 257-268, "Structure of Planer Aggregates of Si in Heavily Si-doped GaAs"



